UNIVERSIDADE FEDERAL DO RIO GRANDE DO SUL
PROGRAMA DE PÓS-GRADUAÇÃO EM MICROELETRÔNICA

LUCAS PRATES MARTINS

Flexible Temperature-Pressure Organic Sensor

Dissertação apresentada como requisito parcial para a obtenção do grau de Mestre em Microeletrônica.

Orientador: Prof. Dr. Henri Ivanov Boudinov

Porto Alegre
2020

AGRADECIMENTOS

A **Deus**, donde provém toda a ciência e conhecimento, pois somente com Ele, por Ele e Nele é que, de fato, tudo é possível, e à **Mãe Rainha e Vencedora Três Vezes Admirável de Schoenstatt**, pois são dela todos os méritos, e entrego todo o esforço e dedicação empenhados neste trabalho ao seu **Capital de Graças**, para maior Glória de Deus e da Santa Igreja.

À **Universidade Federal do Rio Grande do Sul**, por sua estrutura, corpo docente e administração e pela oportunidade de realizar este trabalho de pesquisa por meio do **Programa de Pós-Graduação em Microeletrônica**.

Ao meu orientador, professor **Dr. Henri Ivanov Boudinov**, por seu singular *espírito de paternidade*, com todo seu conhecimento, dedicação, atenção e, principalmente, paciência, sem os quais este trabalho não seria possível. ***Много благодаря!***

Aos meus colegas do **Laboratório de Microeletrônica**, **Ricardo Augusto Razera Leandro Lunardelli Soares**, sempre dispostos a ajudar quando necessário.

À minha noiva, **Mariana Peixoto Feyh**, de forma especial, por suas orações, carinho, paciência, motivação, amor e suporte constantes, sem os quais este trabalho não teria propósito.

Aos meus pais, **Francisco José de Ávila Martins** e **Carla Silvana Prates Martins**, pois sem o esforço, amor e dedicação deles, nada disso seria possível. Aos meus **avós**, **tios**, **primos** e **demais familiares**, pelas constantes orações, apoio e dedicação ao longo de toda a minha vida.

Aos padres **Roque Machado** e **Pedro Willemsens** e à **Irmã Maria Aparecida** por serem a presença viva de Cristo e de Maria Santíssima em minha vida e por sua amizade e orientação espiritual. Aos meus amigos e irmãos de caminhada do **Grupo Transfiguração**, **Movimento Apostólico de Schoenstatt** e da **Paróquia Menino Deus de Porto Alegre,** pelas orações, suporte e amizade.

E a todos que direta ou indiretamente fizeram parte desta importante etapa da minha vida, o meu muito obrigado!

This work was partially supported by **Conselho Nacional de Desenvolvimento Científico e Tecnológico** (CNPq, Proc. 405.603/2018-5), **Coordenação de Aperfeiçoamento de Pessoal de Nível Superior** (CAPES – Finance Code 001) and **Fundação de Amparo à Pesquisa do Estado do Rio Grande do Sul** (FAPERGS).

RESUMO

Este trabalho teve como objetivo desenvolver um sensor de pressão e temperatura baseado em fenômenos piezo-resistivo e termoelétrico, usando espuma de poliuretana porosa e melamina impregnadas em solução de *Poly(3,4-ethylenedioxythiophene)-poly(styrenesulfonate)* (PEDOT:PSS). Este dispositivo permite a medida simultânea de temperatura e pressão através da transdução de estímulos externos em sinais elétricos separados, com resolução promissora de detecção de temperatura e pressão para inteligência artificial e sistemas de aplicação em saúde. Foi possível fabricar sensores individuais, que atingiram um desempenho máximo de 90% da variação da resistência, com capacidade de detectar, de 3 a 30 kPa, entre uma faixa de 10 e 50% de deformação, respectivamente. Esses dispositivos geraram uma tensão térmica média de 2,8 mV sob estímulo de alta temperatura. Levando em consideração os parâmetros de fabricação e a performance obtida para sensores individuais, foi fabricada uma matriz 4x4, utilizando uma abordagem nova, ainda não relatada na literatura. Utilizou-se uma peça única de melamina impregnada em PEDOT:PSS diluído para a construção do dispositivo. O sensor foi integrado ao microcontrolador Arduino e uma interface foi implementada com software de interface visual para monitoramento em tempo real de posição e intensidade de pressão. O dispositivo sensor matricial 4x4 apresentou resultados promissores, havendo a necessidade, contudo, de se aprimorar os contatos entre os eletrodos e a esponja, visto que estes apresentavam degradação com o uso intensivo.

ABSTRACT

This work aimed to develop pressure and temperature sensor based on piezo-resistive and thermoelectric phenomena, using porous polyurethane and melamine foams impregnated with a solution of *Poly (3,4-ethylenedioxythiophene)-poly(styrenesulfonate)* (PEDOT:PSS). This device allows the simultaneous measurement of temperature and pressure through the transduction of external stimuli into separate electrical signals, with a promising resolution of temperature and pressure detection for artificial intelligence and health application systems. It was possible to manufacture individual sensors, which achieved a maximum performance of 90% of the resistance variation, with the ability to detect, from 3 to 30 kPa, between a range of 10 and 50% of deformation, respectively. These devices generated an average thermal voltage of 2.8 mV under elevated temperature stimulus. Considering the manufacturing parameters and the performance obtained for individual sensors, a 4x4 matrix was manufactured, using an innovative approach, not yet reported in the literature. A single piece of melamine impregnated with diluted PEDOT: PSS was used to construct the device. The sensor was integrated with the Arduino microcontroller and an interface was implemented with visual interface software for real-time monitoring of pressure position and intensity. The 4x4 matrix sensor device showed promising results, with the need, however, to improve the contacts between the electrodes and the sponge, since they presented degradation with intensive use.

LIST OF FIGURES

LIST OF TABLES

LIST OF ABBREVIATIONS AND SYMBOLS

σ	mechanical stress
ε	mechanical strain
F	force load
E	Young's modulus
TE	Thermoelectric Effect
J	current density
σ_c	electrical conductivity
E_{emf}	electromotive field
S_T	Seebeck Coefficient
∇T	temperature gradient
V_{therm}	thermoelectric voltage
ρ	electrical resistivity
R_s	electrical sheet resistance
PEDOT:PSS	Poly(3,4-ethylenedioxythiophene)-poly(styrenesulfonate)
PU	porous polyurethane
D23, D33, D43	foam density 23, foam density 33, foam density 43
MS	melamine sponge

TABLE OF CONTENTS

1. INTRODUCTION

The development of increasingly sophisticated and complex devices comes from the emerging need of sectors of industry and science to operate in a wide range of applications and problems. The introduction of microelectronics and micro-systems in the biomedical and health sciences can contribute to significant advances in the development of biomedical tools while, at the same time, reducing related costs.

Flexible, low-cost temperature and pressure sensing devices are essential to meet many advanced artificial intelligence application requirements (GUIRIEC *et al.*, 2009; SEKITANI *et al.*, 2008, 2010). Due to their flexibility and accessibility, organic electronic devices are promising candidates for integrated intelligent systems. Researchers have recently taken the first steps towards developing electronic skin from organic materials and pressure sensor matrices for health applications (SCHWARTZ *et al.*, 2013; TEE *et al.*, 2012).

Even more fascinating, organic devices offer simultaneous detection of pressure and temperature stimuli, mimicking human skin functionality. The transduction of multiple stimuli into a signal coupled or separated by the sensing elements becomes necessary for this achievement. To date, only limited examples of temperature-pressure sensing devices based on organic material exist in the literature because of the critical requirements for the multifunctionality of materials, such as the ability to perform distinct detections simultaneously (SOMEYA *et al.*, 2005; WANG *et al.*, 2017; ZHANG *et al.*, 2015). The integration of individual pressure and temperature sensors into one pixel stands for an efficient approach to achieve two-parameter sensing functionality.

Receiving help from the ingenious integration of organic devices, Someya et al. showed flexible, large-area, conformal pressure and temperature sensor networks with active organic field-effect transistors (OFET) arrays (SOMEYA *et al.*, 2005).

In 2009, GUIRIEC *et al.* reported constructing an organic nonvolatile memory transistor for flexible sensor arrays (Figure 1.1).

The making of nonvolatile memory arrays on flexible plastic substrates took place using organic transistors with a floating gate embedded in hybrid dielectrics that formed a two nanometer-thick molecular self-assembled monolayer. The dielectrics' small thickness allowed impressively small program and erased voltages (≤6 volts) to produce a nonvolatile, reversible threshold-voltage shift. The transistors endured more than 1000 programs and erased cycles (GUIRIEC *et al.*, 2009).

Figure 1.1(a) shows a photograph of an organic floating-gate transistor sheet forming 26 by 26 memory cells (the array has a significant area of 50 by 50 mm^2). Figure 1.1(b) shows the schematic of the floating-gate transistors' cross-section. The substrate is flexible PEN. The control and floating gates are 20-nm-thick layers of evaporated aluminum. The top and bottom plastic dielectrics are a combination of a 4-nm-thick layer of AlOx and a 2-nm-thick SAM. The organic semiconductor is a 50-nm-thick layer of pentacene, and the source and drain contacts are 50-nm-thick layers of evaporated gold.

Figure 1.1: (a) Photograph of an organic floating-gate transistor sheet. The inset shows a magnified image of the array. (b) Schematic cross-section of the floating-gate transistors.

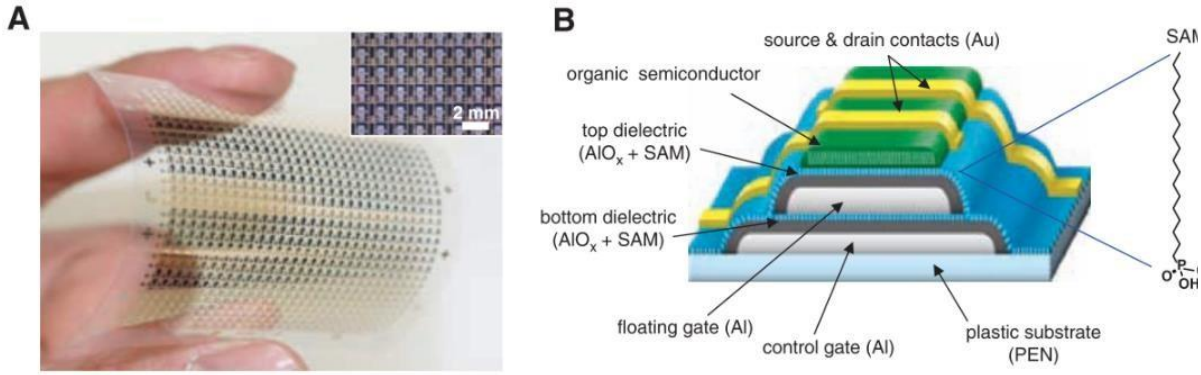

From (GUIRIEC *et al.*, 2009)

In 2013, LAI *et al.* presented a thin-film device fabricated on a flexible substrate and conceived explicitly for tactile sensing (Figure 1.2).

The device's fabrication takes place on a polydimethylsiloxane capacitor integrated with a floating-gate organic field-effect transistor able to operate at ultralow voltages. Its construction principle consisted of the physical separation between the pressure-sensitive area and the active area of the OFET. The constructed device, named pressure-modulated FET (PMOFET), incorporated a floating gate OFET connected with a thin-film, *polydimethylsiloxane* (PDMS) capacitive sensor working as a floating-gate transistor, biased through a control capacitor.

The PMOFET derivates from the charge-modulated FET (CMFET), in which the transduction mechanism occurs on the transistor's field effect's modulation due to the variation of charge distribution in the floating-gate (LAI *et al.*, 2013).

Figure 1.2: Structure of the PMOFET and summary of the employed materials.

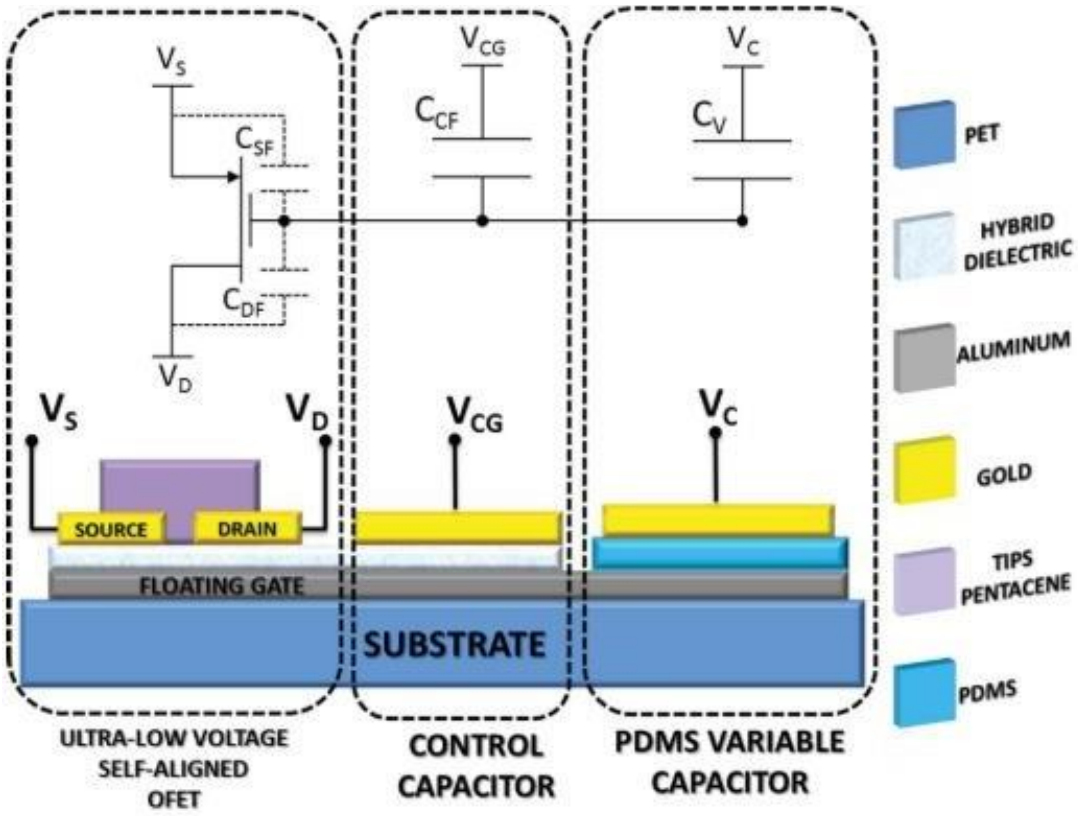

From (LAI *et al.*, 2013)

In 2018, WANG *et al.* described a fabrication process (Figure 1.4) that enables high yield and uniformity from various intrinsically stretchable electronic polymers (Figure 1.3).

This process offers a promising general platform for incorporating other intrinsically stretchable polymer materials and enabling the fabrication of next-generation stretchable skin electronic devices. The fabrication process allowed the demonstration of an intrinsically stretchable polymer transistor array with an unprecedented device density of 347 transistors/cm^2.

The transistors had average charge-carrier mobility comparable to amorphous silicon, varying within one order of magnitude when subjected to 100 percent strain for 1,000 cycles, without current-voltage hysteresis. Thus, the transistor arrays constitute intrinsically stretchable skin electronics and include an active matrix for sensory arrays and analog and digital circuit elements (WANG *et al.*, 2018).

Figure 1.3: Intrinsically stretchable transistor array as a core platform for functional skin electronics. Three-dimensional diagram of an intrinsically stretchable transistor array as the core building block of skin electronics.

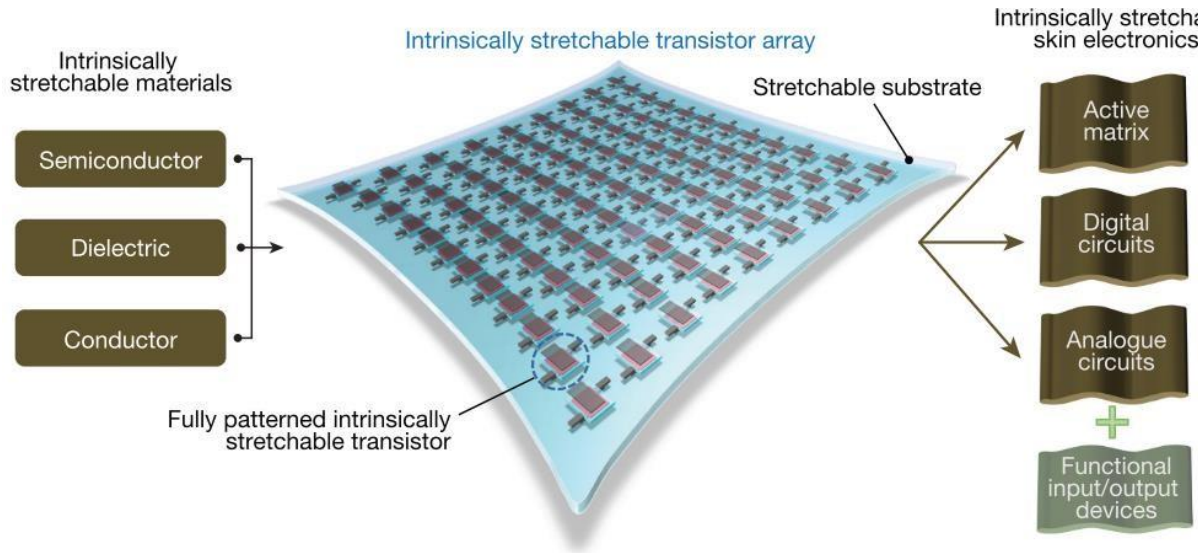

From (WANG *et al.*, 2018)

WANG et al. described a general fabrication process flow (Figure 1.4), which enables high device yield, device-to-device uniformity, good material compatibility between layers, and good electrical and mechanical performances. Specifically, the process flow uses layer-by-layer direct deposition of active components to avoid the low yield and poor uniformity typically obtained from transfer processes.

The process begins with a silicon wafer coated with a water-soluble sacrificial layer (dextran) to enable the devices' final release onto a stretchable substrate, ensuring good substrate compatibility during the entire fabrication process. The deposition and photopatterning of a stretchable dielectric occur in the sequence.

It was necessary to perform the consecutive deposition and patterning of the stretchable semiconductor to get a top-contact structure and conductor for source/drain electrodes. Then, there is the laminating of a stretchable substrate onto the device. It was necessary to soak the device in water to release it from the rigid substrate. The gate electrodes are deposited and patterned on the dielectric layer to complete the transistor structure (WANG *et al.*, 2018).

Figure 1.4: Fabrication process flow.

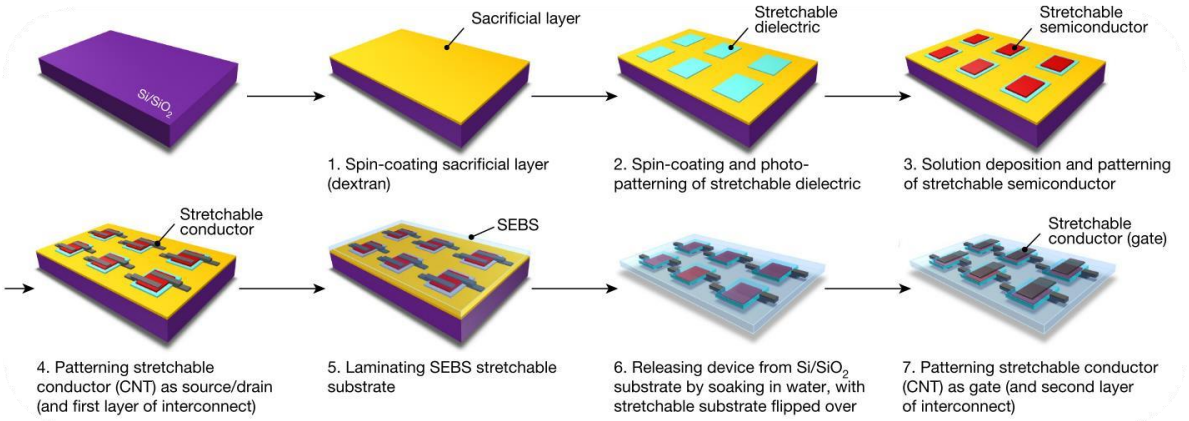

From (WANG *et al.*, 2018)

In 2009, GRAZ *et al.* showed the development of a dual-parameter sensor based on flexible active-matrix cells for application on pressure and temperature sensing skin, built with bifunctional polymer-ceramic nanocomposite (Figure 1.5).

The construction of the device occurs with a bifunctional sensory cell. The composition of this sensory cell includes two sub-cells, one being pressure-sensitive (a piezoelectric element with antiparallel polarization) and the other temperature-sensitive (a pyroelectric element with parallel polarization), which was formed by piezoelectric ceramic lead titanate nanoparticles along with a polymer matrix of ferroelectric *poly(vinylidene fluoride trifluoro-ethylene)* to ensure mechanical flexibility. The bifunctional sensor array (front-plane foil) aligned with thin-film transistors (TFTs) formed a flexible backplane (GRAZ *et al.*, 2009).

Figure 1.5(a) shows the bifunctional sensor array scheme for the lamination of the flexible ceramic polymer sensor front-plane on a flexible transistor backplane. The pyroelectric sub-elements have a parallel orientation of the polarization in the ceramic nanoparticles and ferroelectric polymer matrix, while the piezoelectric sub-elements have an antiparallel orientation of the polarization. Figure 1.5(b) shows the photograph of a two-element sensor prototype.

Figure 1.5: (a) Scheme of the bifunctional sensor array; (b) Photograph from a two-element sensor prototype.

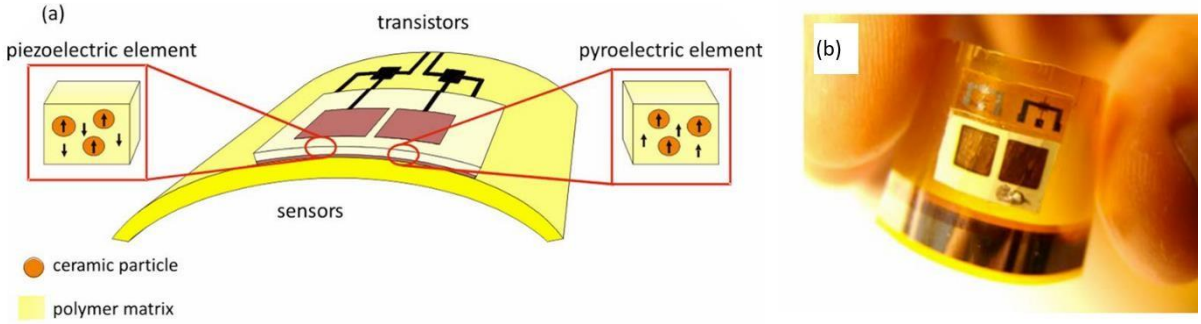

From (GRAZ *et al.*, 2009)

Figure 1.6 illustrates the execution of a two-step poling sequence process, which occurs in a way that the composite's inherent sensitivity to pressure and temperature allows for its selective and spatial control. The temperature and voltage profiles are on the same time scale. The arrows indicate the polling process's end, where the acquisition of the pyro and

piezoelectric elements occurs. P_p and P_c denote the polymer and ceramic polarization, while ***p*** and ***c*** represent the pyro and piezoelectric coefficients.

Figure 1.6: Two-step poling process for obtaining multifunctional nanocomposites.

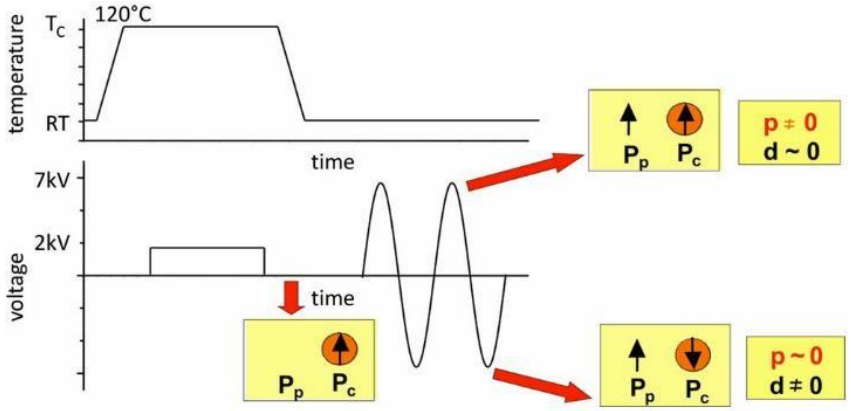

From (GRAZ *et al.*, 2009)

The resulting sub-cells are sensitive to either pressure or temperature, with minor cross-sensitivity to the other input parameter (Figure 1.7).

Figure 1.7: Amplitude of the drain-source current changes of the hybrid sensor front and backplane showing reduced cross-sensitivities of the piezo (a) and pyroelectrical (b) sub-cells interfaced with a-Si:H TFTs.

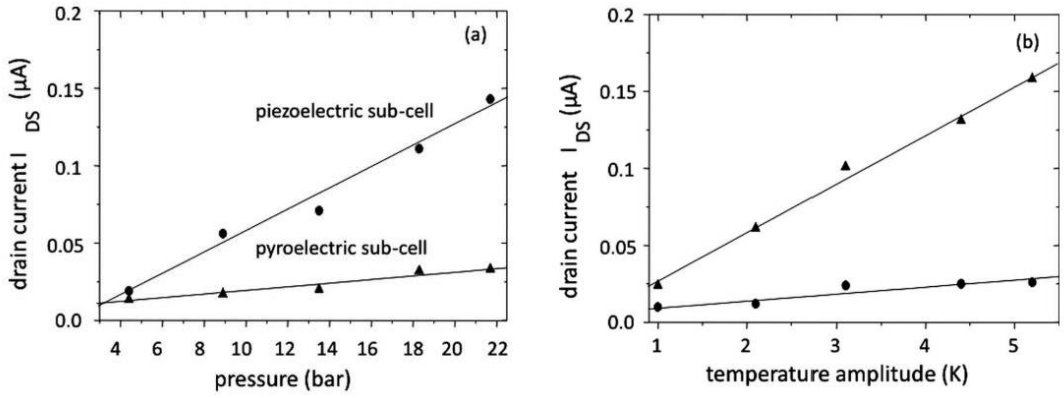

From (GRAZ *et al.*, 2009)

The development of new double parameter sensors that transduce different stimuli into separate signals can intrinsically minimize the pressure stimulus's influence on the temperature signal and vice versa, significantly facilitating analysis and allowing for more precision in both pressure and temperature measurements. For most organic active devices with external power supplies, the current is usually a unique signal, which prevents its use in two-parameter sensing applications. In 2015, ZHANG *et al.* showed a promising approach to develop a pressure-temperature double-parameter sensor using a *microstructure frame-supported organic thermoelectric* materials (MFSOTE) (ZHANG *et al.*, 2015).

Taking advantage of independent piezoresistive and thermoelectric effects in a single device, the execution of simultaneous monitoring of temperature and pressure occur by transducing external stimuli into separate electrical signals (Figure 1.8). The devices can be self-powered by a temperature gradient with promising temperature and pressure detection resolution for artificial intelligence and healthcare applications.

Figure 1.8: Illustrative schematic of a flexible dual-parameter device with thermoelectric and piezoresistive properties. (a–h) Schematic illustration of temperature–pressure (T–P) sensing mechanism: (a, b) The device in its pristine condition; (c, d) The stimulus of a temperature difference ($\Delta T = TS - T_0$) applied across the device; (e, f) Stimulus of a pressure load over the device; (g, h) loading of a coupled temperature and pressure stimuli.

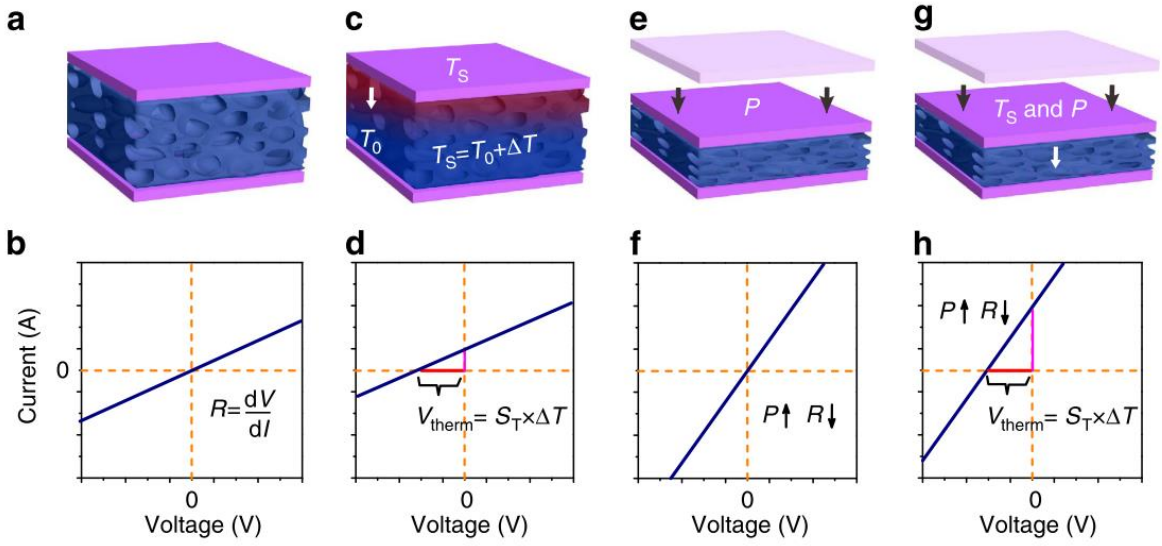

From (ZHANG *et al.*, 2015)

It is possible to deposit an organic thermoelectric material into a deformable structure to achieve such temperature and pressure sensing properties for a flexible dual-parameter device. In that way, when the device is under the stimulus of an object with coupled temperature and pressure, the temperature difference ΔT between the surface (T_S) and the bottom (T_0) of the device becomes detectable via thermoelectric effect (Figure 1.8(c, d)), leading to instantaneous detection of the surface temperature when the device has a constant bottom temperature, like for the skin. Meanwhile, the microstructure is deformed due to an existing force *P*, which changes the active layer's resistance as a function of the applied pressure (Figure 1.8(e, f)). Therefore, it becomes possible to detect the temperature and pressure separately and simultaneously (Figure 1.8(g, h)).

Similarly, another promising approach demonstrated in the literature consists of constructing a conductive foam by one-step dip coating of a commercial melamine sponge (MS, composed by a *copolymer of formaldehyde sodium bisulfite melamine*), in an aqueous dispersion of *Poly(3,4-ethylenedioxythiophene)-poly(styrenesulfonate)* (PEDOT:PSS) (DING *et al.*, 2018). Such conductive PEDOT:PSS@MS may present high compressibility and a stable piezoresistive response at the compressive strain up to 80% and good reproducibility over 1000 cycles, due to the interconnected porous structure of MS (Figure 1.9).

Figure 1.9: (a) Electric resistance variations of a PEDOT:PSS@MS device under different compressive strains. Inset: Image of a pressure sensor device. (b) Relative resistance variation [$(R–R_0)/R_0$] of a PEDOT:PSS@MS under different compressive strains; (c) Time-dependent response of $(R–R_0)/R_0$ during the compress−release cycle between 0 and 70% strain.

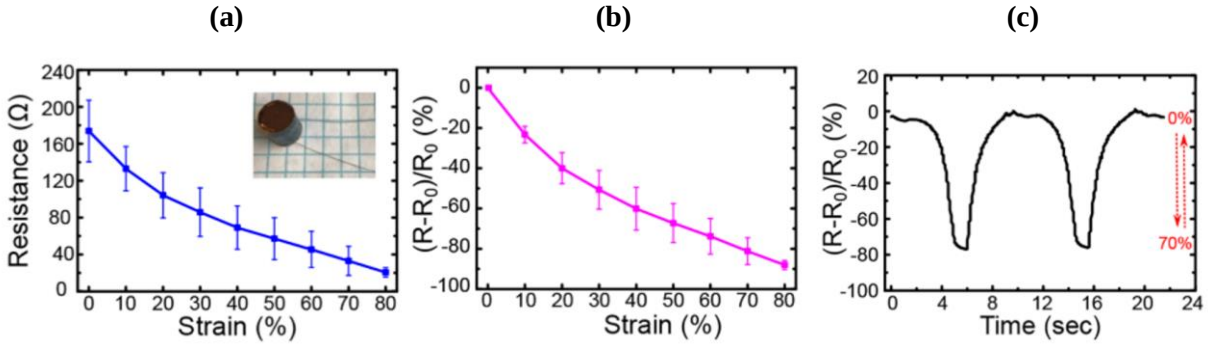

From (DING *et al.*, 2018)

The versatile pressure sensors fabricated using the conductive PEDOT:PSS@MS sponges can be attached to various parts of the human body, detecting various human movements, including speech, finger bending, elbow bending, and walking. A tactile sensor array based on these pressure sensors can also be built (Figure 1.10).

Figure 1.10: (a) Photograph of a PEDOT:PSS@MS-based sensory array containing 3 pixel × 3 pixel pressure sensor units; (b) Mapping of the relative resistance changes corresponding to the pressure applied by a balance weight placed on the sensory array. Inset: a photograph of the sensory array with the balance weight placed on top. (c) Mapping of the relative resistance changes corresponding to the pressure applied by a AAA battery placed on the sensory array. Inset: photograph of the sensory array with the AAA battery placed on top.

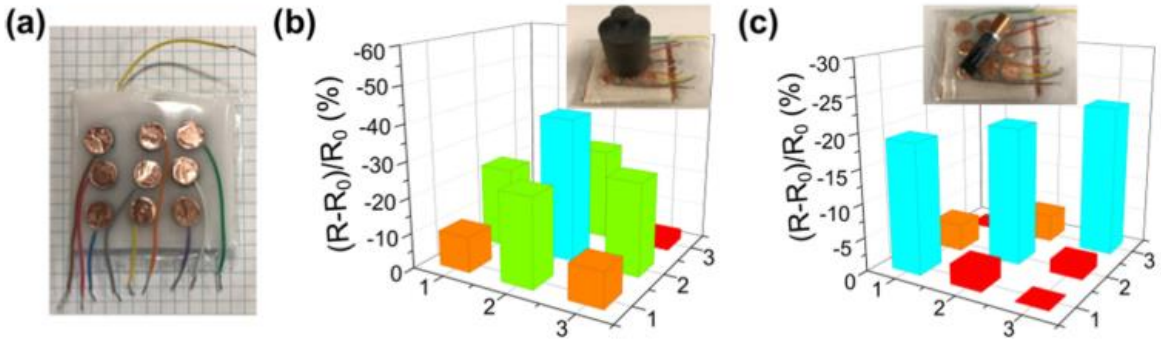

From (DING *et al.*, 2018)

In summary, by using a conducting thermoelectric material such as PEDOT:PSS and a microstructured frame material made of porous polyurethane (PU) or melamine sponge (MS), it is possible to manufacture PEDOT:PSS@PU and PEDOT:PSS@MS devices via one-step dip coating of sponges in an aqueous solution of PEDOT:PSS (DING *et al.*, 2018; ZHANG *et al.*, 2015)**.** Considering that, this work aimed to develop a double parameter pressure-temperature two-dimensional sensor matrix using organic thermoelectric materials impregnated in sponges.

Since the literature had already found that these devices' performance at pressure stimuli depended more on the foams' mechanical and structural properties than on the PEDOT:PSS solution itself, it was decided to further study the devices using high-density foams. After defining the best type of foam, it was necessary to find a way to standardize the manufacturing parameters so that it was possible to reproduce devices with similar performance and detection capabilities.

One of the challenging parts of the manufacturing process was assembling the sensor device since it was necessary to find a way to effectively attach the metal electrodes to the foam, which has a porous and irregular structure. Thus, it was necessary to develop a resistant, flexible, and conductive glue, ensuring contact between foam and electrodes, especially during intensive pressure tests.

It was also essential to verify how the device's internal resistance value and its dimensions affected the sensor's response to pressure and temperature stimuli. Thus, with the manufacturing of PEDOT:PSS(+5%DMSO)@MS devices of different thicknesses, it was possible to evaluate the response to the deformation of these sensors. Once the best dimensions for the devices were defined, sensors were manufactured and evaluated with different concentrations of PEDOT:PSS to obtain devices with different internal resistance values to see how this would affect their performance. Then, having performed pressure and temperature tests to assess the performance of single PEDOT:PSS@MS-based devices and finding a reproducible fabrication method, it was finally possible to manufacture a functional matrix device.

These challenges will be discussed in this dissertation. Initially, the physical concepts of the piezoresistive and thermoelectric effects, and the characteristics of PEDOT:PSS are presented in Chapter 2, while the experimental methods for the fabrication and characterization of devices are presented in Chapter 3. In Chapter 4, the results from the performed pressure (strain-stress) and temperature response tests for single devices, in which it also demonstrates a functional 4x4 matrix fabricated with PEDOT:PSS sponge-based sensor device, is presented. Finally, the conclusions of the work are presented in Chapter 5.

2. PHYSICAL CONCEPTS

2.1 Piezoresistive Effect in Semiconductors

The piezoresistive effect is a physical phenomenon that occurs when a mechanical strain applied to, for example, a semiconductor or metal, results in a change of its electrical resistivity. This effect occurs in conducting and semiconducting materials due to changes in the interatomic spacing affecting the bandgaps, resulting in a change in the material's electrical resistance. Figure 2.1 illustrates how the piezoresistive effect acts on a system constructed with a piezoresistive material (Figure 2.1(a)).

Figure 2.1: Illustration of the piezoresistive effect on a system. (a) Graphical representation of a piezoresistive material attached to electrodes; (b) Illustration showing the presence of variable resistances in the system; (c) A mechanical strain is applied to the system, resulting in a change in its structure and internal resistance.

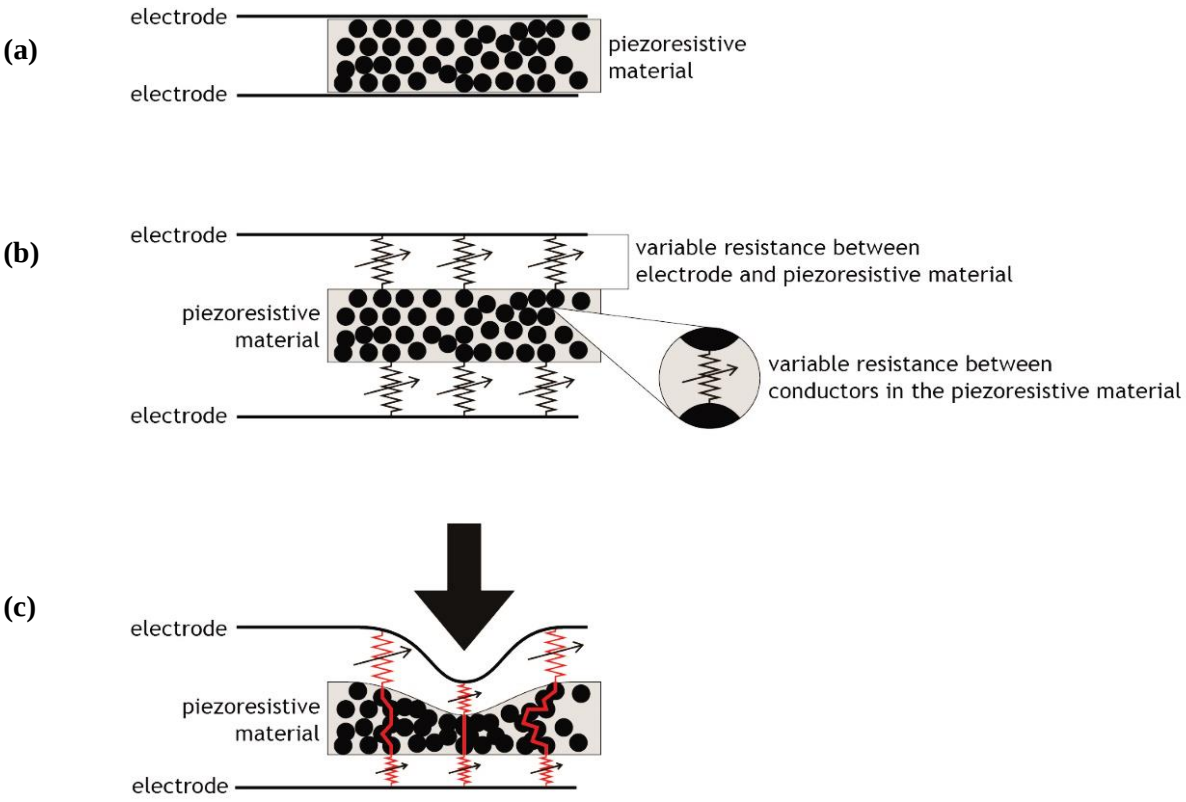

From (PLUSEA, 2019)

Figure 2.1(b) depicts the presence of variable resistances between the electrodes and the piezoresistive material and between conductors in the piezoresistive material itself. Figure 2.1(c) shows that, when the system is under the influence of a mechanical strain (represented by the black arrow), the entire system suffers from a deformation on its structure, thus changing the distances on the inter-atomic spacing and causing a variation of the value of the internal resistances.

When the material of an original cross-sectional area A_0 and original length L_0 is being subjected to a force load *F*, it is experiencing a stress σ defined to be the ratio of the force to the cross-sectional area of the bar:

$$\sigma = \frac{F}{A_0} \tag{1}$$

Due to the applied force load, the dimensions of the material change, and the strain ε is:

$$\varepsilon = \frac{L_0 - L}{L_0} = \frac{\Delta L}{L_0} \tag{2}$$

The SI unit for stress is the newton-per-square-meter, or pascal (1 pascal = 1 Pa = 1 N/m^2), while r strain is dimensionless.

The resistance variation $(R-R_0)/R_0$ for a piezoelectric material is related to strain ε and stress σ due to axial elongation and force loads, respectively, suffered by the material structure under pressure stimulus.

For semiconductor materials, the value of $(R-R_0)/R_0$ can be many orders of magnitude larger than $(L_0-L)/L_0$. Hence, it is possible to build semiconductor strain gauges with remarkably high sensitivity. Since semiconductor strain gauges are sensitive to environmental conditions (especially temperature), their use for precision measurements becomes more challenging than metal strain gauges.

A piezoresistive sensor, which transduces the external pressure into a resistance signal, has the advantage of simple fabrication, low cost, and easy signal acquisition. The literature has demonstrated flexible piezoresistive pressure sensors using conductive elastomeric composites or conductive porous sponges. In these sensors, under compressive forces, more conductive pathways are formed in the conductive elastomeric composites or sponges, resulting in a resistance decrease in the sensors; this transduction mechanism is known as the negative piezoresistive effect (DING *et al.*, 2018).

2.1.1 Stress-Strain Curve for Elastomeric Foams

The typical display of the relationship between *stress* and *strain* is a unique curve for each material, found by recording the amount of deformation (strain) at distinct intervals of various loadings (stress). These curves reveal the material's properties (including data to estimate the modulus of elasticity, *E*).

The stress-strain curve refers to the relationship between normal-axial stress and normal-axial strain of materials measured in a tension test. Stress-strain responses of foams in compression tests show comparable properties for distinct types of foams.

Figure 2.2 shows a typical schematic compressive stress-strain response for an elastomeric foam (VRIES, 2009).

Figure 2.2: Schematic compressive stress-strain response for elastomeric foams

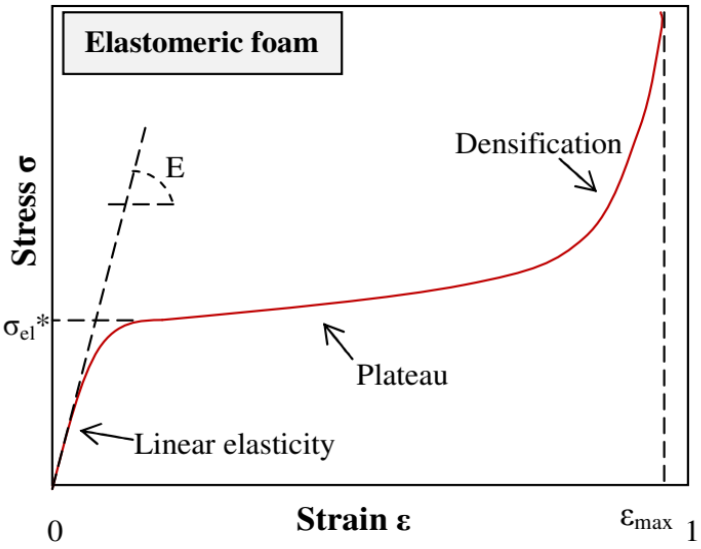

From (VRIES, 2009)

In compression tests, the stress-strain responses describe a region of *linear elasticity* (Hookean) at low stresses followed by a long collapse plateau in which the stresses do not significantly vary, truncated by a region of densification in which the stress rises steeply. The definition of each region occurs by some mechanism of deformation (VRIES, 2009).

Young's modulus *E* is the first slope of the stress-strain response of the polymer foam. For small strains, the foam has an elastic response. In this region, the compressive stress can be determined by (VRIES, 2009):

$$\sigma = E \cdot \varepsilon \quad (3)$$

In compression, the *plateau* is associated with the collapse of the cells, and, for an elastomeric foam, it is determined by elastic buckling. Note that, for a pure elastomeric foam, there is no plastic deformation (VRIES, 2009).

When the cells are close to de completely collapsed, opposing cell walls touch and further strain compresses the solid itself, giving the final region of rapidly increasing stress, referred to as *densification*. Increasing the relative density of the foam increases Young's modulus, raises the plateau stress, and reduces the strain at which densification begins (VRIES, 2009).

2.2 Thermoelectric Effect in Semiconductors

The thermoelectric effect (TE) is a physical phenomenon that consists of the direct conversion of temperature differences to voltage and vice versa. Thermoelectric devices create a voltage when there is a difference in temperature on each side. Conversely, when applying a voltage on it, heat transfer occurs from one side to the other, thus generating a temperature difference. One of the applications of such an effect is to measure the temperature of objects precisely.

To better understand how the thermoelectric effect works in semiconductors, it should be considered that one side of a long rod of an N-type or P-type semiconductor is heated, while the temperature on the other side is maintained at a lower temperature *T*, as shown in Figure 2.3. The electrons and holes move faster on the hot side, resulting in the diffusion of electrons/holes towards the cold side.

The *Seebeck effect* occurs when an electric field E_{emf} sets up across the rod due to the diffusion of charge carriers caused by the applied temperature gradient. The voltage found for a temperature difference, ΔT, under equilibrium, is $S_T \Delta T$, in which S_T is the *Seebeck coefficient* (or thermopower), a property of the local material, given in μV/K.

Figure 2.3: Graphical representation of the thermoelectric effect in semiconductors. For each type of semiconductor, the circles are the mobile charges while the squares the fixed ones.

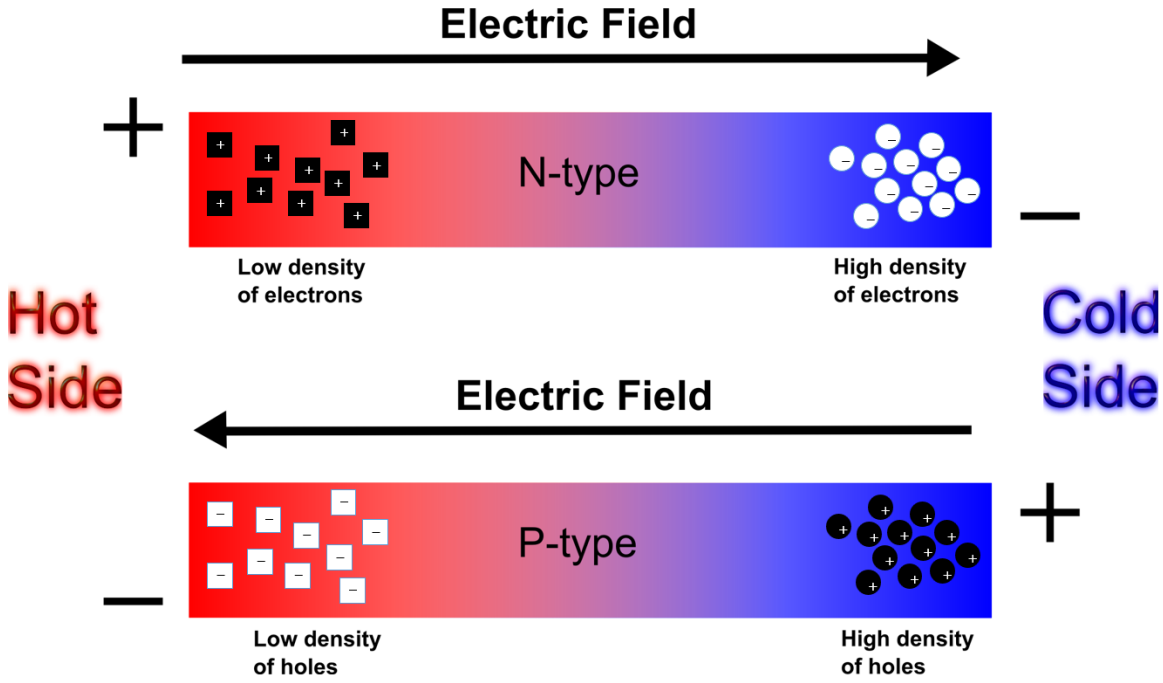

Modified from (UIO: DEPARTMENT OF PHYSICS, 2012)

2.2.1 Seebeck Effect

The *Seebeck* effect is a classic example of an electromotive force (EMF). The effect leads to measurable currents or voltages in the same way as any other EMF. In that way, the current density J is:

$$J = \sigma_c(-\nabla V + E_{emf}) \tag{4}$$

V is the voltage, and σ_c is the conductivity. It is possible to define the *Seebeck* effect by the generation of an electromotive field, due to a temperature gradient ∇T, as:

$$E_{emf} = -S_T \nabla T \tag{5}$$

2.2.2 Seebeck Coefficient

The magnitude and sign of the *Seebeck* coefficient can be physically understood as being given by the entropy per unit charge carried by electrical currents in the material, which can be positive for positively charged carriers, as the holes (S_T>0 for *p*-type thermoelectric

semiconductors) or negative for negatively charged carriers, as the electrons ($S_T < 0$ for *n*-type semiconductors) (HOFMANN; KROON; MÜLLER, 2019).

In summary, it is possible to define the *Seebeck* coefficient as the voltage built up when a material suffers a small temperature gradient and when the material has come to a steady-state where the current density is zero everywhere (i.e., $J = 0$). In that way, from (4) and (5), ∇V can be written as:

$$\nabla V = E_{emf} = -S_T \nabla T \tag{6}$$

If the temperature difference ΔT between the two ends of the material is small, it is possible to define its *Seebeck* coefficient from eq. (6) as:

$$S_T = -\frac{\Delta V}{\Delta T} \tag{7}$$

Here, ΔV is the thermoelectric voltage seen at the terminals. Table 2.1 shows the values of *Seebeck* coefficients for semiconductors.

Table 2.1: Seebeck Coefficients for some Semiconductors.

Semiconductors	Seebeck Coefficient
	μV/K
Se	900
Te	500
Si	440
Ge	300
n-type Bi_2Te_3	-230
p-type $Bi_{2-x}Sb_xTe_3$	300
p-type Sb_2Te_3	185
PbTe	-180
$Pb_{03}Ge_{39}Se_{58}$	1670
$Pb_{06}Ge_{36}Se_{58}$	1410
$Pb_{09}Ge_{33}Se_{58}$	-1360
$Pb_{13}Ge_{29}Se_{58}$	-1710
$Pb_{15}Ge_{37}Se_{58}$	-1990
$SnSb_4Te_7$	25
$SnBi_4Te_7$	120
$SnBi_3Sb_1Te_7$	151
$SnBi_{2.5}Sb_{1.5}Te_7$	110
$SnBi_2Sb_2Te_7$	90
$PbBi_4Te_7$	-53

From (THE SEEBECK COEFFICIENT | ELECTRONICS COOLING, *[s. d.]*)

2.3 Organic Thermoelectric Material PEDOT:PSS

Organic thermoelectric materials have advantages when compared to inorganic counterparts, such as mechanical flexibility, low cost, lightweight, and processability over large areas. The intrinsically low thermal conductivity of organic materials, which is ∼2 to 3 orders of magnitude lower than those of the inorganics, turns these materials into potential candidates for high-performance TE applications (MENGISTIE *et al.*, 2015).

The *Poly(3,4-ethylenedioxythiophene)-poly(styrenesulfonate)* (PEDOT:PSS) is a polymer mixture of two ionomers (polymer composed of repeated units of both electrically neutral repeating units and ionized units). The PEDOT component, *Poly(3,4-ethylenedioxythiophene)*, is a conjugated polythiophene polymer that carries positive charges. In contrast, *Poly(styrenesulfonate)* makes up the PSS component, which is sulfonated polystyrene, and part of those sulfonyl groups are deprotonated and carry a negative charge (GROENENDAAL *et al.*, 2000).

Figure 2.4: The PEDOT:PSS, a high-efficiency organic thermoelectric material.

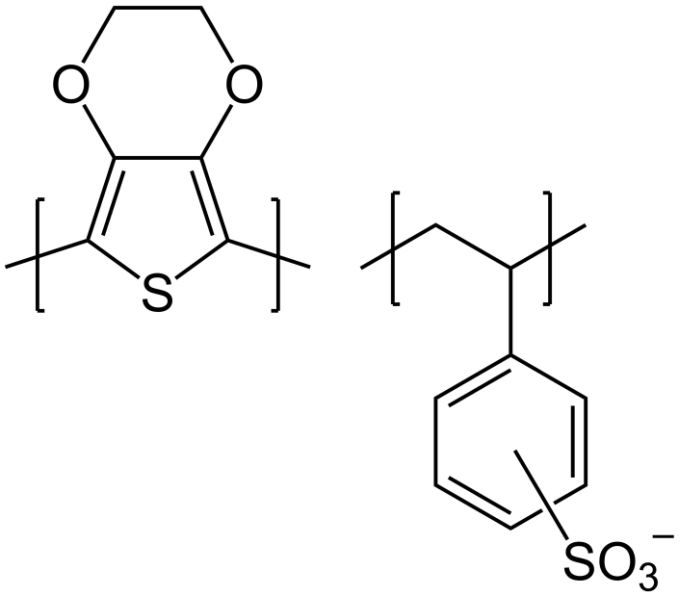

From (FILE:POLYTHIOPHENES_PEDOTPSS @ COMMONS.WIKIMEDIA.ORG, *[s. d.]*)

PEDOT:PSS has the highest electrical efficiency among conductive organic thermoelectric materials, which allows its use on flexible and biodegradable thermoelectric generators (SATOH et al., 2018). In addition to its high conductivity, PEDOT:PSS displays

other advantages: high transparency and thermal stability. Its most extensive application is as a transparent, conductive polymer. For example, AGFA coated 200 million photographic films per year with a thin layer of transparent and colorless PEDOT:PSS as an antistatic agent to prevent electrostatic discharges during production and regular film use, independent of humidity conditions.

It is possible to increase the conductivity of PEDOT:PSS by many orders of magnitude with the addition of organic compounds, including high boiling solvents like methyl pyrrolidone, dimethyl sulfoxide, ionic liquids, and surfactants (DÖBBELIN *et al.*, 2007; OUYANG *et al.*, 2004). This conductivity increasing of PEDOT:PSS makes it also suitable as a transparent electrode, for example, in touchscreens, organic light-emitting diodes, and flexible organic solar cells to replace the commonly used indium tin oxide (ITO) (PARK *et al.*, 2016). PEDOT can exhibit conductivities ranging from 10^{-2} to 3500 S/cm, and even PEDOT:PSS typically having low conductivity (<10 S/cm) (CRISPIN *et al.*, 2006), and it can also be significantly improved by a post-treatment with various compounds, such as ethylene glycol (EG) and dimethyl sulfoxide (DMSO) (SAGHAEI; FALLAHZADEH; SAGHAEI, 2015; SAGHAEI; FALLAHZADEH; YOUSEFI, 2015). This conductivity is comparable to that of ITO, a well-known transparent electrode material, and it can triple value that of ITO after the embedding of a network of carbon nanotubes and silver nanowires into PEDOT:PSS (STAPLETON *et al.*, 2015).

The typical application of PEDOT:PSS is a dispersion of gelled particles in water. A conductive layer on glass is obtained by spreading a layer of the dispersion on the surface, usually by spin coating and driving out the water by evaporation. It is possible to develop special PEDOT:PSS inks and formulations for different coating and printing processes. It is also common to use water-based PEDOT:PSS inks in slot dye coating and inkjet printing.

The value of the *Seebeck* coefficient of PEDOT:PSS is generally in the 15–20 μV/K range (MASSONNET *et al.*, 2014). Unlike inorganic TE materials, electrical conductivity enhancement in PEDOT:PSS has a small effect on the *Seebeck* coefficient and thermal conductivity. In PEDOT:PSS, only small crystallites are embedded in the amorphous phase, and hence the thermal conductivity shows only a slight variation with conductivity enhancement (MENGISTIE *et al.*, 2015).

3. EXPERIMENTAL DETAILS

3.1 Ellipsometry

Ellipsometry is a non-destructive optical technique that allows the measurement of thin films' properties such as the actual refractive index (n) and the extinction coefficient (κ). It is possible to perform this characterization in isotropic, anisotropic, and dielectric materials, among others. Besides, it is possible to measure thin films' thicknesses that have low absorption with great precision. This technique consists of focusing a polarized light beam on the sample and measuring the change in polarization after interacting with the material through reflection, which allows the user to know the material's physical properties. The relative amplitudes of the components parallel (ρ^p) and perpendicular (ρ^s) to the plane of incidence together with the phase difference between both components ($\Delta^p - \Delta^s$) determines the change in polarization (VEDAM, 1998). The ratio between the reflections of their polarizations defines the parameters Φ and Δ:

$$\frac{r^p}{r^s} = \left(\frac{\rho^p}{\rho^s}\right) \cdot e^{i(\Delta^p - \Delta^s)} = \tan(\Phi) \cdot e^{i\Delta} \tag{8}$$

The use of an experimental arrangement, as displayed in Figure 3.1, for example, allows measuring the parameters Φ and Δ.

Figure 3.1: Schematic setup for an ellipsometry experiment.

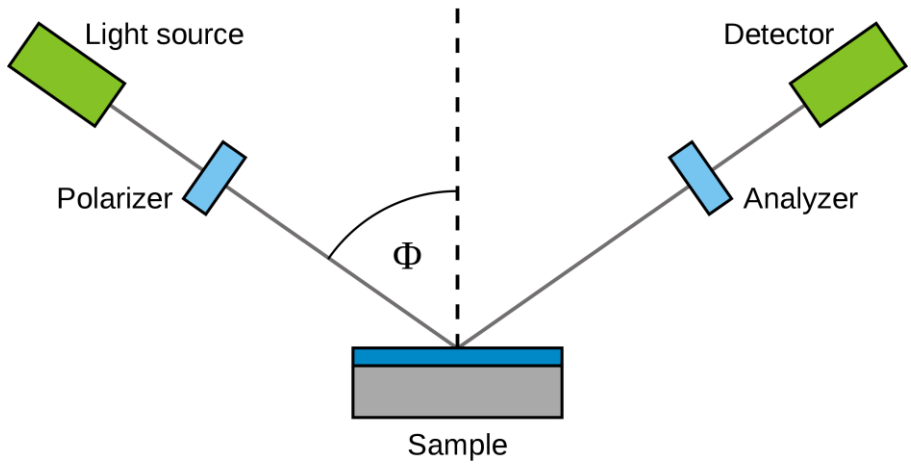

Modified from (FILE:ELLIPSOMETRY_SETUP @ COMMONS.WIKIMEDIA.ORG, *[s. d.]*)

The SOPRA GES-E ellipsometer, shown in Figure 3.2, uses a polychromatic beam that crosses a rotating polarizer (5 Hz frequency) making the beam circularly polarized. The analyzer (another polarizer) is adjusted until reaching a maximum signal in the detector to each wavelength selected in the spectrometer (this maximum signal is obtained by the equipment using *Hadamard* sums). The ellipsometer allows obtaining the optical constants in the spectral range from 0.25 to 1.88 µm, varying the wavelength read in the spectrometer.

Figure 3.2: SOPRA GES-E ellipsometer.

From (SOPRA SA (FRANCE), *[s. d.]*)

This measurement and a model to describe the material investigation is used to obtain the optical constants. In this study, the investigated material is dielectric and isotropic. So a model used to describe the refractive index curve in the visible wavelength range is the *Cauchy* dispersion formula, represented by equation (9) (FUJIWARA, 2007):

$$n(\lambda) = A + \frac{B}{\lambda^2} + \frac{C}{\lambda^4}, \tag{9}$$

where *A*, *B*, and *C* are constants.

The *Winelli II* software, which is used in the equipment, can obtain the film thickness and the refractive index $n(\lambda)$, adjusting the chosen model to the experimental data. The angle of incidence used during the experiments was 75° with the normal. A spectral range from 300 to 800 nm was used in the measurements.

3.2 Resistivity

For semiconductors with both electrons and holes as carriers, the drift current under an applied field is given by:

$$J = \sigma_c \,.\, E_{emf} = q\left(\mu_n n + \mu_p p\right) . E_{emf} \tag{10}$$

The conductivity σ_c is related to the resistivity ρ according to:

$$\sigma_c = \frac{1}{\rho} = q\left(\mu_n n + \mu_p p\right) \tag{11}$$

If *n* >> p, as in *n*-type semiconductors, then:

$$\rho = \frac{1}{q(\mu_n n)} \tag{12}$$

and

$$\boldsymbol{\sigma_c = q(\mu_n n)} \tag{13}$$

The most common method for measuring resistivity is the four-point probe method (Figure 3.3) (SMITS, 1958; W. E. BEADLE, J. C. C. TSAI, 1985).

Figure 3.3: The four-probe method.

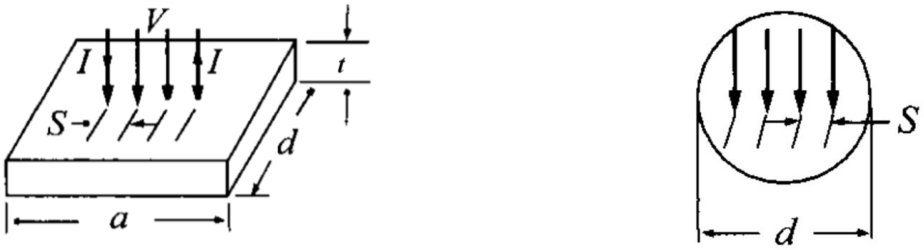

From (SZE; NG, 2007)

With this method, a small constant current *I* passes through the outer two probes, and the voltage *V* measurement occurs between the other inner two probes. For a thin wafer with thickness t much smaller than either dimension a or d, the sheet resistance R_s, with a correction factor *CF*, is given by:

$$R_s = \frac{V}{I} \cdot CF \qquad [\ \Omega\ /\ \text{sq}\ ] \qquad (14)$$

The resistivity ρ is:

$$\rho = R_s\,.\,t \qquad [\ \Omega\text{-cm}\ ] \qquad (15)$$

In the limit, when $d >> S$, where S is the probe spacing, the correction factor becomes $\pi/\ln(2)$ $(= 4.54)$.

3.3 Arduino

Arduino is an open-source hardware and software company, project, and user community that designs and manufactures single-board microcontrollers and microcontroller kits for building digital devices. The Arduino hardware products have a CC-BY-SA license. The software has the GNU Lesser General Public License (LGPL) or the GNU General Public License (GPL), which grants the manufacturing of Arduino boards and software distribution to anyone. Arduino boards are available commercially from the official website or through authorized distributors (INTRODUCTION @ WWW.ARDUINO.CC, *[s. d.]*).

Arduino board designs use a variety of microprocessors and controllers. The boards contain sets of digital and analog input/output (I/O) pins, which allows the interfacing to have various expansion boards ('shields') or breadboards (for prototyping), and other circuits. The boards feature serial communications interfaces, including Universal Serial Bus (USB), for loading programs from personal computers. The microcontrollers can be programmed using the C and C++ programming languages, using a standard API, which is also known as the "Arduino language." In addition to using traditional compiler toolchains, the Arduino project provides an integrated development environment (IDE) and a command-line tool (Arduino-CLI) developed in Go.

Arduino Mega 1280 (pinout diagram on Figure 3.4) is an 8-bit microcontroller board based on the ATmega1280. It has 54 digital input/output pins (of which 14 also work as PWM

outputs), 16 analog inputs, 4 UARTs (hardware serial ports), a 16 MHz crystal oscillator, a USB connection, a power jack, an ICSP header, and a reset button. The Arduino Mega 1280 contains all requirements to support the microcontroller; simply connect it to a computer with a USB cable or power it with an AC-to-DC adapter or battery to get started. Table 3.1 shows the technical aspects of the Arduino Mega 1280 board.

Table 3.1: Arduino Mega 1280 Features.

Microcontroller	ATmega1280
Operating Voltage	5 V
Input Voltage (recommended)	7-12V
Input Voltage (limits)	6-20V
Digital I/O Pins	54 (of which 14 provide PWM output)
Analog Input Pins	16
DC Current per I/O Pin	40 mA
DC Current for 3.3V Pin	50 mA
Flash Memory	128 KB (of which 8 KB used by the bootloader)
SRAM	8 KB
EEPROM	4 KB
Clock Speed	16 MHz

When working with voltage measurements, it is essential to know that the board's microcontroller has a circuit inside called an *analog-to-digital converter* (*ADC)* that reads the changing voltage and converts it to a number between 0 and 1023. When 0 volts reach the pin, the input value is 0. On the other hand, when 5 volts reach the pin, the input value is 1023. When between 0 and 5 volts, *analogRead()* returns a number between 0 and 1023, proportional to the pin's applied voltage. Thus, to convert this number to a voltage value, the *real* output voltage of a circuit read by the Arduino can be programmed as:

$$V_{real} = \frac{sensorValue}{1023.0} \times V_{ref} \ , \tag{16}$$

in which *sensorValue* is a number between 0 and 1023 read by the *analogRead()*. It is possible to set V_{ref} as a fixed value of external reference voltage (between 0.6 and 5 V), which the user defines by setting the *AREF* pin on the board. When using Arduino's board's built-in *POWER* pin, it is also possible to set it as +5 or +3.3V DC.

Figure 3.4: Pinout diagram of the Arduino Mega board.

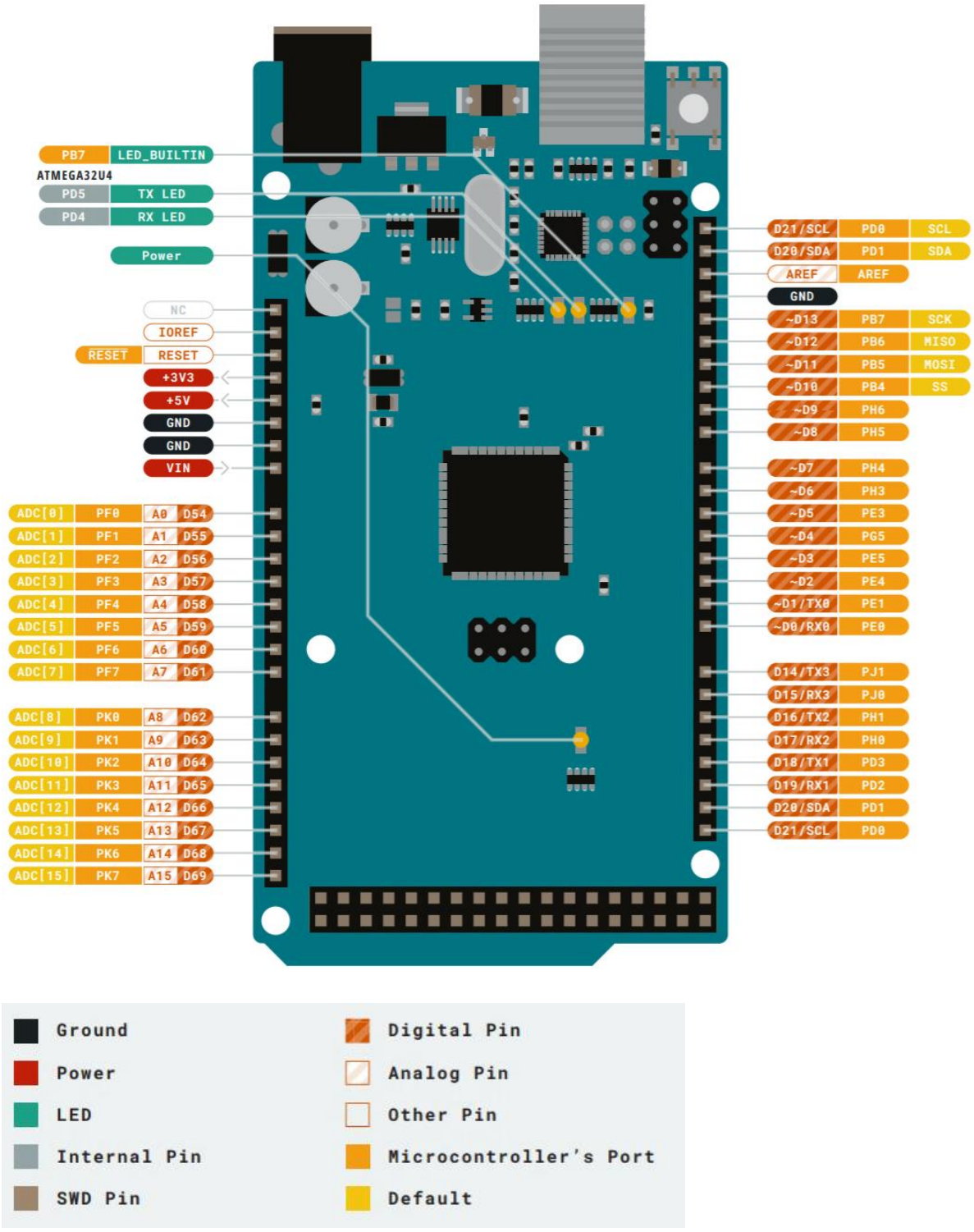

Modified from (ARDUINO.CC, 2020)

3.4 Characterization of the Microstructured Foams

The selection of the flexible microstructured foam to be impregnated with PEDOT:PSS is crucial since the pressure-sensing performance of flexible organic devices relies on the

microstructured material's mechanical and structural properties rather than only the PEDOT:PSS itself (ZHANG *et al.*, 2015). By considering this, an easily found and reliable choice would be a Polyurethane foam (PU) for preliminary tests. Also, it would be preferable to choose higher density foams. In that case, the melamine sponge is the right choice.

To understand how the densities of the foams are related to their pore sizes, it was necessary to perform the slicing of PU foams in pieces with an area of 2.25 cm^2 and thickness of 2.0 mm to execute tests for three different densities of PU foams (Figure 3.5(a-c)): D23, D33, and D45. Respectively, they present densities of 23, 33, and 45 kg of raw material per cubic meter of foam. The same holds for a high-density MS (Figure 3.5(d)). With the help of microscopy imaging, it was possible to estimate the pores' diameter from each of the foams by taking the average value of visible pores with well-defined limits, using a 1 mm scale from a ruler as reference (results on Table 3.2).

Table 3.2: Estimated values of the pore diameter for foams of different densities and materials.

Foam Density	**Estimated Pore Diameter [mm]**
D23 (PU)	0.49 ± 0.16
D33 (PU)	0.36 ± 0.08
D45 (PU)	0.32 ± 0.03
MS	0.09 ± 0.03

It is possible to see that the melamine sponge presents smaller pore sizes and variance than the polyurethane foams, which shows a uniformity to the pore dimensions along with the structure of the sponge. That is an interesting aspect since it shows that MS tends to supply more exact and reproducible results, especially when testing devices for strain-stress relation. Using a material with a denser structure provides better mechanical resistance when under mechanical pressure. For that reason, this work has focused on MS, using PU foams only for preliminary tests.

Figure 3.5: Optical microscopy pictures from the microstructured PU foams (a) D23, (b) D33, and (c) D45, and the melamine sponge, (d) MS.

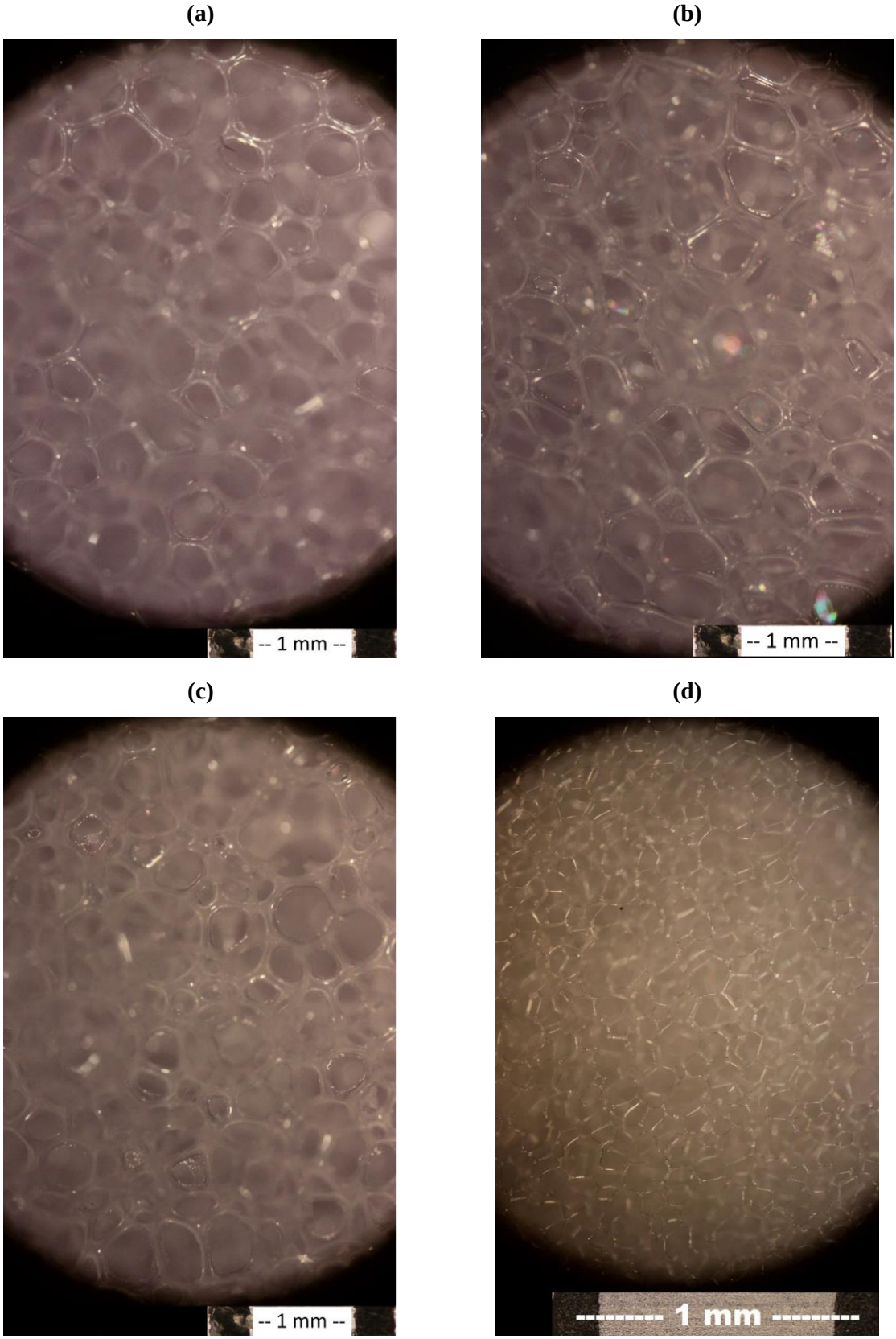

3.5 The procedure of Sensor Preparation

This chapter further discusses the chosen method, based on the literature, to fabricate the proposed sensor devices. For the preparation process for a single sensor device, it was necessary to perform the cutting of small foam squared pieces with an area of 2.25 cm^2, sufficient to fit a fingertip. Also, to assess how thick the foam should be, it was necessary to make sensor devices with different thicknesses.

3.5.1 The Dip-Coating Technique

The method used to impregnate the foam structures with PEDOT:PSS polymeric semiconductor material is known as *dip-coating.* Such technique (as depicted in Figure 3.6) is a simple, low-cost, reproducible, and effective method that involves the deposition of a wet liquid film by immersion of the substrate into a solution and its withdrawal into an atmosphere. After removing the substrate from the solution, the deposition of the homogeneous liquid occurs on the substrate. It is necessary to submit the substrate to dry, thus eliminating volatile solvents and the occurrence of possible chemical reactions. The final result is a thin film coating (NEACŞU *et al.*, 2016) or, in the case of microstructured foams, a uniform impregnation of the porous material.

Figure 3.6: Graphical representation of the dip-coating technique.

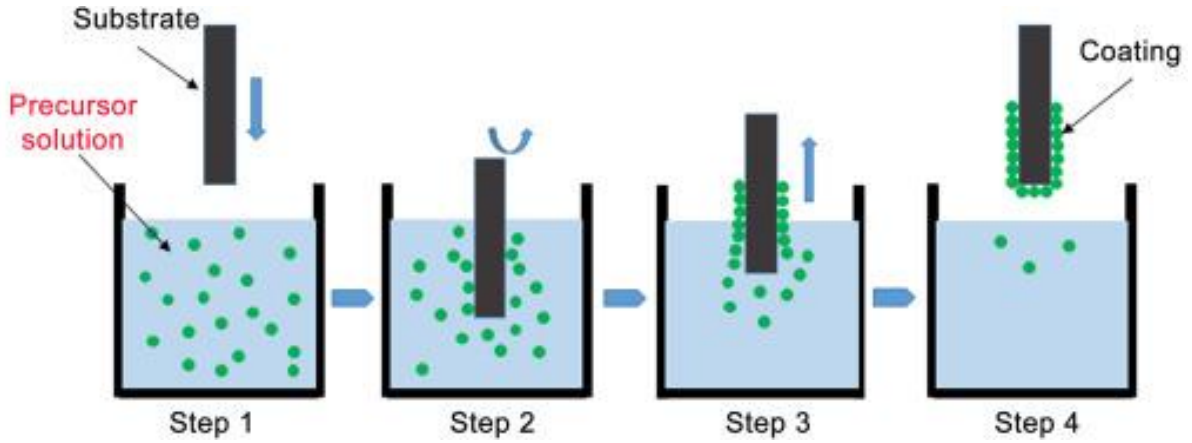

From (NEACŞU *et al.*, 2016)

3.5.2 Impregnating PU and MS structures with PEDOT:PSS

The solution used to impregnate the PU and MS from structures was the high-conductivity grade PEDOT:PSS, dispersed in water, from *Sigma Aldrich* (see Product Specifications on Appendix 6.1).

The construction of the proposed sensor devices began by using a utility blade to manually slice square pieces of 1.5x1.5 cm^2 of both density D45 microstructured polyurethane foam and high-density melamine sponges (having thicknesses of 2, 3, 5, 7.5, and 10 mm), followed by their washing in deionized water and blow-drying using a nitrogen gun.

The PU foams received a one-step dipping in a PEDOT:PSS dispersion (having 5 vol% EG), and they were dried at 100 °C for 10 minutes. As a result, the PU pieces became uniformly impregnated with the PEDOT:PSS film, thus generating the PEDOT:PSS@PU material.

Similarly, it was necessary to perform the dipping of MS pieces in a PEDOT:PSS dispersion for 15 minutes, with three different concentrations for the impregnation: one having 5 vol% DMSO, another having the *original dispersion* of PEDOT:PSS, and a third one *diluted* in 9 parts of H_2O. After removing the samples' excess solution, they were dried in the air on a hot plate at 100 °C for one hour to obtain a PEDOT:PSS@MS conductive sponge.

Table 3.3 shows a summary of the fabrication recipes for the sensors with PEDOT:PSS, which produce the desired conductive foam devices PEDOT:PSS@PU and PEDOT:PSS@MS, similarly to the process depicted in

Figure 3.7. Note that the darker the foam structure becomes, the stronger is the impregnation with PEDOT:PSS.

Table 3.3: Summary of the fabrication methods for the PEDOT:PSS-foam-based devices.

Solution Concentration: 0.5-1 wt. % (PEDOT:PSS* in water)	**Substrate Foam**	**Area**	**Thickness**	**Dip-coating**	**Drying @ 100ºC**
+ 5 vol% EG	Polyurethane (Density 45)	2.25 cm^2	2 mm	< 1 min	10 min
+ 5 vol% DMSO	Melamine		2, 3, 5, 7.5, 10 mm	15 min	1 h
Original Dispersion			2.5 mm		
Diluted in 9 parts of H_2O					

* *Poly(3,4-ethylenedioxythiophene)-poly(styrenesulfonate)* – high-conductivity grade (*Sigma-Aldrich* – Product No. 900181)

Figure 3.7: Schematic for preparing the PEDOT:PSS-coated melamine sponge (PEDOT:PSS@MS) by a simple dip-coating process.

From (DING *et al.*, 2018)

3.5.3 Device Assembling

For the PEDOT:PSS@PU, the impregnated materials are assembled into dual-parameter sensors by putting them between two thin copper plates (with a thickness of 0.1 mm each), which work as electrodes (Figure 3.8(a)), using silver conductive glue to attach the electrodes to the foam structure.

Similarly, for PEDOT:PSS@MS, the sensor is prepared by connecting a piece of flexible *copper laminate polyamide* (with a thickness of 0.1 mm) on the top part of the conductive sponge and a hard copper plate on the bottom, all using a flexible conducting glue. Figure 3.8(b) shows one of the fabricated PEDOT:PSS@MS devices. On both electrodes are soldered thin copper wires for connecting.

The flexible conducting glue was prepared by mixing contact glue (which has Aliphatic Solvent, Oxygenated Solvents, Synthetic Resins, Synthetic Rubbers, and Additives on its composition) with graphite powder and toluene as solvent, providing a proper attachment between the electrodes and the foam structure.

Figure 3.8: Pictures of the PEDOT:PSS sponge-based sensor devices, both with an area of 2.25 cm^2. (a) One of the first assembled PEDOT:PSS@PU sensor devices, using D45 foam. Inset: Graphical representation of the device in the pristine state; (b) A PEDOT:PSS(diluted)@MS sensor device.

(a)

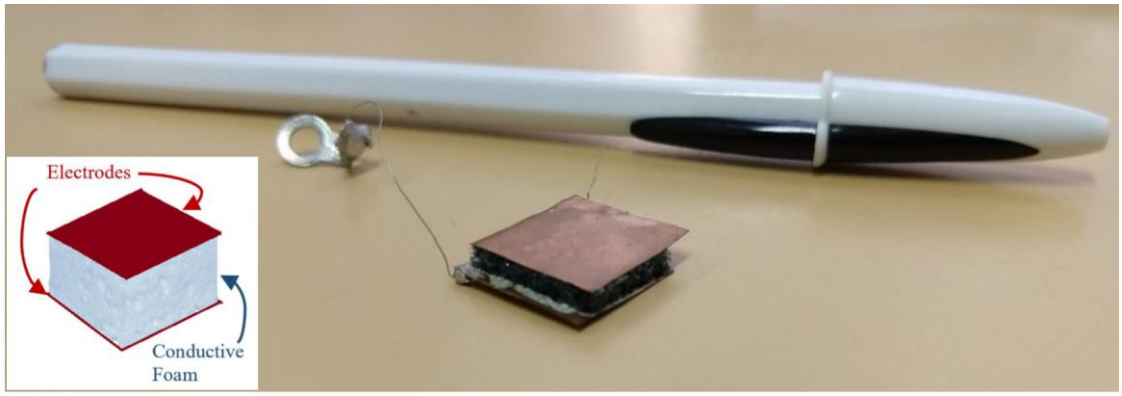

(b)

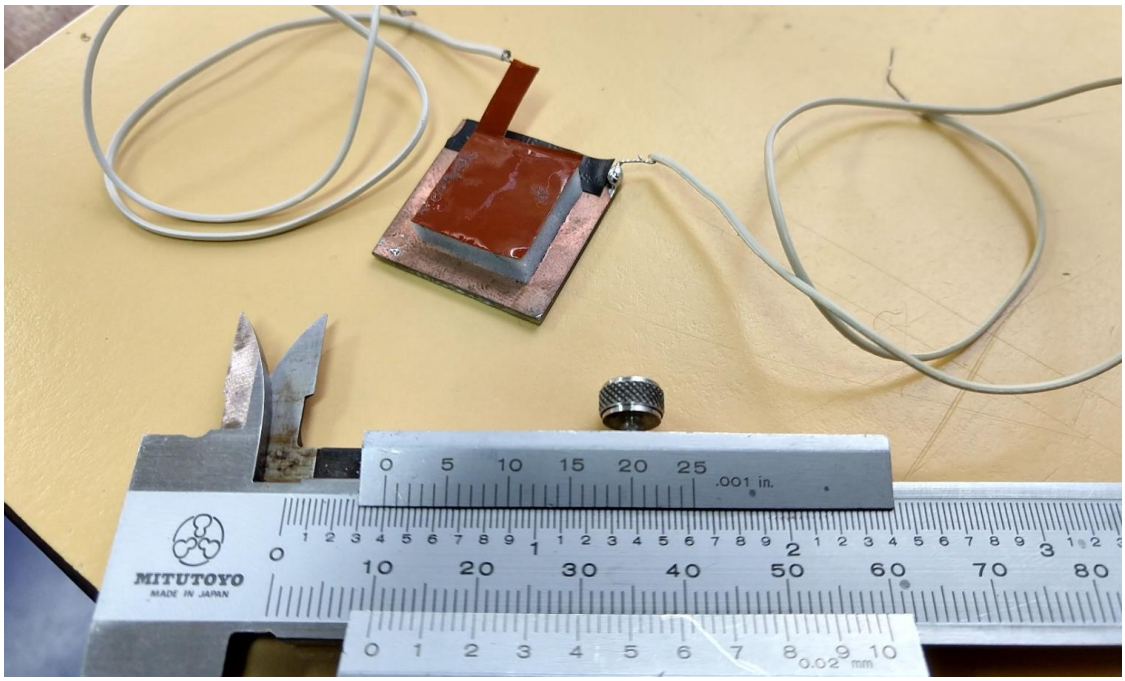

4. RESULTS AND DISCUSSION

4.1 Characterization of PEDOT:PSS Films Deposited on Silicon Wafers

To better understand the PEDOT:PSS's electrical properties, it is possible to estimate its conductivity σ_c (in S/cm) using four-probe measurements. This method allowed finding the resistivity ρ (in Ω.cm) for a PEDOT:PSS film by measuring its sheet resistance R_s. If the film thickness t (in cm) is known, it is possible to calculate its bulk resistivity using eq. (15). From eq. (11), since the conductivity is the inverse of resistivity, it is possible to rewrite equation (15) as:

$$\sigma_c = {}^{1}/_{(R_s.\,t)} \tag{17}$$

PEDOT:PSS films were deposited by spin-coating on SiO_2/Si wafers at 2000 and 4000 rpm for 50 seconds and annealed at a temperature of 100 ºC for 5 min in the air. For increasing conductivity, a solution of PEDOT:PSS containing 5 vol% of ethylene glycol (EG) was also deposited by spin-coating at 2000 rpm in SiO_2. With the thickness of the films measured on ellipsometry (see 3.1), it was possible to extract the sheet resistance values using the four-point method (see 3.2). Table 4.1 shows the conductivity results for PEDOT:PSS films, calculated using equations (15) and (17).

Table 4.1: Estimated values for the thickness, refractive index, sheet resistance, and conductivity for the PEDOT:PSS films deposited on SiO_2 @ 2000 RPM and 4000 rpm via spin-coating.

Spin-coating [rpm]	***t* [nm]**	***n* @ *λ* = 550 *nm***	**R_s [kΩ/sqr.]**	**σ_c [S/cm]**
2000	88.9 ± 1.4	1.54	1.63	69
4000	54.7 ± 0.6	1.56	0.99	185
2000	89.5 ± 1.4	1.54	0.37	302*

* +5 vol% EG

4.2 Signal Conditioning

Arduino's 10-bit ADC use allowed for real-time data acquisition for accurate measurements of resistance and voltage variations for sensor devices under pressure and temperature stimuli over time.

4.2.1 Resistance Measurements

A simple voltage divider was built according to Figure 4.1 to measure the response of the sensor device's resistance variation when under pressure stimuli.

Figure 4.1: A schematic of the Arduino system used to measure the resistance variation response of the fabricated PEDOT:PSS devices when under pressure stimulus.

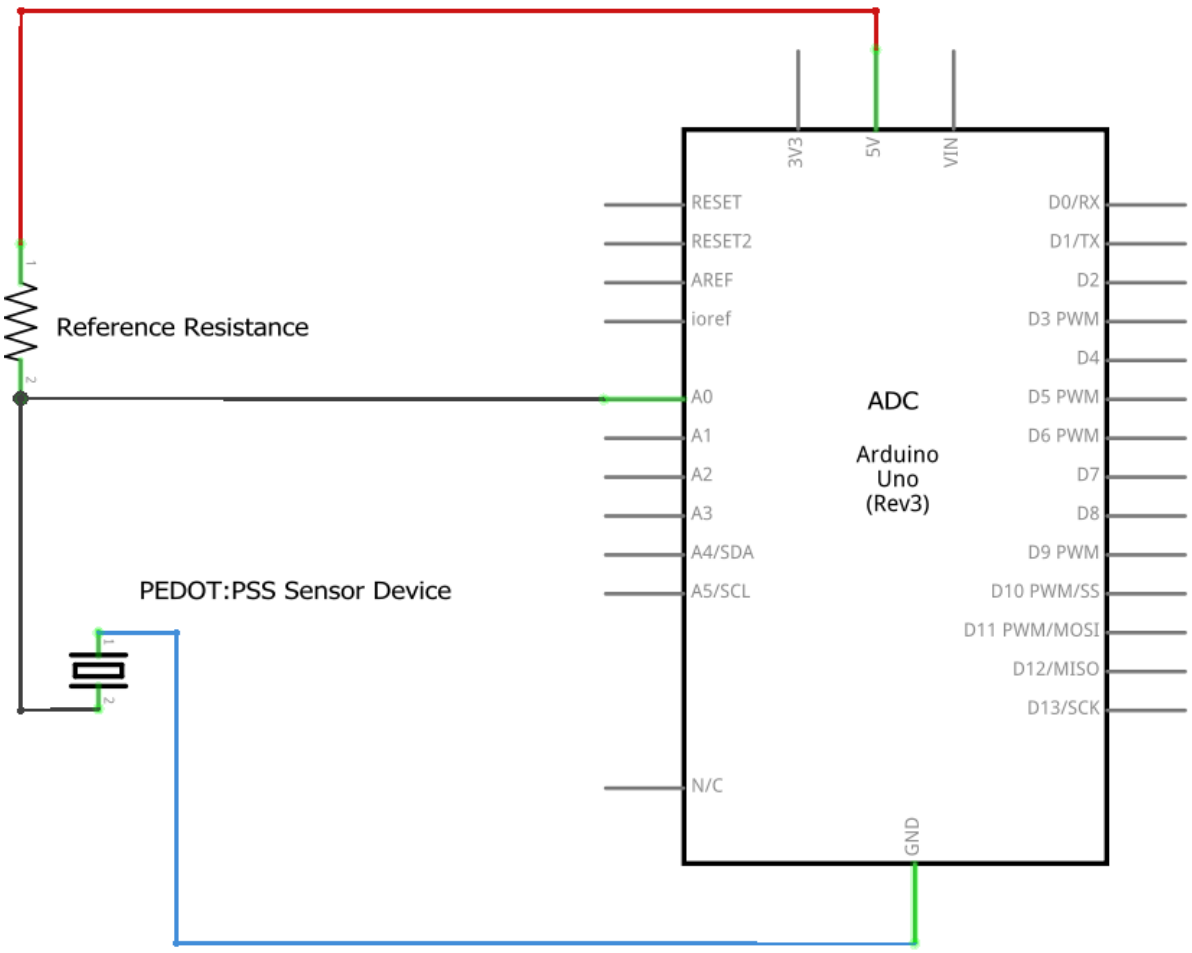

Once a known reference resistor is set up with a fabricated PEDOT:PSS sensor device, the Arduino measures the voltage, using the microcontroller's built-in power pin as the input voltage +5 V DC for the circuit. The board's programming sets the analog pin A0 of Arduino to read the voltage between the reference resistor and the device's internal resistance over time (see Appendix 0). The system performs real-time measurements of resistance variations, each 100 ms. From the resistive divider, the output voltage on A0 was:

$$V_{out} = \frac{R_2}{R_1 + R_2} \times V_{in} = \frac{R_{Ref}}{R_{Sensor} + R_{Ref}} \times (+5) \tag{18}$$

From eq. (16), it was possible to define the output voltage as:

$$V_{out} = \frac{analogRead(0)}{1023.0} \times (+5) \tag{19}$$

Where *analogRead* returns a number between 0 and 1023. From equations (18) and (19), the internal resistance value for the PEDOT:PSS sensor device is given, in ohms, by:

$$R_{Sensor} = R_{Ref} \times \left(\frac{1023.0}{analogRead(0)} - 1\right) \tag{20}$$

As a preliminary test, it was possible to perform a qualitative measurement to compare the resistance variation for two different single sensor devices (preparation procedures in Table 4.2) by submitting them to finger pressing tests (see Figure 4.2). The devices' fabrication included a polyurethane microstructured foam, dip-coated in a solution of PEDOT:PSS + 5 vol% EG, and a high-density melamine sponge dip-coated in a solution of PEDOT:PSS + 5 vol% DMSO. The devices received three pressings, and the signal acquisition interval was of 100 milliseconds.

The PEDOT:PSS(+5%EG)@PU(D45) presented a pristine internal resistance R_0 = 522 Ω, while the PEDOT:PSS(+5%DMSO)@MS presented R_0 = 13 Ω. Figure 4.2 shows the relative variation of the resistances. The maximum relative resistance variation for devices fabricated on PU and MS was about -40% and -30%, respectively, not depending on the absolute resistance value.

Table 4.2: Summary of preparation regimes and performance for sensor devices fabricated with PU and MS.

	PU	**MS**
Microstructured material	D45 Polyurethane foam	High-density melamine sponge
Device area	2.25 cm^2	2.25 cm^2
PEDOT:PSS	+ 5 vol% Ethylene-glycol	+ 5 vol% DMSO
Dip-coating	< 1 min	15 min
Drying	10 min @ 100°C	1 hour @ 100°C
Ro	522 Ω	13 Ω
Max. ΔR/Ro	-40%	-30%

It was possible to notice that the signal from the MS device is much smoother than the one fabricated with PU, due to selecting the reference resistors for both devices, corresponding to different voltage discretization in the 10 bits ADC.

Figure 4.2: resistance response to pressure stimuli over time for PEDOT:PSS(+5% EG)@PU(D45) and PEDOT:PSS(+5%DMSO)@MS devices.

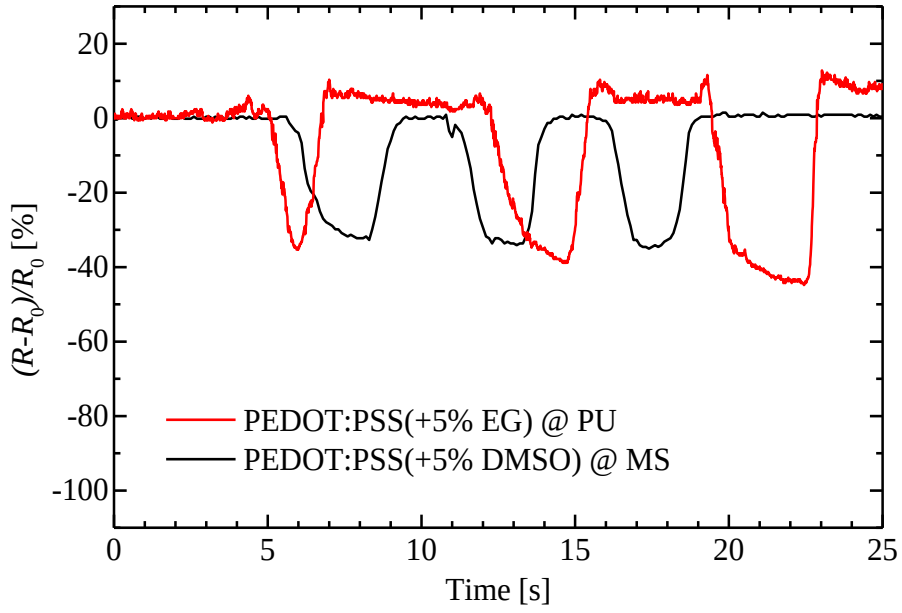

4.2.2 Voltage Measurements

The Arduino microcontroller was programmed to work as a voltmeter, setting the *analog pin A1* to read the value of the generated voltage on the fabricated PEDOT:PSS sensor device during the stimulus of a heat source (see Appendix 6.3). Since the expected voltage response was of the order of millivolts, a 50x Voltage Amplifier was required; otherwise, the signal would be too small for Arduino to read. A better signal resolution was obtained by using an external reference to the Arduino's AREF pin with the value of 0.6 V (the lowest reference value detectable by the board). Figure 4.3 displays the schematic of the proposed circuit.

Figure 4.3: A schematic of the Arduino system used to measure the thermal voltage response of the fabricated PEDOT:PSS devices generated when under temperature stimulus.

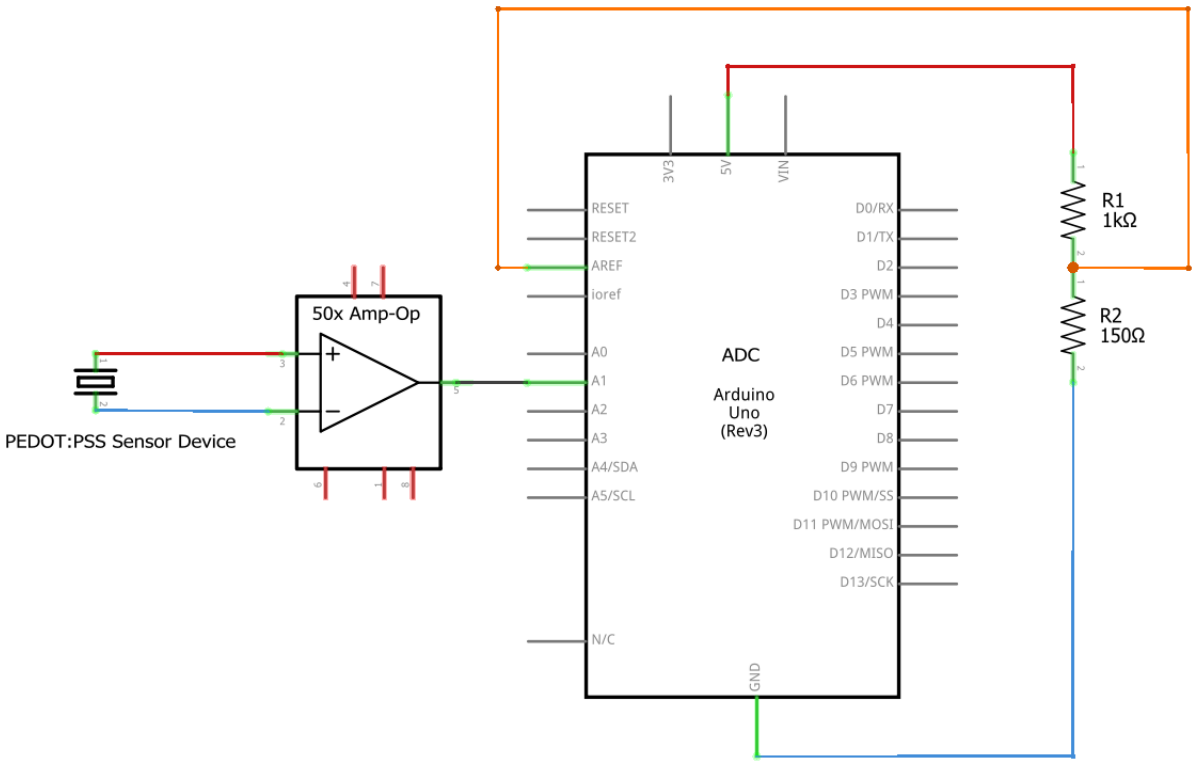

Thus, from eq. (16), the *real* voltage read on *A1* is given by:

$$V_{real} = \frac{analogRead(1)}{1023.0} \times (+0.6) \tag{21}$$

Since there is a 50x amplification of V_{real}, the generated V_{therm} that A_1 reads is given, in millivolts, by:

$$V_{therm} = \frac{1}{50} \times \left(\frac{0.6 \times analogRead(1)}{1023.0} \right) \times 1000 \quad (22)$$

Figure 4.4 presents an example of a real-time conditioned voltage signal collected from a preliminary test for a PEDOT:PSS@PU device. This result shows what happens to the sensor when it receives a finger touch stimulus: it generates a low voltage (less than one millivolt) due to the temperature gradient between the top and bottom of the device, caused by the finger's heat on its surface.

Figure 4.4: Qualitative preliminary result from the generated thermal voltage response to the stimulus of 4 finger-touches (with no pressing) for a PEDOT:PSS(+5%EG)@PU(D45) device.

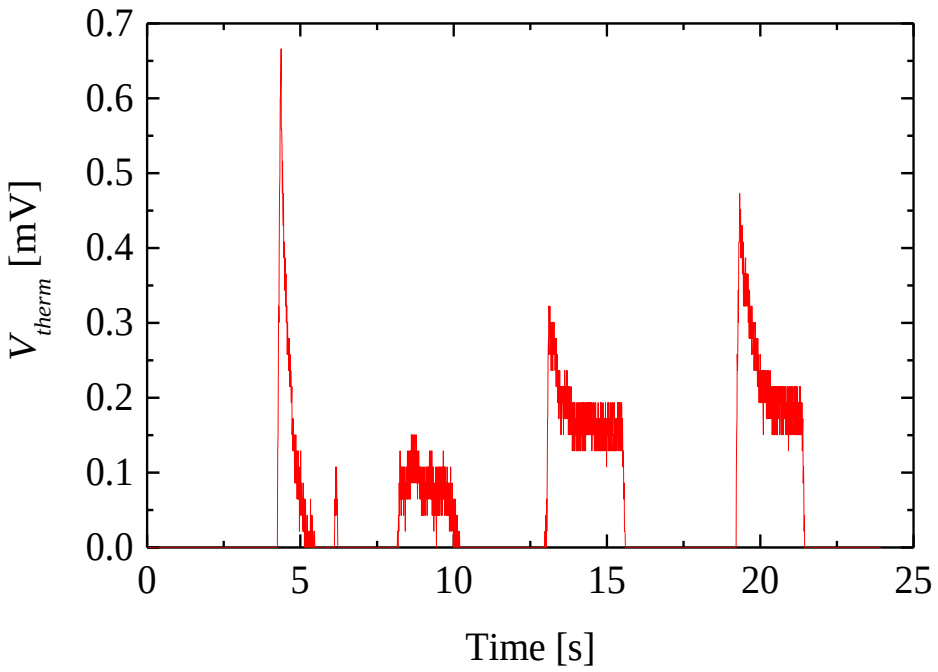

4.3 Setup Instrumentation and Testing Procedures

This section shows the experimental setup for pressure and temperature measurements, and the testing procedures are further discussed, showing some examples of the results for each kind of test for a fabricated PEDOT:PSS@MS device.

4.3.1 Pressure Stimulus

Figure 4.5 shows the assembly of the acquisition system used for pressure response measurements. In this configuration, it was essential to use a high precision potentiometer for better control of the reference value, so that it was possible to match its resistance to a value close to that of the sensor device. Also, it was necessary to perform two different measurements to obtain the stress-strain curve of the devices: one to detect the device's internal resistance variation when it was experiencing the *stress* of a force load distributed on its area A_0 (see Eq. (1)) and other when it was experiencing the *strain* due to axial compression ΔL (see Eq. (2)).

Figure 4.5: The system setup that was used to perform resistance variation measurements for pressure stimuli tests using the Arduino microcontroller.

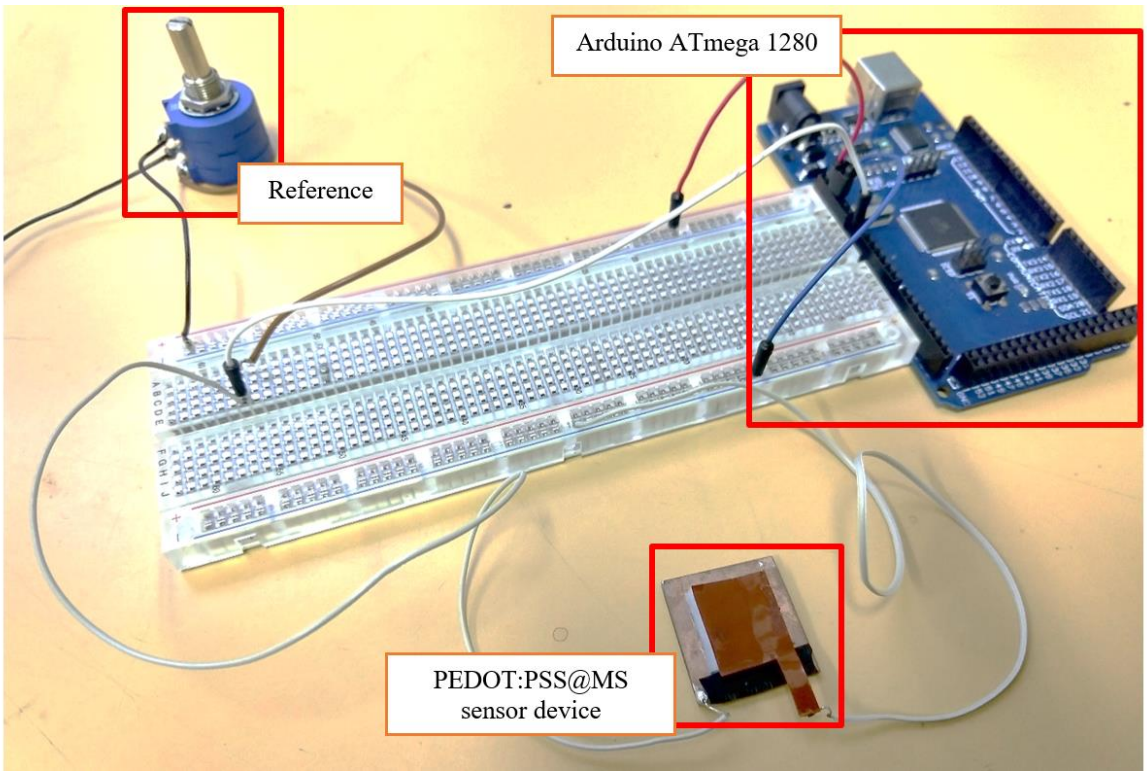

4.3.1.1 Stress Response

For the *stress* response, known loads of 100 g, 200 g, 500 g, 1 kg, 2 kg, and 5 kg (Figure 4.6(a)) were carefully placed on the device, and its resistance was measured using Arduino. The data displayed in Figure 4.6(b) show an example of a result obtained from a stress test for a fabricated sensor device. Note that 1 kg-f/cm^2 = 0.968 atm = 98.067 kPa, so the value for stress, in kilopascal, depends on the area of the device.

Figure 4.6: Stress testing methodology. (a) Weights used to measure the stress response caused by the loads in a fabricated PEDOT:PSS@MS. Inlet: Graphical representation of the device under pressure load stimulus; (b) Example of a percentual resistance variation response.

(a) **(b)**

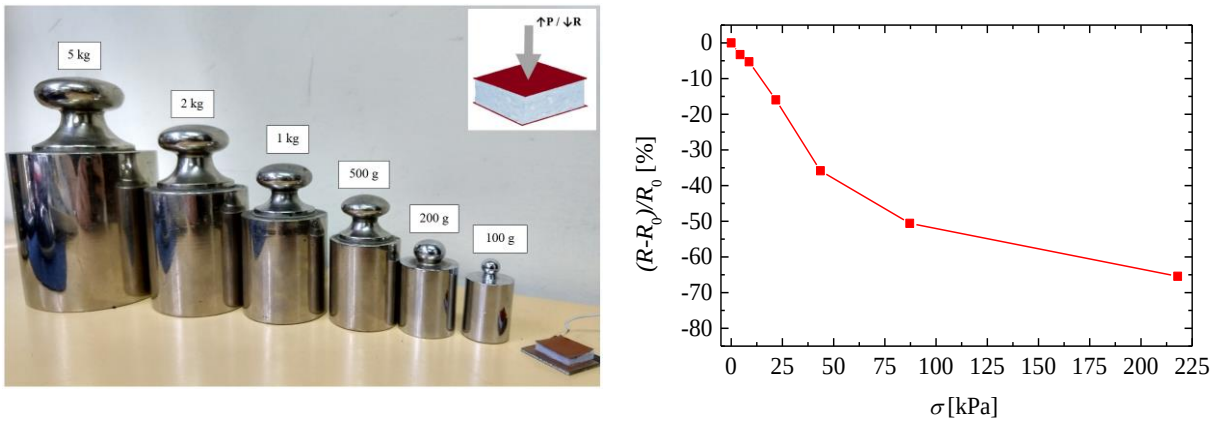

4.3.1.2 Strain Response

Like stress testing, the method chosen to measure the strain response consists of using a horizontally moving micrometer plate (Figure 4.7(a)), which compresses the device at a dislocation L.

The experiment starts from a first position greater than L_0 (start of the compression) and goes as close as possible to its end at dislocation position zero (maximum compression). It was necessary to find the inflection-point position of the extracted curve and infer that this is the middle position of the process ($L_0/2$), as shown in Figure 4.7(b), defining the initial position of the compression process as L_0.

Using eq. (2), it was possible to calculate the strain and Figure 4.7(c) displays the resistance as a function of the strain. Also, the same curve was replotted as the *relative*

resistance variation, considering the value found for R_0. Finally, Figure 4.7(d) shows the relative resistance variation as a function of the strain.

Figure 4.7: Strain testing and plotting methodology. (a) The system used to measure the strain response caused by the micrometer table's dislocation over a fabricated device; (b) Device resistance vs. linear dislocation of the micrometer table; (c) The resistance value of the device as a function of the strain; (d) Relative resistance variation vs. strain.

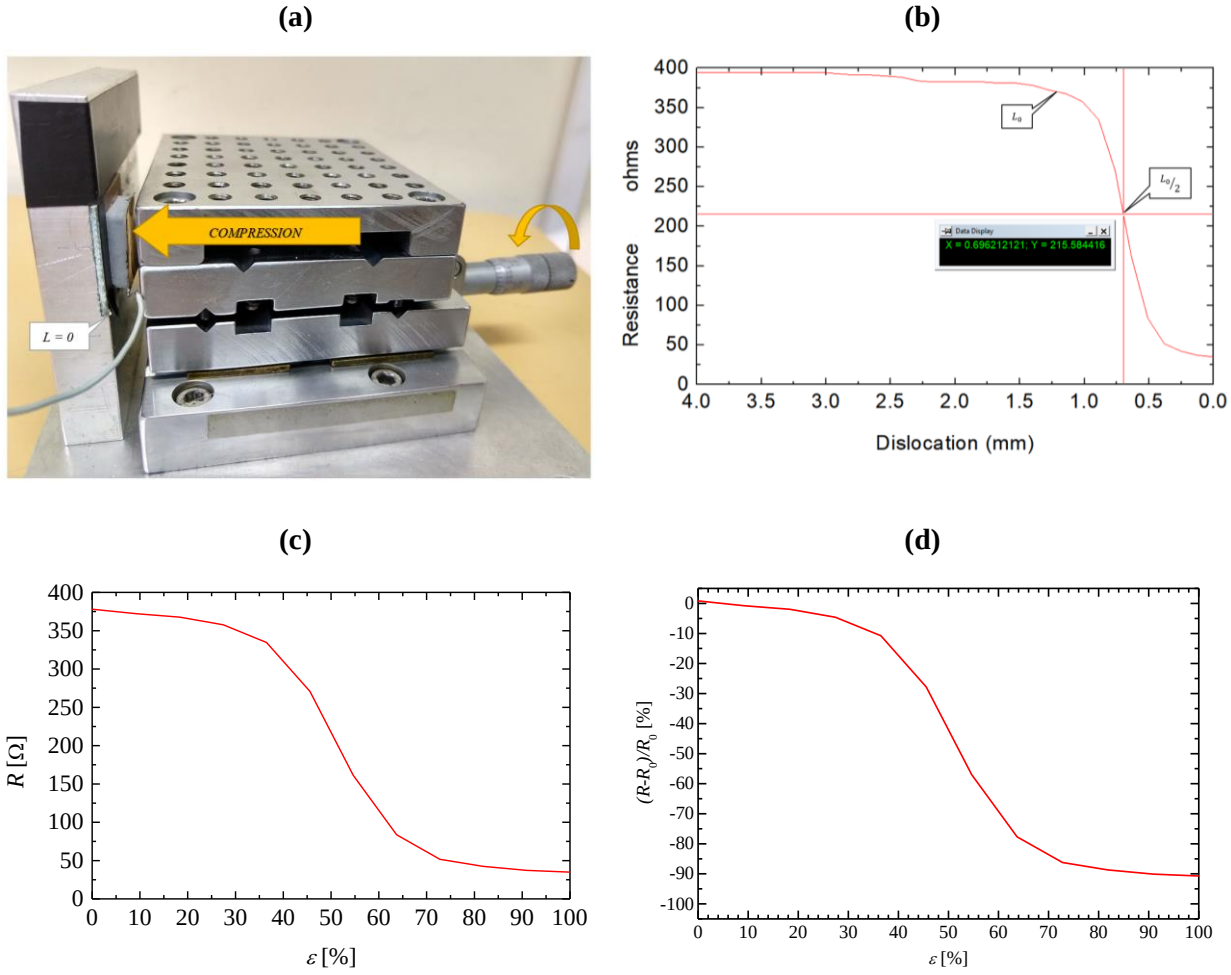

4.3.1.3 Stress-Strain Response

The normalized collected data from both stress and strain measurements as a function of the relative resistance variation are plotted together for comparison (Figure 4.8(a)) to find the sensor device's strain-stress response. Figure 4.8(b) displays an example of the stress-strain curve for the sensor device.

Figure 4.8: Stress-Strain plotting methodology. (a) Normalized data collected from both stress and strain measurements, plotted together as a function of the relative resistance variation, used to construct the stress-strain curve of a PEDOT:PSS@MS sensor device; (b) Strain-stress curve from a PEDOT:PSS@MS sensor device.

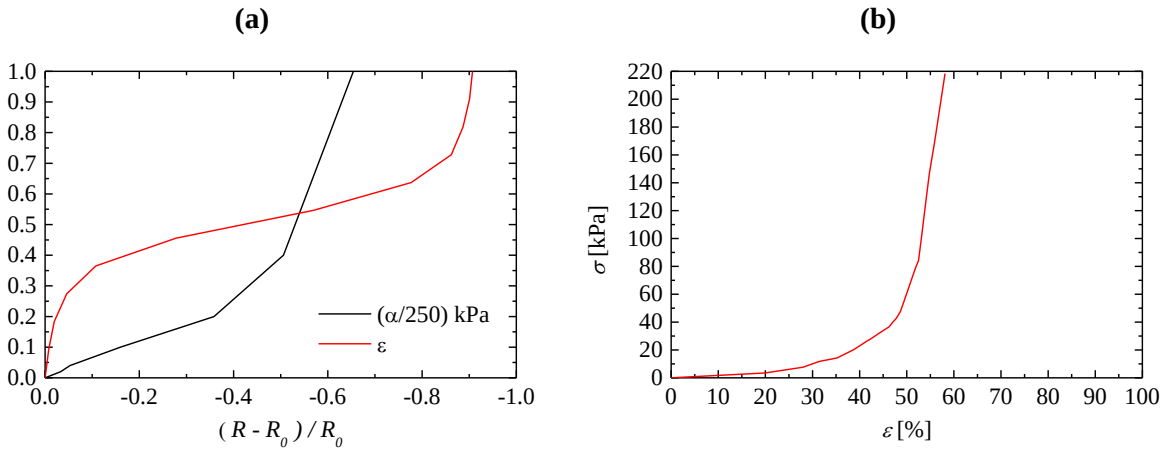

4.3.2 Temperature Stimulus

Figure 4.9 shows the circuit set-up for the acquisition system used for temperature response measurements. This system does not measure the device's actual temperature, but the temperature gradient's thermal voltage. The fabricated sensor device receives a stimulus from a heating source, which causes a temperature gradient ΔT on the device (Figure 4.10(a)). During the heating process, the device generates a thermal voltage V_{therm} in the order of mV, which grows over time as the temperature gradient experienced by the sensor rises (Figure 4.10(b)). Depending on how close the heat source is to the device, the V_{therm} curve suffers some variation. After finding a maximum V_{therm}, the device was left to cool down to observe its thermal inertia.

Figure 4.9: The setup system used to perform V_{therm} measurements using the Arduino microcontroller and Voltage Amplifier. A high-precision potentiometer is present to better control the desired external voltage reference value on this setup.

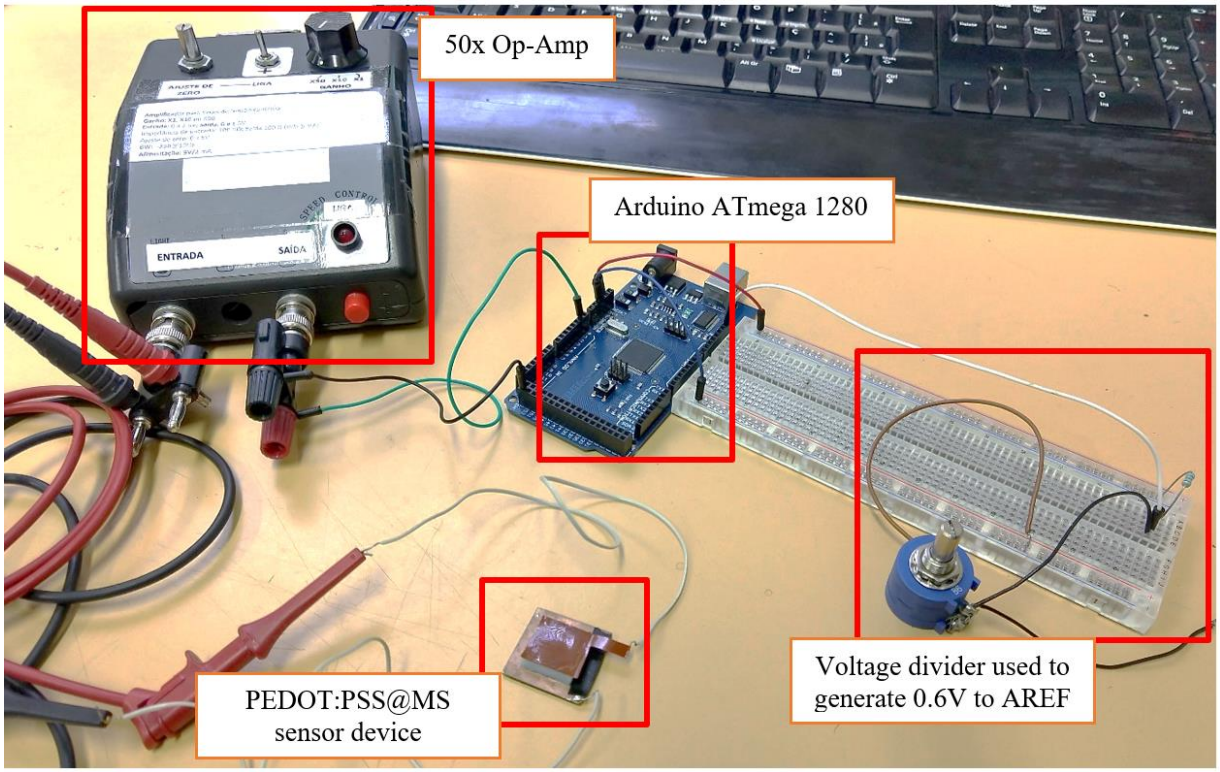

Figure 4.10: (a) High-temperature source for thermally stimulating a fabricated PEDOT:PSS@MS sensor device. Inset: graphical representation of the temperature difference ($\Delta T = T_{top} - T_{down}$) across the device during thermal stimulus; (b) The curve of a V_{therm} response for a fabricated PEDOT:PSS@MS sensor device when under the stimulus of an elevated temperature.

(a) **(b)**

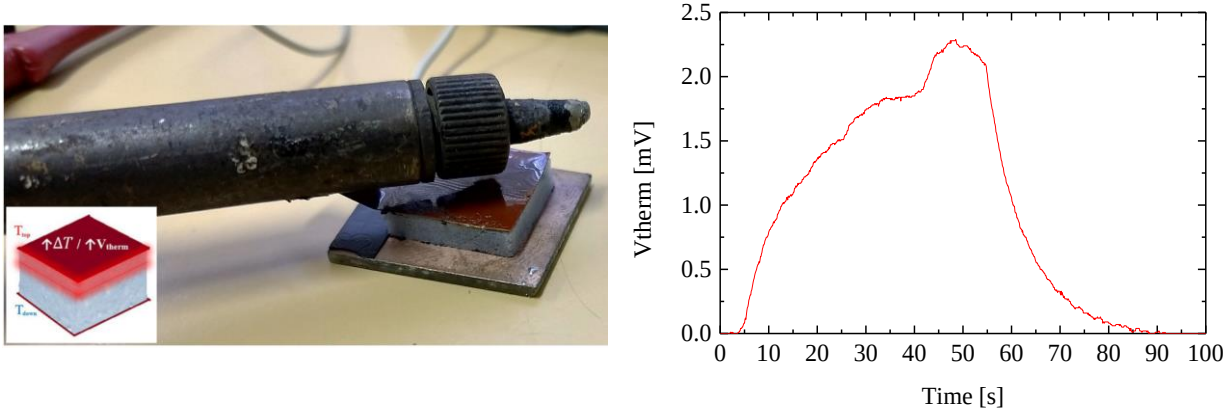

Figure 4.11 displays the curves of the thermal voltage as a temperature gradient response of PEDOT:PSS(diluted)@MS sensor devices with similar internal resistance values, as an attempt to relate the generated thermal voltage to the temperature difference between the terminals of the device, using a pyrometer, in a yet inaccurate method, since it was not sufficiently controlled. Table 4.3 shows the average temperature gradient response for thermal voltages of 0.1, 0.4, and 0.7 mV.

Figure 4.11: Relation between temperature gradient and thermal voltage.

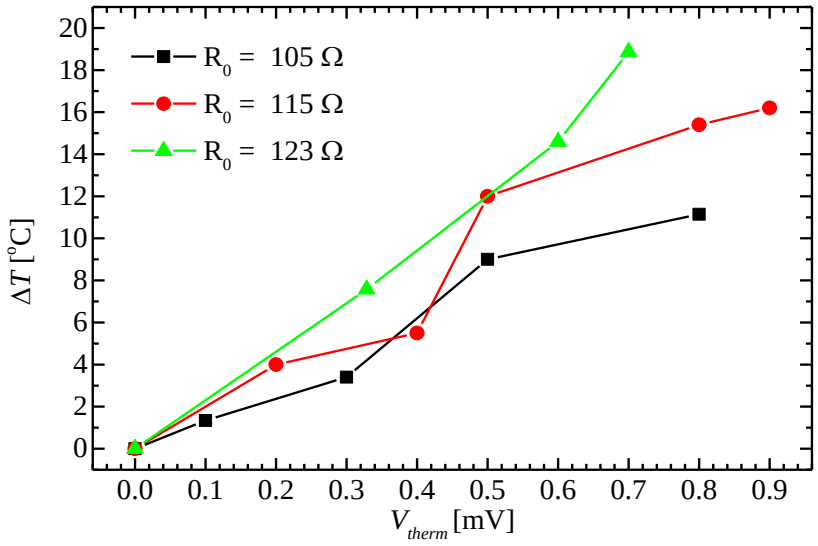

Table 4.3: Average temperature gradient response as a function of thermal voltage.

V_{therm} [mV]	$\overline{\Delta T}$ [ºC]
0.1	1.9 ± 0.5
0.4	7.0 ± 2.0
0.7	14.5 ± 4.2

4.3.3 Evaluating the influence of the sensor thickness

Another parameter of interest for testing was the device thickness and how it would affect the sensor's response to pressure stimuli. Thus, PEDOT:PSS(+5%DMSO)@MS devices with different thicknesses (from 2 to 10 mm) were fabricated for testing (Figure 4.12).

Figure 4.12: PEDOT:PSS(+5%DMSO)@MS sensor devices fabricated with different thicknesses.

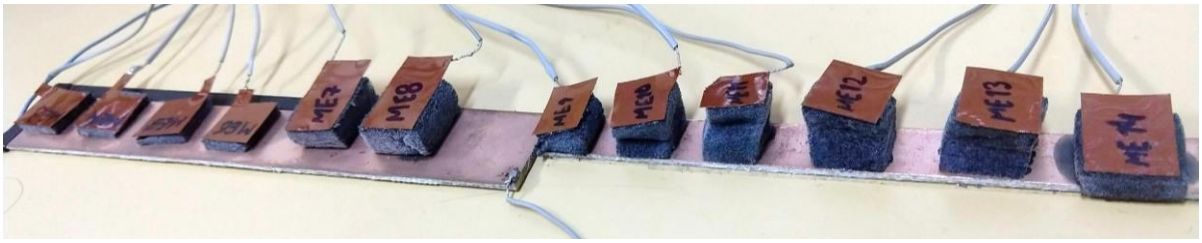

The devices were submitted to the strain test using the micrometer table. They received full compression followed by full release, thus turning back to its pristine state. Figure 4.13(a) shows the curves overtime for the devices with thicknesses of 2, 3, and 5 mm, all having similar internal resistance values close to 11 Ω. Similarly, Figure 4.13(b) shows the curves for devices with 7.5 and 10 mm thicknesses, both having an internal resistance close to 7 Ω. Table 4.4 shows a summary of the average performance of the devices as a function of their thicknesses.

Figure 4.13: Maximum variation of relative resistance as a function of time for sensor devices of different thicknesses and similar internal resistance when under high-pressure load stimulus. (a) Results for thinner devices of approx. 11 Ω; (b) Results for thicker devices of approx. 7 Ω

(a) **(b)**

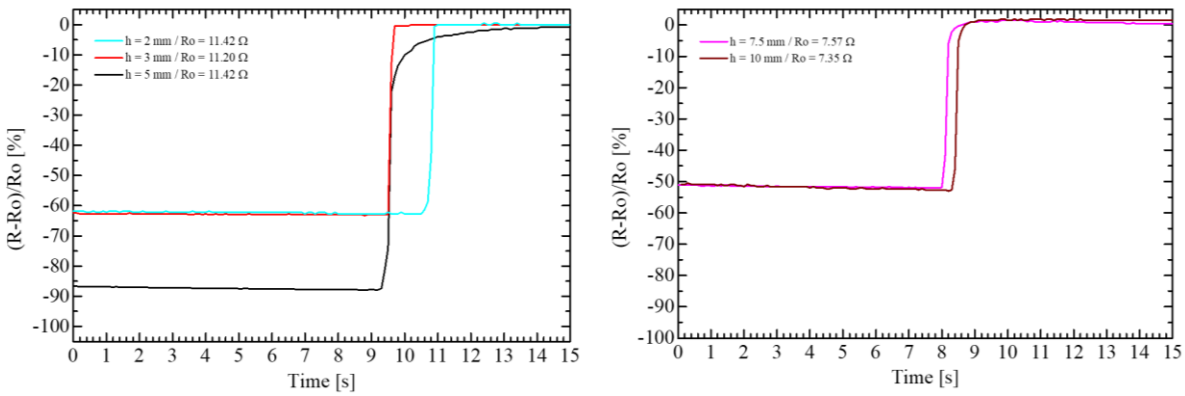

Table 4.4: Average performance as a function of the device's thickness.

$\overline{R_0}$ [Ω]	Thickness [mm]	Max. $\Delta R/R_0$ [%]
~ 11	2	-65
	3	
	5	-85
~ 7	7.5	-50
	10	

The results have shown that, while thicker devices present an absolute relative resistance variation of 50%, the thinner devices present an absolute variation between 65% and 85%. Also,

during testing, it was possible to see that thicker devices presented considerable deformation, thus suffering structure degradation, which is not suitable for repetitive loads of pressure stimulus. Thereby, it is preferable to fabricate thinner devices with thicknesses between 2 and 3 mm.

4.4 Results for Single Devices

In this session, the devices impregnated with different PEDOT:PSS solutions are evaluated. The experiments' goal was to find a correlation between the sensor devices' resistance and their response to pressure and temperature stimuli and understand how it would affect their sensitivity. After finding the devices with dimensions and resistance values that would favor a satisfactory overall performance in all tests, finding a reproducible method for obtaining such devices was necessary.

4.4.1 Evaluating PEDOT:PSS(+5%DMSO)@MS sensor devices

Figure 4.14 shows the pressure and temperature stimuli results obtained for sensors with different R_0's values to understand how the sensor devices' pristine resistance affects their response and performance.

It is essential to notice that the values of the resistance are not well controlled. After removing the foam piece from the solution, it was manually squeezed to remove excess liquid in a merely qualitative process. The lowest value of R_0 refers to the device was not squeezed. The more the excessive solution of PEDOT:PSS(+5%DMSO) is squeezed from the MS, the higher is the internal resistance of the device.

For the stress response results (Figure 4.14(a)), it is possible to see that the device of 23 Ω presented the most significant decrease in resistance, getting close to 60% of the initial value when under stress close to 220 kPa.

For the strain testing results in Figure 4.14(b), the 18 Ω device presented a better response, showing a resistance decrease of 55% when close to maximum strain. As a result (see Figure 4.14(c)), the device of 18 Ω showed higher sensitivity compared to the other two devices with 9.3 Ω and 23 Ω, not sensing more than 140 kPa at a maximum strain.

For the temperature testing (Figure 4.14(d)), the device with 9.3 Ω resistance has produced the highest value of thermal voltage over time, close to 1.6 mV, when under the stimulus of high-temperature.

Figure 4.14: Pressure and temperature stimuli results for PEDOT:PSS(+5% DMSO)@MS devices with different internal pristine resistances R_0. (a) Stress response; (b) Strain response; (c) Stress-Strain curve; (d) Thermal voltage response.

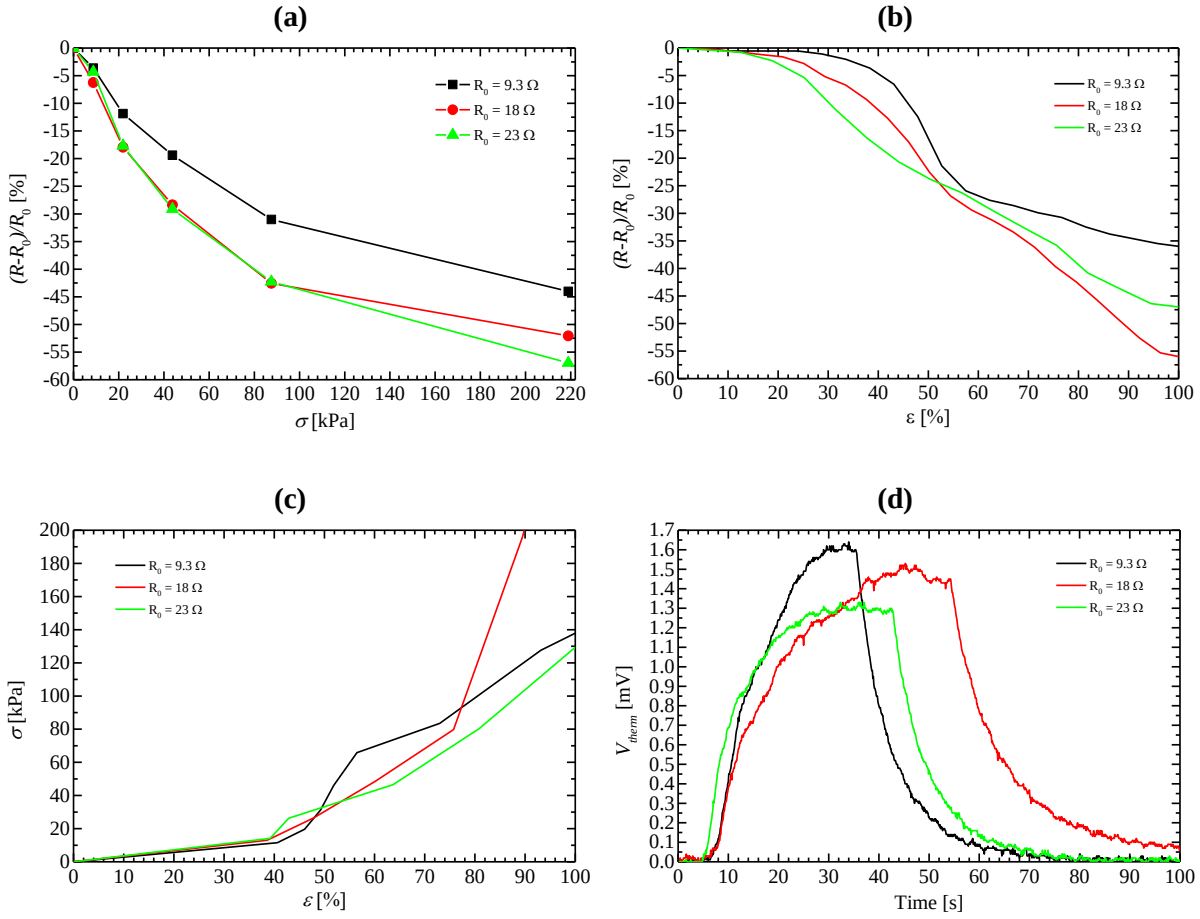

These results have shown that higher resistance PEDOT:PSS(+5%DMSO)@MS devices tend to be more sensitive to pressure stimuli but generate a lower V_{therm} when under temperature. Even with different internal resistance values, all the devices presented similar curves.

4.4.2 Evaluating PEDOT:PSS(original)@MS sensor devices

In the following subsection, the evaluation of more resistive devices is discussed. The preparation procedures for these devices used only the original dispersion of PEDOT:PSS, without adding DMSO.

As mentioned before, the fabrication method for obtaining the device's pristine resistance was still merely qualitative and not well controlled, being defined by the amount of excessive PEDOT:PSS that was manually squeezed from MS. The curves plotted in Figure 4.15 show the performance of PEDOT:PSS(original)@MS sensors when under pressure and temperature stimuli, as done previously for devices with DMSO.

The stress results in Figure 4.15(a) show that the device with the highest pristine resistance showed less sensitivity to stress. While the 375 Ω device had its resistance decreased by 65% under stress close to 220 kPa, the 70 Ω device decreased by 80%. The 17 Ω device (manufactured without squeezing) presented an intermediate result to the other two devices.

For the strain testing, shown in Figure 4.15(b), the device which presented the most significant resistance variation was the one with 375 Ω, which reached a variation of -90% in its internal resistance when under maximum strain. For the devices with 17 Ω and 70 Ω, the resistance values have decreased by 75% and 82% at maximum strain, respectively.

For the resulting stress-strain curves in Figure 4.15(c), the device with the highest internal resistance value has presented a capability of sensing lower pressure values at low strain percentage, being able to detect 4.0 kPa at 10% of strain, while the other devices detected a significant value only close to 30%.

For the temperature stimulus test result presented in Figure 4.15(d), the devices with 70 Ω and 375 Ω produced the highest thermal voltage when exposed to a high-temperature gradient, generating a value close to 2.2 mV, while the 17 Ω device generated a thermal voltage close to 1.6 mV.

Figure 4.15: Pressure and temperature stimuli results for PEDOT:PSS(original)@MS fabricated sensor devices with different internal pristine resistances R_0. (a) Stress response; (b) Strain response; (c) Stress-Strain curve; (d) Thermal voltage response.

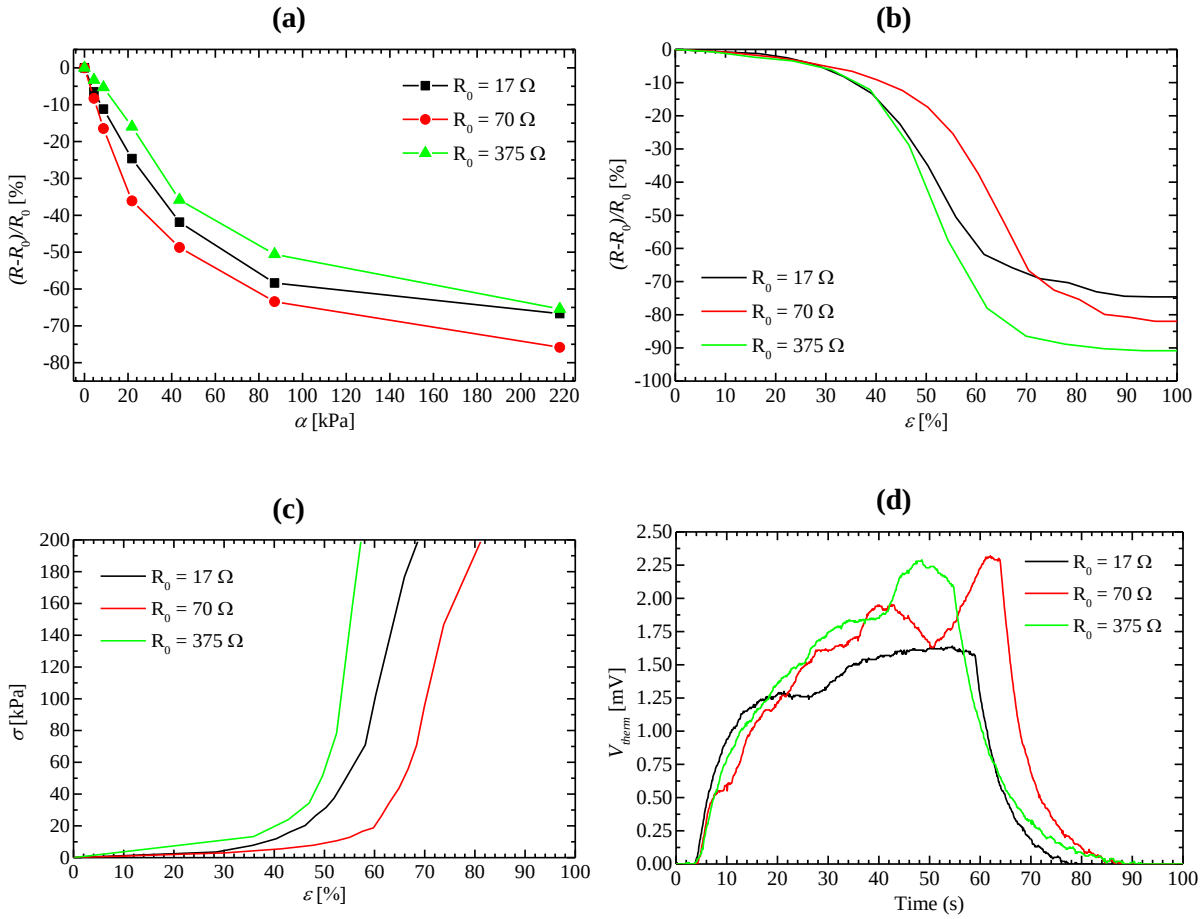

These results suggest that fabricating a device, even without DMSO's addition, presents a satisfactory response to pressure stimulus, and that higher resistances respond better to the temperature gradient. Thus, it is preferable to fabricate devices with internal resistances between 70 and 400 Ω, achieving a reasonable trade-off for performance in pressure and temperature tests.

4.4.3 Evaluating PEDOT:PSS(diluted)@MS sensor devices

The next step was to prepare devices with values of R_0 between 70 and 400 Ω. It was interesting to dismiss the use of DMSO since the high-density structure of the melamine sponge already favors the conductivity of PEDOT:PSS.

It was also essential to find a method to allow the reproducibility of high enough resistance values for the fabricated devices. The chosen method was to dilute the original dispersion of PEDOT:PSS in a larger amount of water to find the best proportion. After some testing, it was possible to find that the addition of 9 parts of H_2O in 1 part of the original dispersion of PEDOT:PSS helped in obtaining devices with a reproducible internal resistance of the order of 100 Ω ($\overline{Ro}$ = 114 ± 9 Ω).

As the results in Figure 4.16 suggest, the overall response to pressure and temperature stimuli for the three devices of remarkably similar resistances was satisfactory. Table 4.5 shows the average values for all three devices' performances to pressure response and the highest thermal voltage generated under temperature stimulus.

The stress test results in Figure 4.16(a) show that even with similar resistances, each device responded differently when under load stimulus, thus presenting an average response of stress with high deviation (see Table 4.5). The device with the lowest resistance value of 105 Ω is the one that presented the most significant resistance variation under pressure stimulus, with a change of -80% close to 220 kPa, like the 115 Ω device. The 123 Ω device presented a lower resistance decrease, reaching 55% at 220 kPa.

The strain test results in Figure 4.16(b) present remarkably similar curves for the three devices. They presented the best performance for this type of test so far, with a low average value of deviation for strain tests (see Table 4.5), reaching a resistance change of -90% when under maximum strain.

While comparing the results of stress with the strain, it is possible to see that, even with remarkably similar internal resistance values, the devices presented different stress curves once the moving micrometer plate device used to perform the strain tests supplies more accuracy and control than the weight loads used to perform the stress tests. Even so, the resulting stress-strain curves in Figure 4.16(c) show that all three devices presented similar sensitivity to pressure stimulus, being able to detect 220 kPa between 50 % and 60 % of strain.

The temperature stimulus test results in Figure 4.16(d) show that the device with the lowest resistance of 105 Ω has generated the lowest value of thermal voltage, close to 2 mV,

while the other two devices of 115 and 123 Ω generated values close to 3.5 mV under high-temperature gradient, which represents the highest generated values for V_{therm} so far (Max. $\overline{V_{therm}}$ = 2.8 ± 0.7 mV).

Figure 4.16: Pressure and temperature stimuli test results for PEDOT:PSS(diluted)@MS fabricated sensor devices with different internal pristine state resistances R_0. (a) Stress response; (b) Strain response; (c) Stress-Strain curve; (d) Thermal voltage response.

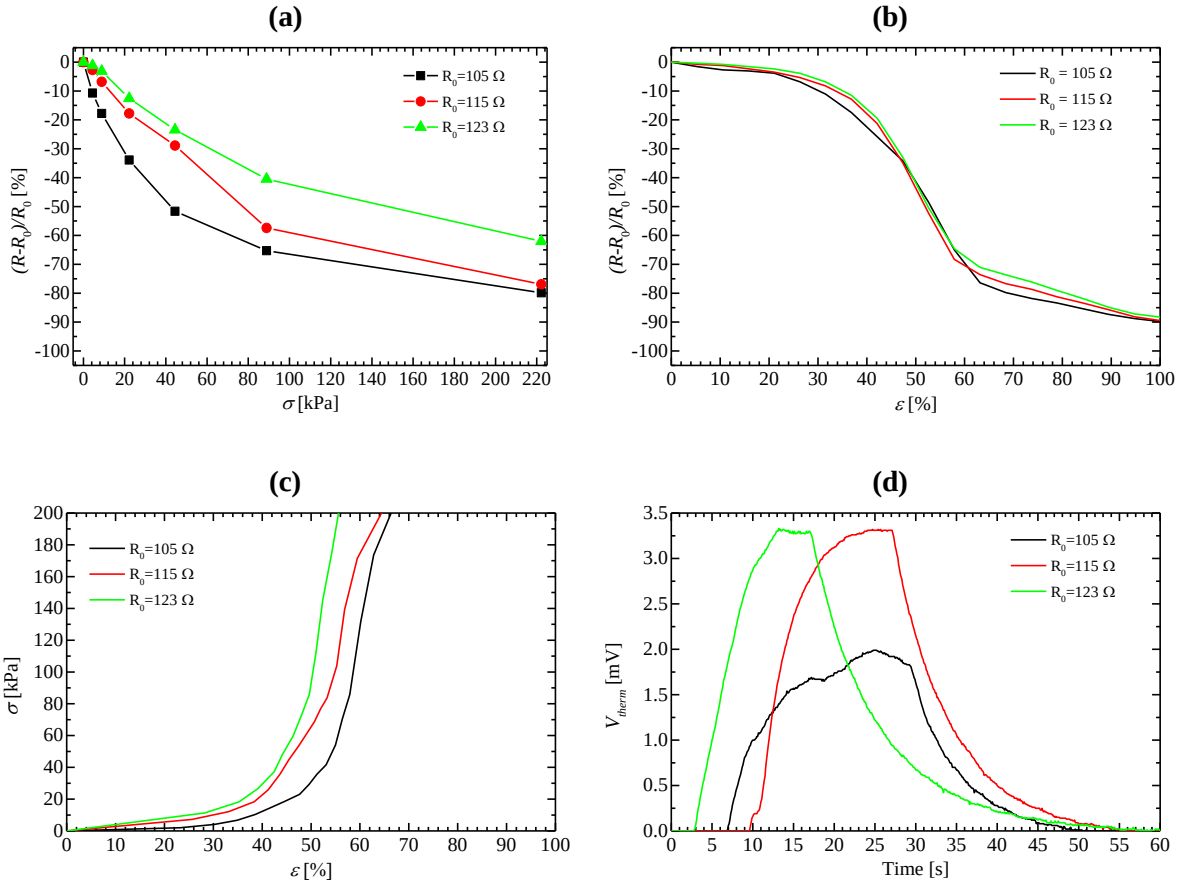

The latest results have shown that even with a highly diluted solution of PEDOT:PSS in water, it is possible to reproduce a sensor device using high-density melamine with a resistance value high enough to have a satisfactory overall performance to both pressure and temperature stimuli.

Table 4.5: Average performance values and deviation for PEDOT: PSS(diluted)@MS sensor devices, showing the average pristine resistance ($\overline{R_0}$) of the fabricated devices, and the average values of stress

($\bar{\sigma}$) and strain ($\bar{\varepsilon}$) for different values of resistance variation (|ΔR/R0|), and the maximum average value of generated thermal voltage ($\overline{V_{therm}}$).

$\overline{R_0}$	$\lvert\Delta R/R_0\rvert$ [%]	$\bar{\sigma}$ [kPa]	$\bar{\varepsilon}$ [%]	Max. $\overline{V_{therm}}$
114 ± 9 Ω	10	12.2 ± 7.2	33.0 ± 2.6	2.8 ± 0.7 mV
	20	24.9 ± 13.6	40.8 ± 2.3	
	30	41.6 ± 21.6	45.5 ± 0.7	
	40	52.6 ± 31.2	49.2 ± 0.3	
	50	89.2 ± 53.8	52.5 ± 0.6	
	60	125.8 ± 76.6	55.9 ± 0.7	

The dilution of 9 parts of H_2O did not compromise the detection properties of the devices. Table 4.6 summarizes all single devices' performance and shows that the 123 Ω device has the highest sensitivity to pressure and temperature stimuli. This device detected 4.0 kPa at 10% of strain and 200 kPa at 55% of strain. Also, the device was able to generate a thermal voltage of 3.2 mV under the high-temperature stimulus. The next session presents a multiple 4x4 matrix device as a bidimensional sensor with an optimized fabrication process, considering Table 4.6.

Table 4.6: Summary of the characterization of the PEDOT:PSS@MS sensor devices.

	R_0 [Ω]	Max. $\Delta R/R_0$ [%]	σ [kPa]				Max. V_{therm} [mV]
			@ 10 % ε	@ 45% ε	@ 50% ε	@ 55% ε	
+ 5% DMSO	9.3	-35	3.3	18.7	36.1	62.4	1.6
	18	-55	3.3	23.1	30.3	40.7	1.5
	23	-47	3.3	29.2	33.2	38.9	1.3
Original	17	-75	0.9	18.7	30.2	56.7	1.6
	70	-80	0.9	6.5	8.5	13.4	1.8
	375	-90	4.3	30.8	54.6	157.0	2.7
Diluted in H_2O	105	-90	0.5	20.1	30.6	60.5	2.0
	115		3.1	46.2	65.4	110.6	3.2
	123		4.0	55.8	94.9	200	3.2

4.5 PEDOT:PSS@MS-based 4x4 sensory array

After testing and optimizing single devices and finding the best geometry and resistance values to obtain the most appropriate responses, it was possible to manufacture an array of 4x4 pressure sensors. The use of a melamine sponge and a diluted solution of PEDOT:PSS for the fabrication of the sensor provided an increase in the resistance value and the possibility for good signal conditioning.

The device's fabrication required a single squared piece of sponge with 2.5 x 2.5 cm^2 area and 2.5 mm thickness. A flexible sheet of *copper laminate polyamide* was used as the top electrode, commonly connected to the entire matrix, to grant touch flexibility. A non-flexible copper circuit board served for the manufacturing of 16 electrodes on the bottom of the device. Table 4.7 presents a list of the manufacturing details of the matrix.

Table 4.7: Fabrication aspects for the PEDOT:PSS-based sensory array.

PEDOT:PSS solution	Diluted in 9 parts of H_20
Foam	High-density melamine sponge
Thickness	2.5 mm
Area	6.25 cm^2
Dip-coating	30 min
Drying	2 h @ 100 ºC
Top electrode	A flexible sheet of *copper laminate polyamide* (0.1 mm thick) A single piece of 6.25 cm^2
Bottom electrode	A rigid plate of copper (PCB fiberglass board) (Photolithography - 4x4 matrix) 16 electrodes of 16 mm^2 each

The manufacturing of this device aimed to interface an array based on PEDOT: PSS@MS with the Arduino board and software developed in *Processing*, which allows users to have visual feedback of a virtual matrix on the computer screen, providing real-time monitoring of the position, percentage of resistance variation, and intensity (in grayscale) applied to the sensor matrix device.

4.5.1 Signal Conditioning and Circuit

The signal conditioning for the 4x4 matrix and the system used for data acquisition work similarly to that for single devices' resistance variation measurements (see Section 4.2.1). The device works as a matrix of 16 voltage dividers, according to the schematic in Figure 4.17. With this approach, it was necessary to use 16 Arduino's analog inputs (A0 to A15) and 16 reference resistors, connected between the V_{DD} of 5 V Arduino's built-in power supply (red wire) and each of the 16 device's bottom electrodes. The top of the device has only one electrode, commonly grounded (blue wire).

Figure 4.17: The schematic of the PEDOT:PSS@MS-based 4x4 array.

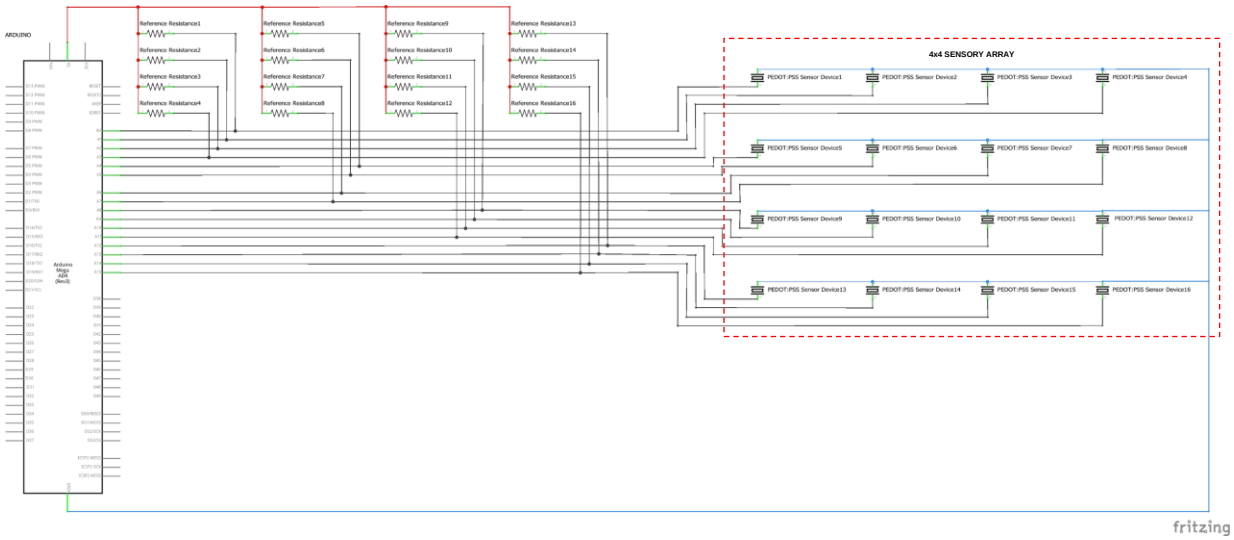

4.5.2 Electrodes Fabrication Process and Device Assembling

The sensor device's bottom electrodes were fabricated on a hard copper plate using the photolithography technique, which required a photomask production with the desired design. The device fabrication took place in a clean room, with temperature, humidity, and particle control.

4.5.2.1 Mask fabrication for the bottom Electrodes

The fabrication of a photomask, designed with the *Layout Editor Software*, was performed using the *Heidelberg µpG 101 Tabletop Micropattern Generator* (Figure 4.18). A stack of glass/chromium/photoresist served as the substrate for the patterning. The mask's production required adjusting a significant quantity of parameters within the micropattern generator, such as the laser's focus and energy, which required adjustments for diverse types and thicknesses of photoresist.

Figure 4.18: Heidelberg µpG 101 Tabletop Micropattern Generator.

Figure 4.19(a) shows the design used to draw the array of electrodes. It was necessary to develop the exposed photoresist and perform the chromium etching using a cerium sulfate solution. Figure 4.19(b) shows the manufactured photomask ready to use. The large electrode pads have 4x4 mm^2 and are 2 mm distant from each other. Each of the small pads used to weld the wires for the acquisition system's connections has 1.5x1.5 mm^2. The paths are 200 µm wide.

Figure 4.19: (a) Design used to print the photomask; (b) The fabricated photomask ready to use.

(a) **(b)**

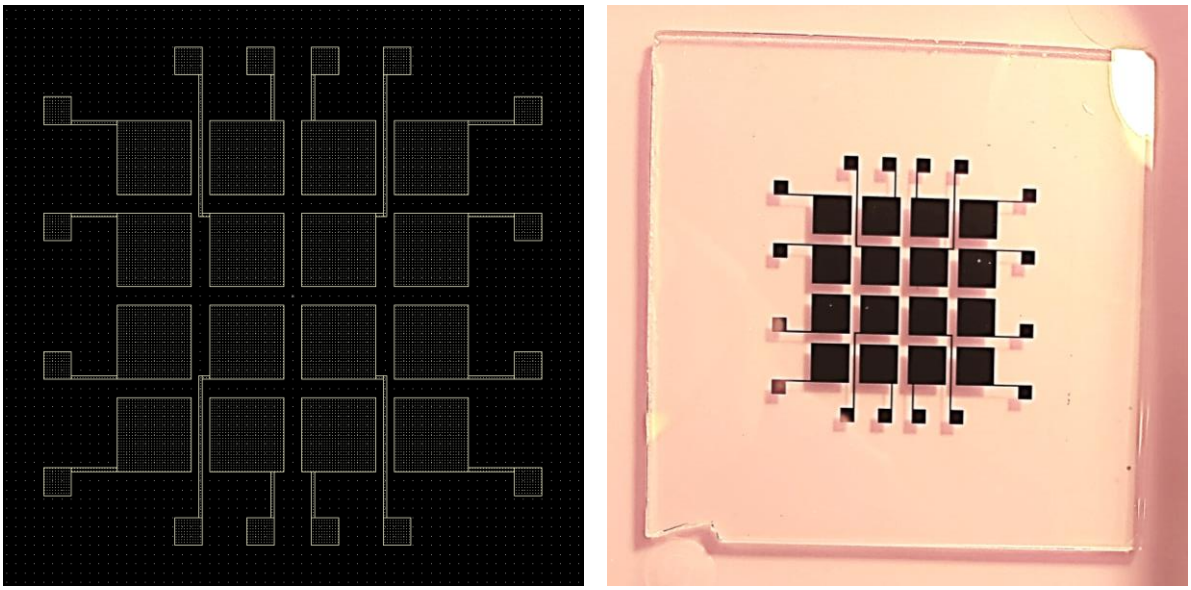

4.5.2.2 Photolithography of the bottom Electrodes

The photolithography process consists of the micropatterning of complex structures on photoresist, subsequently transferring the conductive substrate, in this case, a rigid copper plate. The recipe in Table 4.8 is used for most photolithography steps and requires a hot plate, regular spinners, and an exposure lamp.

Once the spin-coating of photoresist on the copper plate was concluded, UV light exposure was performed. During this process, the photomask, placed on the copper plate, "protected" the region chosen to receive the electrodes' design. After exposure, the photoresist's development process revealed the electrodes' desired design on the copper plate's surface.

Table 4.8: Recipe used for photolithography.

Photoresist	AZ1512
Spin coating	4000 RPM for 50 sec.
Soft Baking	90~100◦C for 5 min.
Exposure time	120 sec.
Development	60 seconds at 5 H_2O(DI):1 AZ351
Wash	H_2O (DI) for 5 minutes
Hard Baking	100~110◦C for 5 minutes

After the photolithography process, the plate received an iron perchloride etching. During this process, the entire region of “unprotected” copper was removed from the plate,

preserving only the region protected by the photoresist (subsequently removed in acetone). Figure 4.20 is a picture of the manufactured copper electrodes, ready to be assembled into the PEDOT:PSS@MS-based 4x4 sensory array.

Figure 4.20: Picture of the copper matrix of electrodes made via photolithography, after etching.

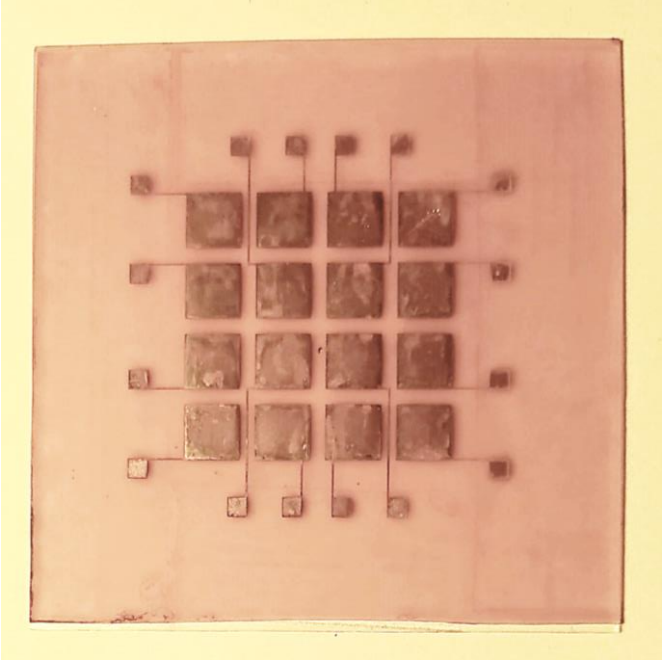

4.5.2.3 Device Assembling

To assemble the device into the desired sensory array, the piece of melamine sponge impregnated with PEDOT:PSS(diluted) was carefully attached (using conductive glue) to each of the individual 16 electrodes of the matrix on the rigid plate. A single flexible copper laminate polyamide sheet is attached and connected to the VDD source on top of the device. Each electrode received the proper wiring (Figure 4.21(a)), using the small pads for soldering. The device received the connection to the acquisition system setup used for testing, as displayed in Figure 4.21(b).

Figure 4.21: (a) PEDOT:PSS(diluted)@MS-based 4x4 sensory array; (b) The system used to perform tests on the device, using the Arduino microcontroller.

(a)

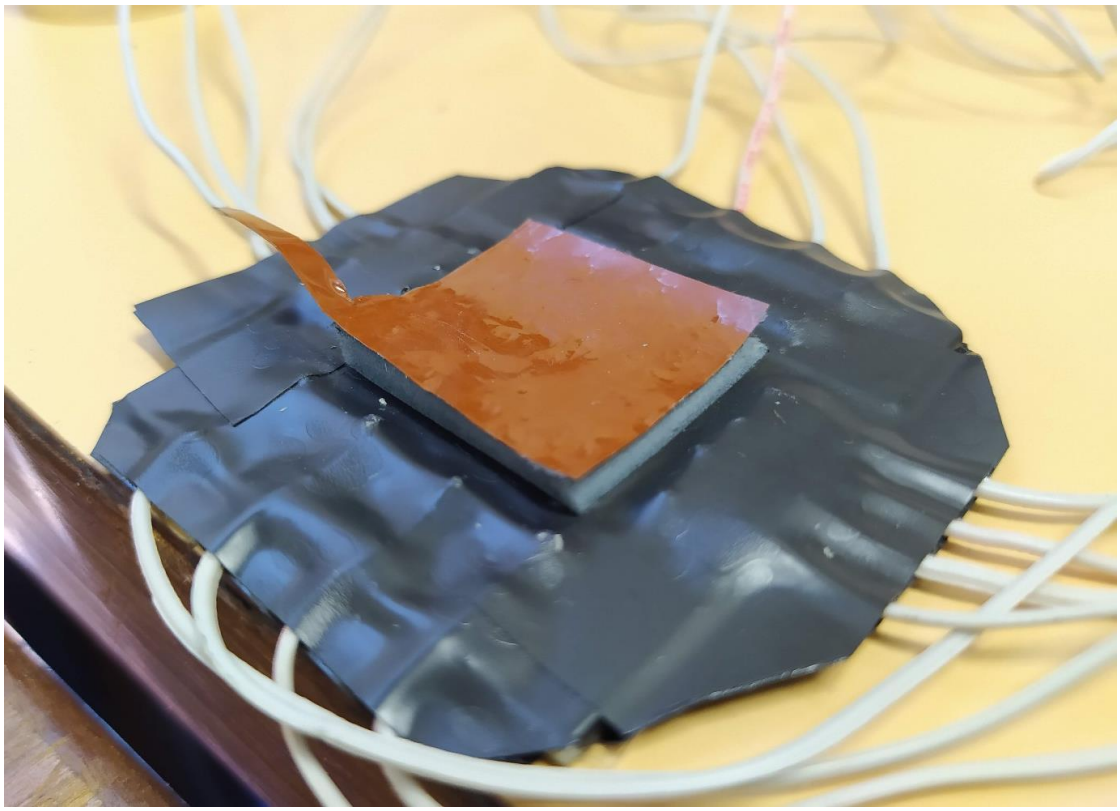

(b)

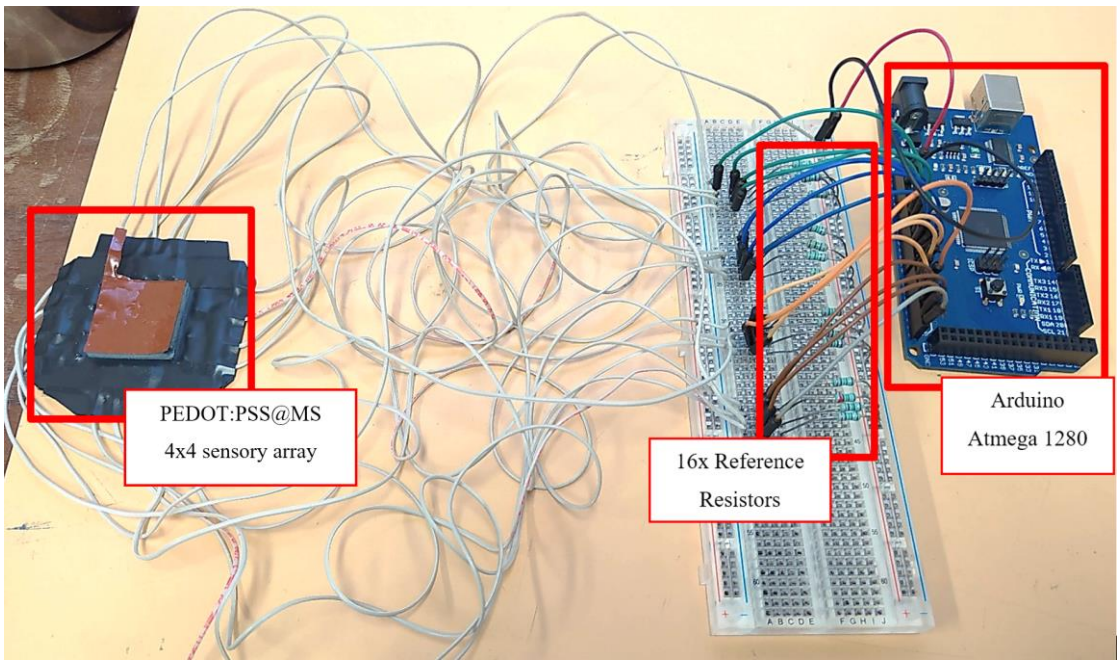

4.5.3 Matrix sensor software and testing

The Arduino *Standard Firmata* library and software programmed in *Processing* helped obtain a graphical interface for real-time monitoring of the sensor. In this software, a virtual matrix allowed the visualization of both the pressed position and the intensity (represented in grayscale) applied by the user in a specific region of the real device. The software used the resistance values read on the Arduino's analog ports (from A0 to A15) to fill the 4x4 sensory matrix's graphic representation with all its 16 positions, represented as “pixels.”

4.5.3.1 Hardware-software communication

Standard Firmata is a software library that allows Arduino boards to communicate with computers, while *Firmata* is the communication protocol between microcontrollers and software on computers, smartphones, or tablets.

Uploading the *Standard Firmata* library (already installed in the Arduino IDE) to the board is necessary when the user wishes to leave it connected to the computer for data transferring. In this case, the board acts as an "extension" of the user's computer to provide a set of inputs and outputs for digital and analog connections.

Processing is a software package that uses *Standard Firmata*, allowing communication between the board and the computer. After the user uploads *Standard Firma* to the Arduino board, the desired script's encoding takes place entirely within *Processing* (see Appendix 6.3).

4.5.3.2 Grayscale device calibration

A digital grayscale image represents the value of each pixel in a range between black and white. Gray scales vary between black as the lowest intensity and white as the highest intensity. Monochrome images typically have 8 bits per pixel of storage, which allows 256 intensities.

Considering this, once the communication between the device and the software was made, it was necessary to conduct a sensor calibration so that the grayscale would respond correctly to each matrix pixel's sensitivity.

To do so, a load of 5 kg served as a reference (Figure 4.22(a)), corresponding to a pressure of 78.45 kPa. This initial calibration defined the minimum resistance values R_{min} obtained for each of the 16 pixels in the matrix.

After removing the reference load from the top of the device, the values obtained for the sensor matrix pristine state were stored, corresponding to the resistance values R_0 for each of the 16 pixels in the matrix, when it was not under the influence of any pressure load (Figure 4.22(b)).

Figure 4.22: (a) The device under the calibration process with the 5 kg reference load; (b) The device in its pristine state after calibration. The snapshot shows the matrix software at initialization after calibration.

(a) **(b)**

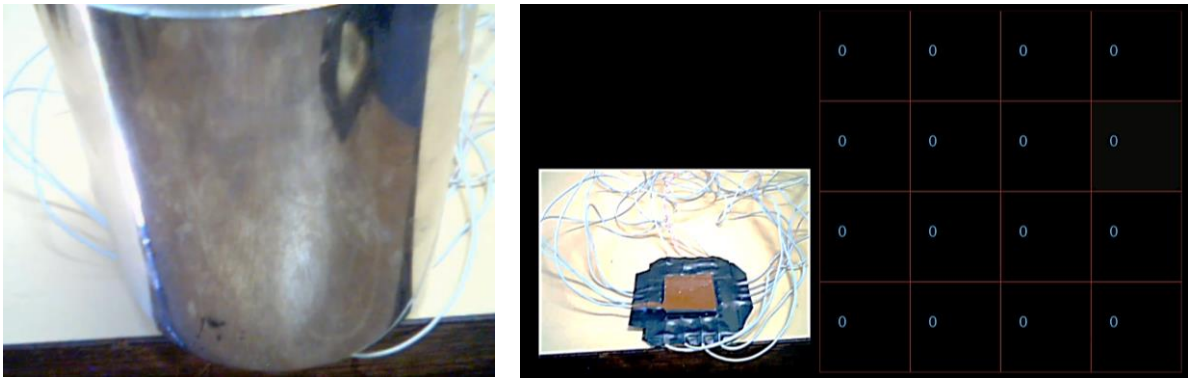

The programming on the *Processing* software was responsible for storing and relating the resistance values measured during the calibration to the grayscale's maximum resolution, from 0 to 255. Therefore, the closer to R_0 the measured value of resistance was, the *darker* the feedback (intensity 0), showing that the sensor did not suffer significant pressure. The closer to R_{min} the measured value of resistance was, the *lighter* was the feedback (intensity 255), which means that the sensor suffered a significant pressure stimulus.

The following formula was programmed into the *Processing* software and is responsible for normalizing the grayscale value for each sensor pixel in the matrix:

$$RV[i] = 255 \times \left[1 - \left(\frac{R[i] - R_{min}[i]}{R_0[i] - R_{min}\ [i]}\right)\right] \quad (23)$$

R[i] is the resistance value measured in real-time for a sensor pixel on position *i* of the matrix. For instance:

- If $R[i] = R_0[i]$, then $RV[i] = 0$ (black);
- If $R[i] = R_{min}[i]$, then $RV[i] = 255$ (white).

The software also shows the absolute value of resistance variation percentage for each pixel in the sensor matrix. Figure 4.23 shows how the resistance values relate to grayscale in the software.

Figure 4.23: The 8-bit grayscale spectrum calibration related to the internal resistance of the device.

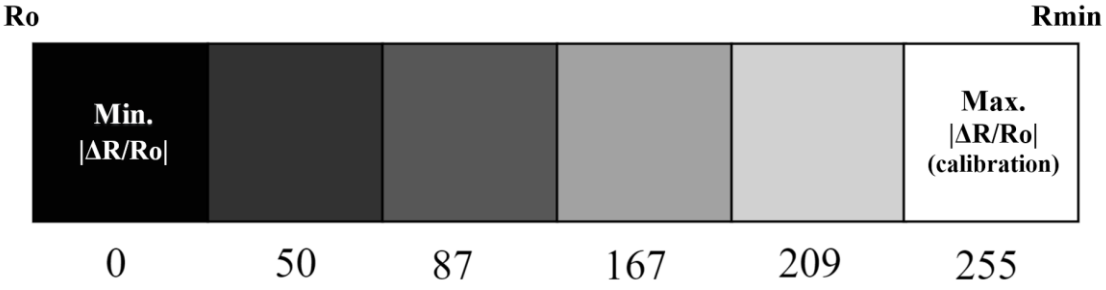

Modified from (COLOR \ PROCESSING.ORG, *[s. d.]*)

Table 4.9 shows the R_{min} and R_0 values obtained during the calibration of the PEDOT:PSS(diluted)@MS-based 4x4 sensory matrix. The average value of the device's resistance in its pristine state was of the order of 1 kΩ, higher than that obtained for similar single devices.

Each pixel of the matrix presented a different value of R_0, with a deviation of ± 352.4 Ω. That happened due to differences in contact between the electrodes and the sponge. During calibration, it was possible to measure a smaller deviation of ± 128.8 Ω, since the pressure applied to the device helped improve the electrodes' contacts.

Table 4.9: Values for the internal resistance of calibration (R_{min}) and pristine state (R_0) for the PEDOT:PSS(diluted)@MS-based 4x4 sensory array.

R_{min} [Ω]				R_0 [Ω]			
1104.7	664.1	595.2	519.7	1621.2	1000	931.2	845.6
724.4	636.6	541.6	359.9	1261.9	1672.7	841.7	658.3
578.3	456.2	583.3	398.2	986.9	768.7	1672.7	750
474.1	349.6	412.7	477	857.5	629.8	761.1	931.2
$\overline{R_{min}} = 554.7 \pm 128.8\ \Omega$				$\overline{R_0} = 1011.9 \pm 352.4\ \Omega$			

It was possible to attenuate the deviation between the matrix's pixels with the normalization of relative resistance variation (Table 4.10). In this case, the device calibration reached a maximum average resistance variation of 44%, with a ± 9% deviation. This result suggests that, even though each pixel has a different internal resistance value, the matrix tends to respond similarly to the pressure stimulus, with the proviso that some pixels tend to be more sensitive than others.

Table 4.10: Maximum value of $|\Delta R/R_0|$ reached during the calibration of the PEDOT:PSS(diluted)@MS-based 4x4 sensory array.

Max. $\lvert\Delta R/R_0\rvert$ [%]			
32	34	36	38
43	62	36	45
41	41	65	47
45	44	46	49
$Max.\overline{\left\lvert\frac{\Delta R}{R_0}\right\rvert} = 44 \pm 9\ \%$			

4.5.3.3 Device response test

Figure 4.24 shows a snapshot of the virtual 4x4 matrix sensor software, with a photo of the actual manufactured device, being assessed simultaneously. The software displays the real-time visual intensity feedback (in grayscale) and the absolute percentage of resistance variation (blue numbers) for the position (white numbers) of the 4x4 sensory matrix.

In this test, position 13 of the matrix received a certain amount of pressure, which generated a relative resistance variation of 43%. The pixel in this position has become lighter than the others, according to the grayscale used. It was possible to observe that the neighboring pixels also suffered variation in their resistance, something expected for a device manufactured with a single piece of sponge and a commonly connected top electrode.

Figure 4.24: Snapshot from a recording showing the sensor device under test. The software displays feedback in shades of gray, showing the specific position and the absolute percentage of the percentage resistance variation caused by pressure.

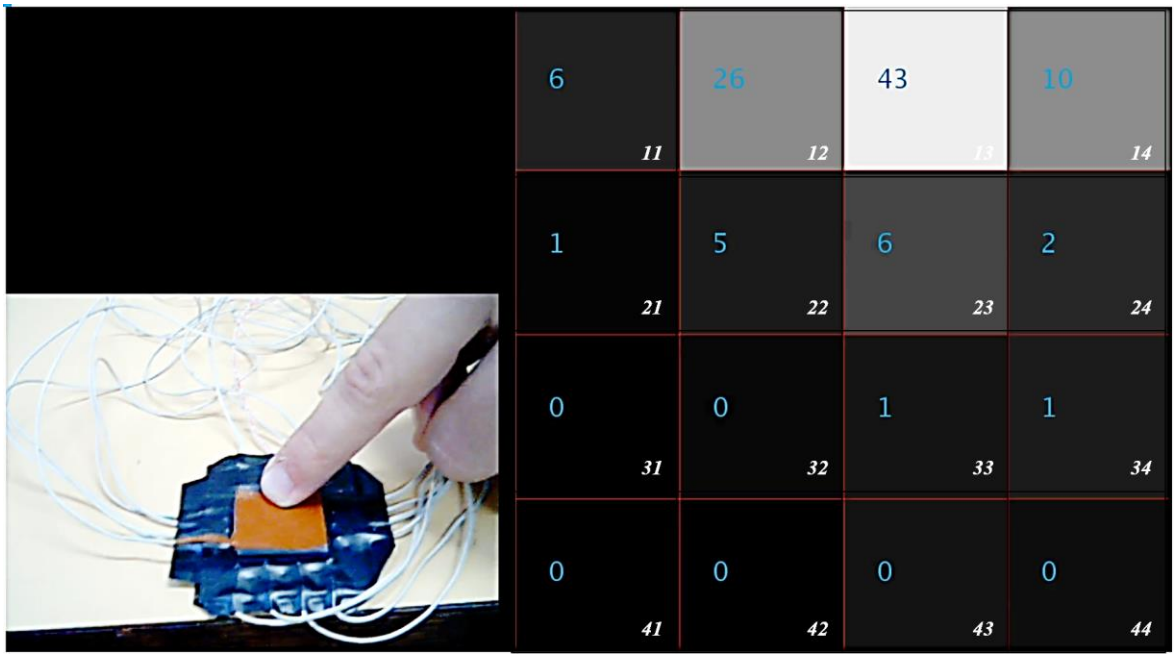

Figure 4.25(a-d) shows the corners of the device under test. It was possible to accurately monitor the position under testing, seeing that the region under pressure became more apparent than the others. Figure 4.25(e-f) shows the device under the pressure of loads of 5 and 2 kg, respectively. The pixels showed satisfactory overall performance, although with different sensitivities. A video from this test is available on a link in Appendix 6.5 (Test 1).

Figure 4.25: Testing the PEDOT:PSS(diluted)@MS-based 4x4 sensory array. Testing of positions (a) 11, (b) 14, (c) 41, and (d) 44. Testing with loads of (g) 5kg and (h) 2 kg.

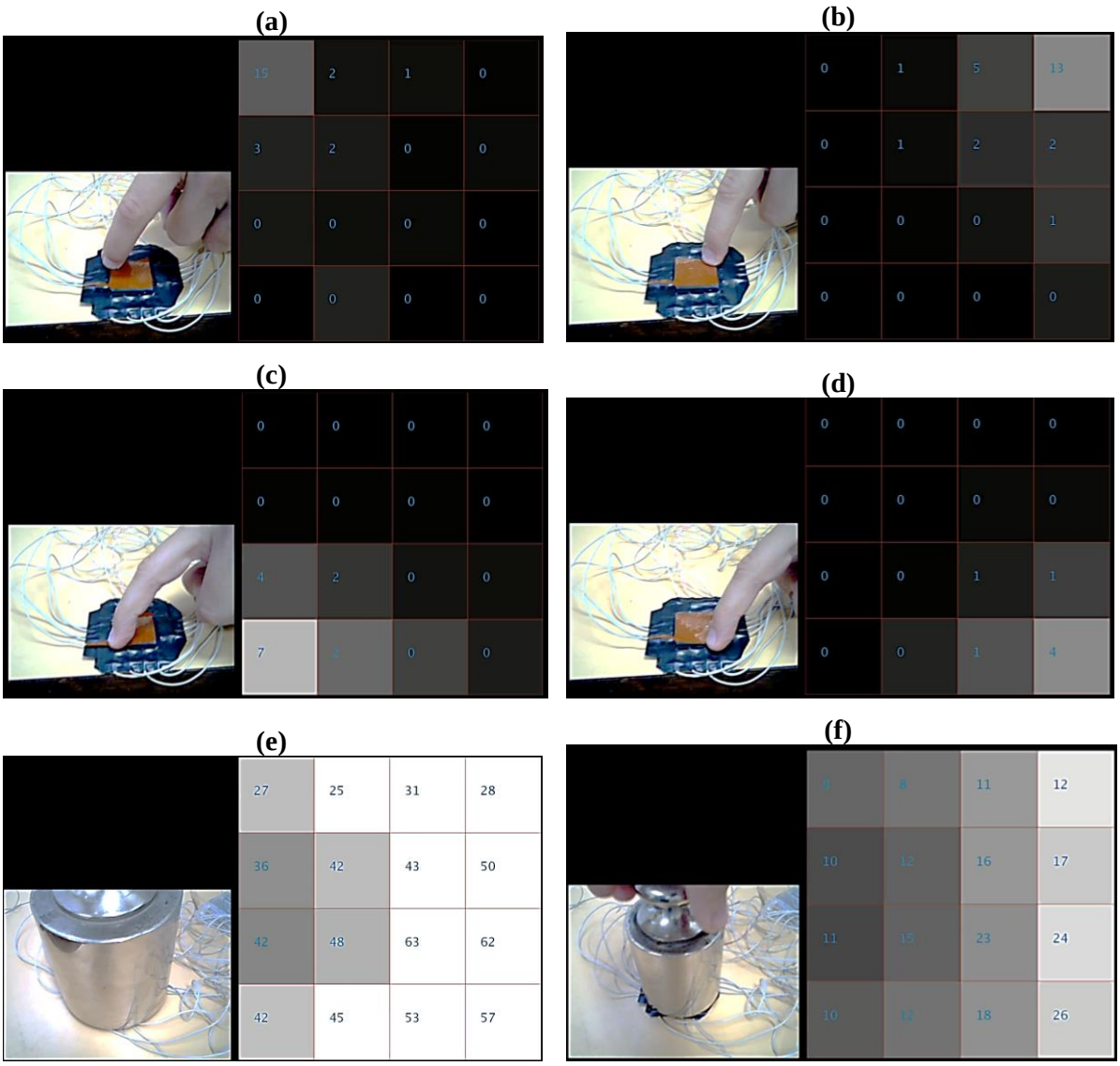

Figure 4.26 shows photos of a complete test of each of the 16 pixels of the device. The matrix had a satisfactory response once it was possible to monitor each pixel's value individually. A video from this test is available on a link in Appendix 6.5 (Test 2)

Figure 4.26: Full demonstration of the performance of the PEDOT:PSS(diluted)@MS-based 4x4 sensory array. Position in the matrix: (a) 11, (b) 12, (c) 13, (d) 14, (e) 21, (f) 22, (g) 23, (h) 24, (i) 31, (j) 32, (k) 33, (l) 34, (m) 41, (n) 42, (o) 43, and (p) 44.

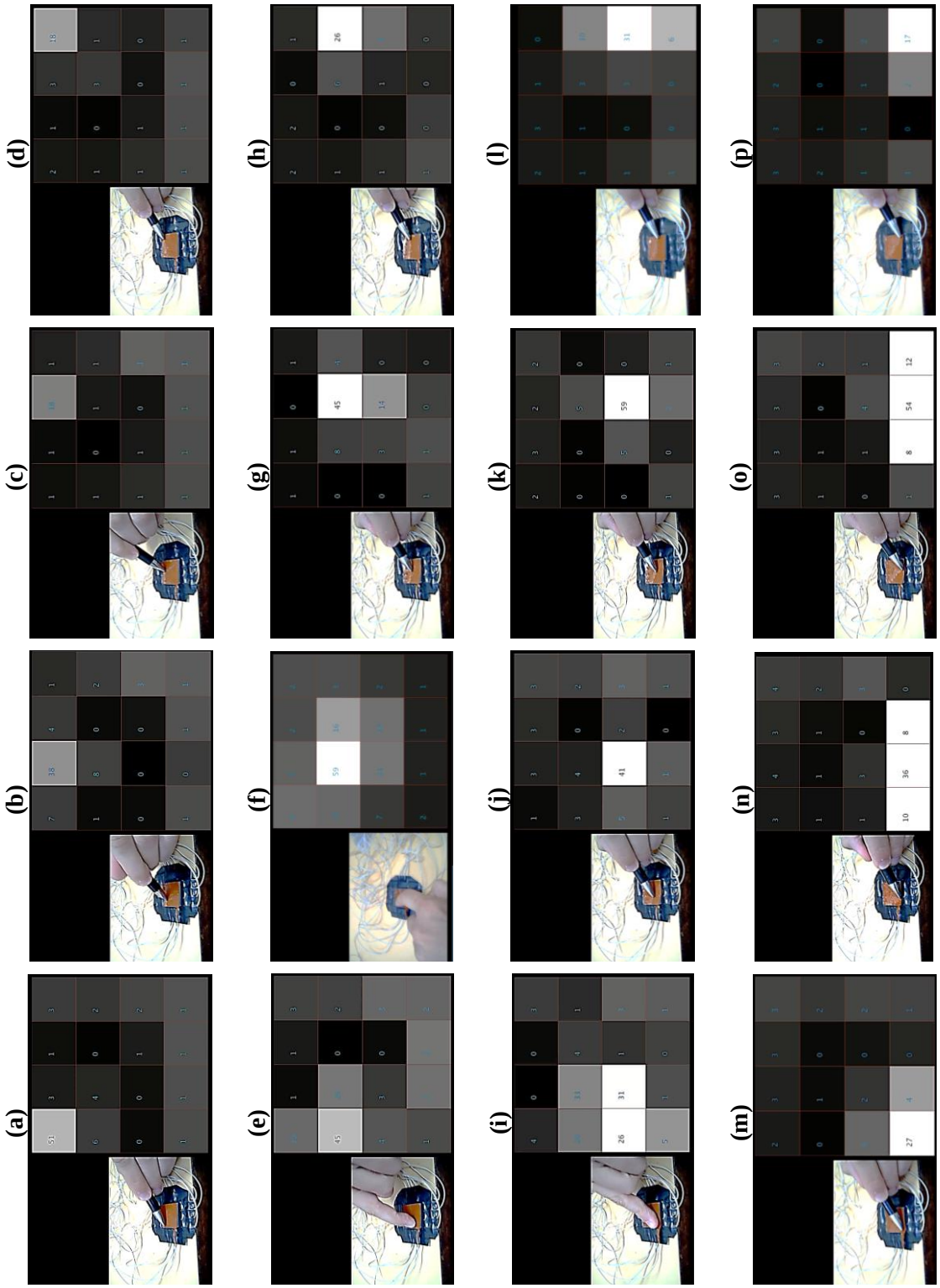

As expected, the pressed pixels became lighter, and their percentage of resistance variation increased. However, it was possible to observe that the device's repetitive use tended to de-calibrate it over time, which caused some pixels to exhibit unexpected behaviors, which became noticeably clear even without pressing. Even though it was possible to solve this problem within each new calibration, the device contacts were degrading with intensive use, making signal reading sometimes unstable. This fact indicates the need for improvements in the preparation of the device and electrode contacts.

5. CONCLUSIONS

This work has deepened the study, fabrication, and characterization of pressure-temperature sensing devices based on foams impregnated with PEDOT:PSS. It was possible to manufacture devices from flexible microstructured materials, such as polyurethane foams (PU) and commercial melamine sponges (MS), which provided good flexibility and mechanical resistance to pressure stimuli. Using a well-known organic thermoelectric semiconductor material, such as PEDOT:PSS, gave the sponges the necessary properties for building pressure and temperature sensors. Achieving this was possible with the simple dip-coating impregnation of these porous structures on a solution of PEDOT:PSS and the sample fabrication was refined through the project.

The data acquisition system developed for the tests was built with an Arduino microcontroller, enabling to measure the real-time resistance and voltage variations with satisfactory resolution and precision. It was possible to program the microcontroller to perform a real-time reading of the manufactured sensor devices' internal resistance variation, as a voltage divider circuit. In preliminary tests, it was possible to validate the efficiency of devices manufactured in polyurethane and melamine, showing a straightforward implementation of technology. These initial devices achieved an internal resistance variation of the order of 40% under mechanical pressure stimulation.

During the preliminary temperature tests, it was possible to perceive certain instability of the signal since it was in the order of millivolts. This instability, resulting from the material's high sensitivity to changes in the environment, such as temperature and humidity, could be corrected using an external voltage reference of 0.6 V, allowing a better resolution of the signal, stabilizing the reading, and making it less noisy. Besides, the use of a 50x voltage amplifier provided better signal reading.

When assessing foams of different thicknesses, it was observed that thicker devices did not perform better, once their structure suffered more significant degradation and deformation than the thinner devices when under high mechanical stress. Thus, it was possible to conclude that the fabrication of devices with thicknesses not exceeding 5 mm is preferable.

Upon testing devices with different values of resistance, it was possible to observe that the less resistive devices, with the addition DMSO (with resistances between 9 and 25 Ω), were the ones that presented less variation of internal resistance under high pressure (between 35 and 47%) and thermal voltage generation under elevated temperature (between 1.3 and 1.6 mV).

Thus, it was possible to conclude that the addition of 5% vol. DMSO to increase conductivity PEDOT:PSS, as suggested in the literature, could be dismissed on these devices. The use of the original dispersion of PEDOT:PSS proved to be sufficient for melamine sponges and generated more resistive devices (with resistances between 70 and 300 Ω).

In light of that, it was possible to conclude that the dilution of a solution of PEDOT:PSS in 9 parts in H_2O resulted in devices with a reproducible resistance value in the order of 100 Ω. PEDOT:PSS(diluted)@MS devices showed a satisfactory response in both pressure and temperature stimulus tests. These devices' average performance in strain tests was up to 90% of maximum variation in relative resistance, with low standard deviation, which was the best among all the other devices evaluated. These devices showed good sensitivity, detecting from 3 to 30 kPa (equivalent to values between 10 and 50% of strain, respectively). The maximum thermal voltage generated by these devices was, on average, 2.8 mV, one of the highest among all manufactured devices.

A 4x4 matrix was manufactured, considering the performance obtained in individual sensors, using a novel approach, not yet reported in the literature: the use of a single piece of melamine impregnated in diluted PEDOT:PSS for the construction of the device, with individual bottom electrodes and a single upper flexible electrode. It was possible to integrate the sensor in the Arduino microcontroller and in an interface programmed in *Processing* with a virtual matrix design in which the position and pressure intensity were visualized in real-time.

However, there is still room for future improvements. The foam cutting methodology, for example, can be improved in a way to allow the user to make more precise cuts and choose an exact value of the desired dimensions.

Another opportunity would be to develop a method that offers better control for stress tests. The method used for stress tests requires the user to manually place a weight load on the device, which was difficult to control since it was crucial to perform an even distribution of the load.

As for temperature stimulus tests, it would be interesting to look for a more quantitative method. To reach this objective, it may be useful to develop a temperature-controlled system that allows the user to monitor the sensor device's top and bottom temperatures in real-time when under a gradient influence. Thus, it would be possible to discover the relationship between V_{therm} and temperature precisely.

Finally, the 4x4 matrix sensor device showed promising results, with the need to improve the contacts between the electrodes and the sponge, since they presented degradation with intensive use. Another 8x8 sensor matrix project was developed (see Appendices 6.6, 6.7, and 6.8). However, more tests are needed to validate its functionality.

6. APPENDICES

6.1 PEDOT:PSS Product Specification (CAS 155090-83-8)

SIGMA-ALDRICH®

sigma-aldrich.com

3050 Spruce Street, Saint Louis, MO 63103, USA
Website: www.sigmaaldrich.com
Email USA: techserv@sial.com
Outside USA: eurtechserv@sial.com

Product Specification

Product Name:
Poly(3,4-ethylenedioxythiophene)-poly(styrenesulfonate) - high-conductivity grade

Product Number: **900181**

TEST	Specification
Appearance (Color)	Dark Blue to Very Dark Blue
Appearance (Form)	Liquid or Suspension
pH	2.0 - 3.5
Surface Resistance (ohm/sq) (coating: 40u wet - drying: 6 min 130°C)	< 200
Viscosity mPa.s at 20°C	< 70
Transmission Visual Light	≥ 80 %
Trademark Orgacon is a trademark of Agfa-Gevaert N.V.	Confirmed
Recommended Retest Period 1 Year	----------

Specification: PRD.2.ZQ5.10000076780

6.2 Arduino script to measure real-time resistance variation

```
float Vin = 5;
float Ref; // MANUALLY DEFINE A VALUE PROPORTIONAL TO SENSOR'S

float Vout;
float R; // Measured resistance Value from PEDOT:PSS device

void setup() {
  Serial.begin(9600);
  delay(1000);
 }

 void loop() {
   Vout = Vin * ( analogRead(0) / 1023.0 );
   R = Ref * ( ( Vin / Vout ) - 1 );
   Serial.println(R);
   delay(5000);
 }
```

6.3 Arduino scrip to measure real-time Vtherm generation

```
float AREF = 0.60;
float Vamp;
float Vtherm;

void setup(){
  Serial.begin(9600);
  analogReference(EXTERNAL);
}

 void loop(){
   Vamp  = AREF * ( analogRead(1) / 1023.0 ) ;
   Vtherm = ( Vamp / 50 )*1000 ; // mV
   Serial.println(Vtherm);
   delay(100);
 }
```

6.4 Processing script for the 4x4 pressure sensor matrix

Note: It is necessary to upload the *StantardFirmata* script on Arduino.

```
import processing.serial.*;
import cc.arduino.*;

Arduino Arduino; //creates Arduino object

int read;
int rectSize = 0;
int rectY;

float Vin = 5.0;
float Ref = 2000.0;

int[] data = new int[16];
float[] Vout = new float[16];

float[] Ro = new float[16];
float[] Rmin = new float[16];

float[] R = new float[16];

float[] dR = new float[16];
float[] RV = new float[16];

int i;
int j;

void setup() {

  arduino = new Arduino(this, Arduino.list()[1], 57600); //sets up arduino
  arduino.pinMode(0, Arduino.INPUT);//setup pins to be input (A0 =0?)

  size(800, 800, P3D); // set up the window to whatever size you want
  rectSize = width/4;
  background(255); // set initial background
  stroke(127, 0, 0);
  smooth(); // turn on antialiasing
  rectMode(CORNER);

  delay(5000);

for (int j = 0; j < 16; j++)
  {
    data[j] = arduino.analogRead(j);
    Vout[j] = Vin * ( data[j] / 1023.0 );
    Rmin[j] = Ref * ( (Vin/Vout[j]) - 1 );
    print(Rmin[j]);
    print(" ");
  }

  println(" ");
  delay(5000);


for (int j = 0; j < 16; j++)
```

```
  {
    data[j] = arduino.analogRead(j);
    Vout[j] = Vin * ( data[j] / 1023.0 );
    Ro[j] = Ref * ( (Vin/Vout[j]) - 1 );
    print(Ro[j]);
    print(" ");

  }

}

void draw() {

  for (int i = 0; i < 16; i++)
  {
    data[i] = arduino.analogRead(i);
    Vout[i] = Vin * (arduino.analogRead(i) / 1023.0 );
    R[i] = Ref * ( (Vin/Vout[i]) - 1 );
    dR[i] = ( R[i] - Ro[i]) / Ro[i] ;

    RV[i] = 1-((R[i]-Rmin[i])/(Ro[i]-Rmin[i])) ;

    fill(abs(RV[i]*255));
    rect(rectSize * (i%4), rectY, rectSize, rectSize); //top left

    textSize(32);
    textAlign(LEFT);
    fill(0, 102, 153);
    text(abs(int(dR[i]*100)), 40+rectSize*(i%4), 100+rectY);

    if ((i+1) % 4 == 0) rectY += rectSize;

  }
  rectY=0;
}
```

6.5 Videos from the 4x4 Matrix Device under testing

Test 1: https://youtu.be/ancM7RtknwM

Test 2: https://youtu.be/jHyVHZ7oWZs

6.6 Project for a position 8x8 sensor matrix device

Figure 6.1: A schematic from the setup system used to perform positioning tests on an 8x8 pressure sensor matrix using a single PEDOT:PSS@MS and Arduino microcontroller. The *Analog Ports* connect to the columns of the matrix and the *Digital Ports* to the rows.

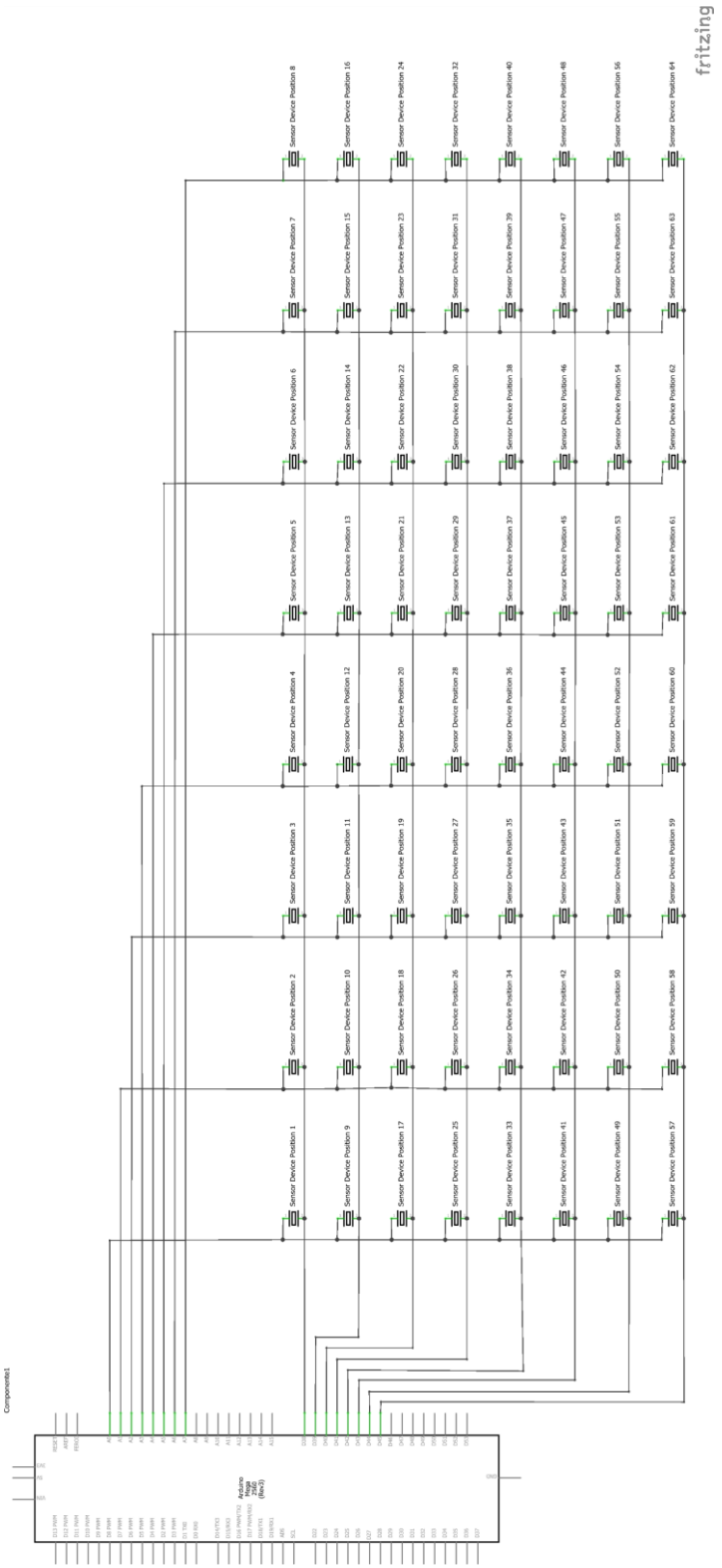

6.7 Processing script for an 8x8 pressure sensor matrix

Note: It is necessary to upload the *StantardFirmata* script on Arduino. The program sets the Arduino's pull-up resistors as a reference.

```
/*
Code based on Tom Igoe's Serial Graphing Sketch
 >> http://wiki.processing.org/w/Tom_Igoe_Interview
 Reads X analog inputs and visualizes them by drawing a grid
 using grayscale shading of each square to represent sensor value.
 >>
 */
import processing.serial.*;

Serial myPort; // The serial port
int maxNumberOfSensors = 64;
float[] sensorValue = new float[maxNumberOfSensors]; // global variable
for storing mapped sensor values
float[] previousValue = new float[maxNumberOfSensors]; // array of
previous values

float Vin = 5;
float Ref = 150;

float[] Vout = new float[maxNumberOfSensors];
float[] Ro = new float[maxNumberOfSensors];
float[] Rmin = new float[maxNumberOfSensors];

float[] R = new float[maxNumberOfSensors];

float[] dR = new float [maxNumberOfSensors];
float[] RV = new float[maxNumberOfSensors];

int rectSize = 0;
int rectY;
void setup () {

  size(900, 900); // set up the window to whatever size you want
  rectSize = width/8;

  //println(Serial.list()); // List all the available serial ports
  //String portName = Serial.list()[2];
  myPort = new Serial(this, "COM4", 57600);
  myPort.clear();
  myPort.bufferUntil(&apos;\n&apos;); // do not generate a serialEvent()
until you get a newline (\n) byte
  background(255); // set inital background
  stroke(127, 0, 0);
  smooth(); // turn on antialiasing
  rectMode(CORNER);
  delay(10000);
for (int j = 0; j < maxNumberOfSensors; j++)
  {
    Vout[j] = Vin*sensorValue[j]/254.0;
    Rmin[j] = Ref * ( (Vin/Vout[j]) - 1 );
    print(Rmin[j]);
    print(" ");
  }

  println(" ");
```

```
  delay(10000);

  for (int j = 0; j < 16; j++)
  {
    Vout[j] = Vin * ( sensorValue[j] / 254.0 );
    Ro[j] = Ref * ( (Vin/Vout[j]) - 1 );
    print(Ro[j]);
    print(" ");
  }
}

  void draw () {
    for (int i = 0; i < maxNumberOfSensors; i++)
    {

      Vout[i] = Vin*sensorValue[i]/254.0;
      R[i] = Ref * ( (Vin/Vout[i]) - 1 );
      dR[i] = ( R[i] - Ro[i]) / Ro[i] ;

      RV[i] = 1-((R[i]-Rmin[i])/(Ro[i]-Rmin[i])) ;

      fill(254*RV[i]);
      rect(rectSize * (i%8), rectY, rectSize, rectSize); //top left

      textSize(20);
      //textAlign(LEFT);
      fill(0, 102, 153);

      text(int(100*dR[i]), 10+rectSize*(i%8), 100+rectY);
      //text(R[i]/1000, 10+rectSize*(i%8), 80+rectY);


      if ((i+1) % 8 == 0) rectY += rectSize;
      //println(rectY);
    }
    rectY=0;
  }

  void serialEvent (Serial myPort)
  {
    String inString = myPort.readStringUntil(&apos;\n&apos;); // get the
ASCII string
    if (inString != null) { // if it&apos;s not empty
      inString = trim(inString); // trim off any whitespace
      int incomingValues[] = int(split(inString, "\t")); // convert to an
array of ints
      if (incomingValues.length <= maxNumberOfSensors &&
incomingValues.length > 0) {
        for (int i = 0; i < incomingValues.length; i++) {
          // map the incoming values (0 to 1023) to an appropriate gray-
scale range (0-255):
          sensorValue[i] = map(incomingValues[i], 0, 1023, 0, 255);
//println(sensorValue[i]);
        }
      }
    }
  }
```

6.8 Prototype PEDOT:PSS(diluted)@MS-based 8x8 sensory array

Figure 6.2 shows a prototype for an 8x8 matrix device, based on PEDOT:PSS(diluted)@MS. The top flexible electrode has eight copper paths (the columns), while the rigid bottom electrode has the other eight paths (the rows). The electrodes are attached to the foam so that the paths are perpendicular to each other, as a grid. Each of the 64 intersection points on the grid is a pixel on the sensory matrix device. The paths are 3 mm wide, and the foam is a single piece of 4.5x4.5 cm^2 and 2 mm thick.

Figure 6.2: An 8x8 matrix device prototype based on PEDOT:PSS(diluted)@MS.

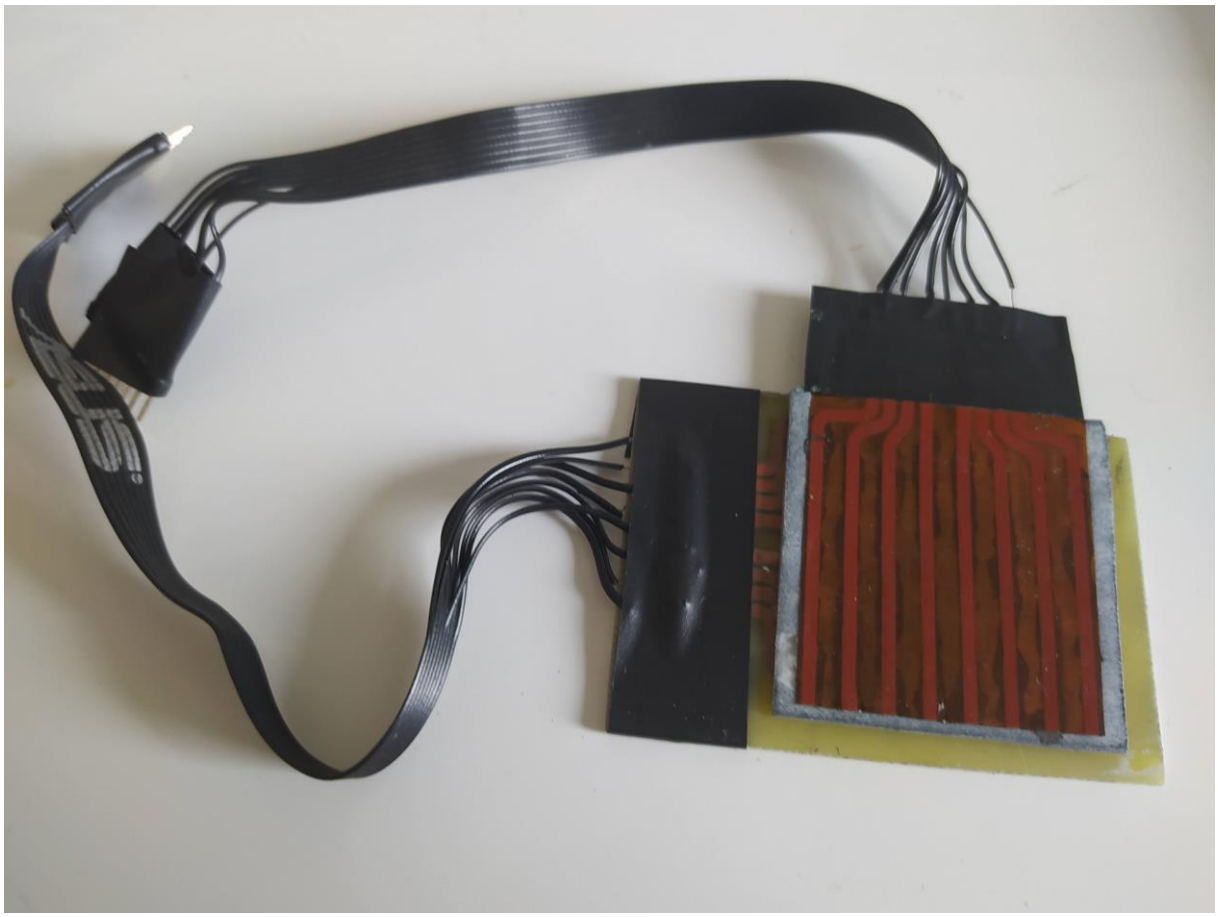

7. REFERENCES

ARDUINO.CC. **Pinout-Mega2560rev3_latest**. *[s. l.]*, 2020. Available at: https://content.arduino.cc/assets/Pinout-Mega2560rev3_latest.pdf. Accessed on: 1 set. 2020.

Color \ Processing.org. . *[s. l.]*, *[s. d.]*. Avaliable at: https://processing.org/tutorials/color/. Accessed on: 17 set. 2020.

CRISPIN, X. *et al.* The origin of the high conductivity of poly(3,4-ethylenedioxythiophene)-poly(styrenesulfonate) (PEDOT-PSS) plastic electrodes. **Chemistry of Materials**, *[S. l.]*, 2006. Available at https://doi.org/10.1021/cm061032+

DING, Y. *et al.* Flexible and Compressible PEDOT:PSS@Melamine Conductive Sponge Prepared via One-Step Dip Coating as Piezoresistive Pressure Sensor for Human Motion Detection. **ACS Applied Materials and Interfaces**, *[S. l.]*, v. 10, n. 18, p. 16077–16086, 2018. Available at: https://doi.org/10.1021/acsami.8b00457. Accessed on: 9 Jan. 2019.

DÖBBELIN, M. *et al.* Influence of ionic liquids on the electrical conductivity and morphology of PEDOT:PSS films. **Chemistry of Materials**, *[S. l.]*, 2007. Available at: https://doi.org/10.1021/cm070398z

File:Ellipsometry_setup @ commons.wikimedia.org. . *[S. l.: s. n.]* Avaliable at: https://commons.wikimedia.org/wiki/File:Ellipsometry_setup.svg

File:Polythiophenes_Pedotpss @ commons.wikimedia.org. . *[S. l.: s. n.]* Avaliable at: https://commons.wikimedia.org/wiki/File:Polythiophenes_Pedotpss.png

FUJIWARA, H. **Spectroscopic Ellipsometry: Principles and Applications**. *[S. l.: s. n.]*. *E-book*. Available at: https://doi.org/10.1002/9780470060193

GIBSON, L. J.; ASHBY, M. F. **Cellular solids: Structure and properties, second edition**. *[S. l.: s. n.]*. *E-book*. Available at: https://doi.org/10.1017/CBO9781139878326

GRAZ, I. *et al.* Flexible active-matrix cells with selectively poled bifunctional polymer-ceramic nanocomposite for pressure and temperature sensing skin. *[S. l.]*, 2009. Available at: https://doi.org/10.1063/1.3191677

GROENENDAAL, L. *et al.* Poly(3,4-ethylenedioxythiophene) and its derivatives: past, present, and future. **Advanced Materials**, *[S. l.]*, 2000. Available at: https://doi.org/10.1002/(SICI)1521-4095(200004)12:7<481::AID-ADMA481>3.0.CO;2-C

GUIRIEC, S. *et al.* Organic Nonvolatile Memory Transistors for Flexible Sensor Arrays. *[S. l.]*, 2009. Available at: https://doi.org/10.1126/science.1182174. Accessed on: 17 Jan. 2019.

HOFMANN, A. I.; KROON, R.; MÜLLER, C. Doping and processing of organic semiconductors for plastic thermoelectrics. *In*: **Handbook of Organic Materials for Electronic and Photonic Devices**. *[S. l.: s. n.]*. *E-book*. Available at: https://doi.org/10.1016/b978-0-08-102284-9.00013-9

Introduction @ Www.Arduino.Cc. . *[S. l.: s. n.]* Avaliable at: https://www.arduino.cc/en/guide/introduction

LAI, S. *et al.* Ultralow Voltage Pressure Sensors Based on Organic FETs and Compressible Capacitors. **IEEE ELECTRON DEVICE LETTERS**, *[S. l.]*, v. 34, n. 6, 2013. Available at: https://doi.org/10.1109/LED.2013.2257660

MASSONNET, N. *et al.* Improvement of the Seebeck coefficient of PEDOT:PSS by chemical reduction combined with a novel method for its transfer using free-standing thin films †. *[S. l.]*, 2014. Available at: https://doi.org/10.1039/c3tc31674b. Accessed on: 21 nov. 2019.

MENGISTIE, D. A. *et al.* Enhanced thermoelectric performance of PEDOT:PSS flexible bulky papers by treatment with secondary dopants. **ACS Applied Materials and Interfaces**, *[S. l.]*, v. 7, n. 1, p. 94–100, 2015.

Available at: https://doi.org/10.1021/am507032e

NEACȘU, I. A. *et al.* Inorganic micro-and nanostructured implants for tissue engineering. *In*: **Nanobiomaterials in Hard Tissue Engineering: Applications of Nanobiomaterials**. *[S. l.: s. n.]*. *E-book*. Available at: https://doi.org/10.1016/B978-0-323-42862-0.00009-2

OUYANG, J. *et al.* On the mechanism of conductivity enhancement in poly(3,4-ethylenedioxythiophene):poly(styrene sulfonate) film through solvent treatment. **Polymer**, *[S. l.]*, 2004. Available at https://doi.org/10.1016/j.polymer.2004.10.001

PARK, Y. *et al.* Flexible, light trapping substrates for organic photovoltaics. **Applied Physics Letters**, *[S. l.]*, 2016. Available at: https://doi.org/10.1063/1.4962206

PLUSEA. **http://flic.kr/p/2hfdoV6**. *[s. l.]*, 2019. Available at: https://www.flickr.com/photos/plusea/48731250207/.

SAGHAEI, J.; FALLAHZADEH, A.; SAGHAEI, T. ITO-free organic solar cells using highly conductive phenol-treated PEDOT:PSS anodes. **Organic Electronics: physics, materials, applications**, *[S. l.]*, 2015. Available at: https://doi.org/10.1016/j.orgel.2015.06.002

SAGHAEI, J.; FALLAHZADEH, A.; YOUSEFI, M. H. Improvement of electrical conductivity of PEDOT:PSS films by 2-Methylimidazole post treatment. **Organic Electronics: physics, materials, applications**, *[S. l.]*, 2015. Available at: https://doi.org/10.1016/j.orgel.2015.01.026

SATOH, N. *et al.* Organic π-type thermoelectric module supported by photolithographic mold: a working hypothesis of sticky thermoelectric materials. **Science and Technology of Advanced Materials**, *[S. l.]*, 2018. Available at: https://doi.org/10.1080/14686996.2018.1487239

SCHWARTZ, G. *et al.* Flexible polymer transistors with high pressure sensitivity for application in electronic skin and health monitoring. **Nature Communications**, *[S. l.]*, v. 4, n. May, p. 1858–1859, 2013. Available at: https://doi.org/10.1038/ncomms2832. Accessed on: 17 Jan. 2019.

SEKITANI, T. *et al.* A rubberlike stretchable active matrix using elastic conductors. **Science**, *[S. l.]*, v. 321, n. 5895, p. 1468–1472, 2008. Available at: https://doi.org/10.1126/science.1160309

SEKITANI, T. *et al.* Flexible organic transistors, and circuits with extreme bending stability. **Nature Materials**, *[S. l.]*, v. 9, n. 12, p. 1015–1022, 2010. Available at: https://doi.org/10.1038/nmat2896. Accessed on: 17 Jan. 2019.

SMITS, F. M. Measurement of Sheet Resistivities with the Four-Point Probe. **Bell System Technical Journal**, *[S. l.]*, 1958. Available at: https://doi.org/10.1002/j.1538-7305.1958.tb03883.x

SOMEYA, T. *et al.* Conformable, flexible, large-area networks of pressure and thermal sensors with organic transistor active matrixes. **Proceedings of the National Academy of Sciences**, *[S. l.]*, v. 102, n. 35, p. 12321–12325, 2005. Available at: https://doi.org/10.1073/pnas.0502392102. Accessed on: 17 Jan. 2019.

SOPRA SA (France). . *[S. l.: s. n.]*. Available at www.sopra-sa.com. Accessed on: 27 ago. 2020.

STAPLETON, A. J. *et al.* Planar silver nanowire, carbon nanotube and PEDOT:PSS nanocomposite transparent electrodes. **Science and Technology of Advanced Materials**, *[S. l.]*, 2015. Available at: https://doi.org/10.1088/1468-6996/16/2/025002

SZE, S. M.; NG, K. K. Physics of Semiconductor Devices, 3rd Edition - Simon M. Sze, Kwok K. Ng. **Physics of Semiconductor Devices, 3rd Edition.; John Wiley & Sons, Inc.; NJ**, *[S. l.]*, 2007. Available at: https://doi.org/10.1002/9780470068328.fmatter

TEE, B. C. K. *et al.* An electrically and mechanically self-healing composite with pressure- and flexion-sensitive properties for electronic skin applications. **Nature Nanotechnology**, *[S. l.]*, v. 7, n. 12, p. 825–832, 2012. Available at: https://doi.org/10.1038/nnano.2012.192. Accessed on: 17 Jan. 2019.

The Seebeck Coefficient | Electronics Cooling. . *[s. l.]*, *[s. d.]*. Available at: https://www.electronics-

cooling.com/2006/11/the-seebeck-coefficient/. Accessed on: 21 nov. 2019.

UIO: DEPARTMENT OF PHYSICS. **Thermoelectrics @ www.mn.uio.no**. *[s. l.]*, 2012. Avaliable at: https://www.mn.uio.no/fysikk/english/research/projects/bate/thermoelectricity/.

VEDAM, K. Spectroscopic ellipsometry: A historical overview. **Thin Solid Films**, *[S. l.]*, 1998. Available at: https://doi.org/10.1016/S0040-6090(97)00762-1

VRIES, D. V. W. M. De. the Mechanics of Foam. *[S. l.]*, n. July, p. 3, 2009. Available at: http://www.mate.tue.nl/mate/pdfs/10702_sec.pdf

W. E. BEADLE, J. C. C. TSAI, and R. D. P. **QUICK REFERENCE MANUAL FOR SILICON INTEGRATED CIRCUIT TECHNOLOGY.** *[S. l.: s. n.]*. *E-book.*

WANG, S. *et al.* Skin electronics from scalable fabrication of an intrinsically stretchable transistor array. **Nature**, *[S. l.]*, v. 555, n. 7694, p. 83–88, 2018. Available at: https://doi.org/10.1038/nature25494

WANG, Z. *et al.* Flexible Dual-Mode Tactile Sensor Derived from Three-Dimensional Porous Carbon Architecture. **ACS Applied Materials and Interfaces**, *[S. l.]*, 2017. Available at: https://doi.org/10.1021/acsami.7b04812. Accessed on: 19 Mar. 2019.

ZHANG, F. *et al.* Flexible and self-powered temperature–pressure dual-parameter sensors using microstructure-frame-supported organic thermoelectric materials. *[S. l.]*, 2015. Available at: https://doi.org/10.1038/ncomms9356